sPH-PPG-2023-002
v1.0
January 29, 2025

$dN_{ch}/d\eta$ at sPHENIX in Run 24 Au+Au collisions with the INTT

Joseph Bertaux[1], Cameron Dean[2], Takashi Hachiya[3], Misaki Hata[3], Jaein Hwang[4], Hao-Ren Jheng[2], Tomoya Kato[5], Chia-Ming Kuo[6], Itaru Nakagawa[7], Genki Nukazuka[7], Michael Peters[2], Gunther Roland[2], Cheng-Wei Shih[6], Maya Shimomura[3], and Yuka Sugiyama[3]

[1] *Purdue University*
[2] *Massachusetts Institute of Technology*
[3] *Nara Women University*
[4] *Korea University*
[5] *Rikkyo University*
[6] *National Central University*
[7] *RIKEN/RBRC*

Abstract

Measurements of the pseudorapidity distributions of charged hadrons produced in gold-gold collisions at a center-of-mass energy $\sqrt{s_{NN}} = 200\,\text{GeV}$ are presented. The data used for analysis was collected by the sPHENIX detector using a minimum-bias trigger, with the trigger decision based on inputs from the Minimum-Bias Detector and Zero-Degree Calorimeter. The number of charged hadrons is measured by counting the pairs of clusters in the inner and outer layers of the Intermediate Silicon Tracker, corrected by detector acceptance and reconstruction efficiencies. The study includes comparisons of the results to previous measurements from different experiments at various energies and collision systems, along with comparisons to theoretical models.

Contents

Log

(v1) First frozen version for the convener review – January 28, 2025

1. The sPHENIX software analysis build is to be updated when the official productions of both data and simulation are finalized (Table 2)

2. ~~Section 2.1.3 (INTT calibration – Hot, dead, and cold channel masks). Plots in Appendix A are to be updated with run 54280~~ Plots in Appendix A are updated on January 29, 2025

3. Section 3 (Monte Carlo). Keep the section for unconventional configurations and settings for this analysis, even though the decision was to have the simulation produced centrally

4. Section 7 (Systematic uncertainties): 2 additional systematic uncertainties (event generator and strangeness decays) to be included when the official production and the centrality for the simulation are ready

5. Section 8 and 9 (Results and Conclusion): Table 6, Figure 71 and 70 are to be updated when the official production and the centrality for the simulation are ready (Similarly the plots in Appendix G Figure 102 and 103)

---

1 Introduction

A hot medium of strongly interacting, deconfined quarks and gluons, known as the quark-gluon plasma (QGP), is formed in ultra-relativistic heavy-ion collisions [1]. The multiplicity and pseudorapidity (η) distributions of charged particles produced in these collisions are critical observables for characterizing the initial conditions and the subsequent hydrodynamic evolution of the QGP [2]. Furthermore, the dependence of charged-particle multiplicity on the colliding system, center-of-mass energy, and collision geometry provides insight into nuclear shadowing, gluon saturation effects [3], and the contributions and modeling of particle production from hard scattering and soft processes [4, 5]. Studying the charged-hadron multiplicity and its dependence on η is essential for understanding the formation and properties of the QGP in heavy-ion collisions.

At Relativistic Heavy-Ion Collider (RHIC), measurements of the system-size dependence of charged-particle η density, denoted as $\mathrm{dN_{ch}/d}\eta$, have been performed for copper-copper (Cu+Cu) and gold-gold (Au+Au) collisions at various center-of-mass energies. Similarly, the ALICE, ATLAS, and CMS experiments at Large Hadron Collider (LHC) have reported $\mathrm{dN_{ch}/d}\eta$ at mid-rapidity ($|\eta|< 0.5$), expressed as $\langle \mathrm{dN_{ch}/d}\eta \rangle$, for lead-lead (Pb+Pb) and xenon-xenon (Xe+Xe) collisions at TeV energy scales. These measurements, summarized in Table 1, have revealed several key empirical trends: (1) Charged-particle production approximately follows a power-law scaling with center-of-mass energy. (2) Central heavy-ion collisions show a steeper increase in $\langle \mathrm{dN_{ch}/d}\eta \rangle$ as a function of center-of-mass energy compared to proton-proton (p+p) and proton-nucleus (p+A) collisions. (3) The values of $\langle \mathrm{dN_{ch}/d}\eta \rangle$, normalized by the number of participating nucleon pairs (N_{part}), grow faster than linearly with N_{part}. (4) The shapes of the N_{part} dependence remain consistent across different collision energies. These findings provide an opportunity to test scaling laws and models tuned to data from different energy regimes and evaluate their applicability to other systems.

This note describes the measurement of $\mathrm{dN_{ch}/d}\eta$ using data collected by the sPHENIX detector, employing a minimum-bias trigger based on inputs from the Minimum-Bias (Min. Bias) Detector (MBD) and the Zero-Degree Calorimeter (ZDC). The analysis depends on the synchronization and functionality of key detector components and the reconstruction chain, including triggering, synchronization across subdetectors, proper operation and coordination of readout servers within individual subdetectors, centrality determination, data readout, bad channel mapping, hit decoding and unpacking, clustering, vertex finding, and detector alignment. Consequently, this work is closely tied to the commissioning of the detector.

Two analysis approaches have been developed. The first is based on methods from the PHOBOS and PHENIX publications [9, 32], while the second follows the CMS Run 2 Xe+Xe and Run 3 Pb+Pb analyses [29, 28]. Both approaches share common global objects, including tracking and calorimeter data storage tapes (DSTs), simulations, INTT calibrations, clusters, scaled trigger objects, Min. Bias classification, centrality calibration, and truth-level definitions. However, the approaches differ in their methods for vertex reconstruction (Section 5.4), tracklet reconstruction and counting (Section 5.5), correction factors (Section 6), and systematic uncertainties (Section 7). The shared objects will be discussed jointly, while analysis methods are introduced and explained separately.

Experiment	Collision species	Center-of-mass energy	Number of analyzed events	Reference
PHENIX	Au+Au	130 GeV	$\sim$ 137 k	[6]
		19.6 GeV 130 GeV 200 GeV	40 k 160 k 270 k	[7]
PHOBOS	Au+Au	56 GeV 130 GeV	382 724	[8]
	Au+Au Cu+Cu d+Au p+p	19.6–200 GeV 22.4–200 GeV 200 GeV 200 and 410 GeV	–	[9]
ALICE	p+p	900 GeV	284	[10]
		900 GeV 2.36 TeV	150 k 40 k	[11]
		7 TeV	300 k	[12]
		13 TeV	$\sim$ 1.5 M	[13]
		0.9, 2.36, 2.78, 7, and 8 TeV	40 k-343.7 M	[14]
		0.9, 7, and 8 TeV	7.4 k-61 M	[15]
		5.02, 7, and 13 TeV	–	[16]
	Pb+Pb	2.76 TeV	2711	[17]
		5.02 TeV	$\sim$ 100 k	[18]
	Xe+Xe	5.44 TeV	$\sim$ 1 M	[19]
CMS	p+p	0.9 and 10 TeV	$\sim$ 5 k	[20]
		0.9 TeV 2.36 TeV	$\sim$ 40.3 k $\sim$ 10.8 k	[21]
		7 TeV	$\sim$ 55 k	[22]
		0.9, 2.36, and 7 TeV	12-442 k	[23]
		8 TeV	–	(With TOTEM) [24]
		13 TeV	11.5 M	[25]
	p+Pb	5.02 TeV 8.16 TeV	$\sim$ 420 k $\sim$ 3 M	[26]
	Pb+Pb	2.76 TeV	$\sim$ 100 k	[27]
		5.36 TeV	–	[28]
	Xe+Xe	5.44 TeV	$\sim$ 1.36 M	[29]
ATLAS	p+Pb	5.02 TeV	$\sim$ 2.1 M	[30]
	Pb+Pb	2.76 TeV	$\sim$ 1.63 M	[31]

Table 1: Selected measurements from previous and present experiments. Information not explicitly mentioned in the publication is marked as ”–”.

2 Event selection

2.1 Data

The analysis uses Min. Bias Au+Au collision data collected on October 10, 2024, acquired without the sPHENIX magnetic field [33]. Table 2 summarizes the key properties of the analyzed data sample.

Property	Value
Run	54280
Production tag	ProdA_2024
Centrality calibration tag	ProdA_2024
Software build	ProdA_2024

Table 2: Key properties of the analyzed data DST.

NOTE: The software analysis build will be finalized when the productions for both data and simulation and the centrality for simulation are ready for the analysis.

2.1.1 Min. Bias definition

The Min. Bias criteria are defined in Ref. [34]:

1. The Level-1 trigger condition: at least 2 hits above threshold in both the north and south MBD
2. Background cleaning: Events, where the charge signal in the south MBD exceeds that of the north MBD by more than 10 times, are discarded
3. Coincidence of energy deposit greater than 40 GeV between the north and south ZDC. This significantly removes non-collision background at high luminosities
4. A vertex cut of $|z_{\text{MBD}}| < 60\,\text{cm}$

2.1.2 INTT calibration – Hit BCO mask

A firmware upgrade to FELIX enabled timing synchronization across the FELIX servers. This synchronization was validated by the fact that the spikes in the BCO difference between collected hits and the GTM clock for all FELIX servers align at the same position, as shown in Figure 1. However, for run 54280, the strobe length was set to 100 BCOs, allowing the possibility of multiple collisions occurring within a single strobe length (also referred to as a Fun4All event). To address this, a hit BCO filter is applied to include only hits recorded within ± 1 BCO relative to the trigger BCO. This 3-BCO acceptance window accounts for potential incorrect hit BCO assignments within one strobe length due to imperfect coarse delay settings in FELIX, as illustrated in Figure 2.

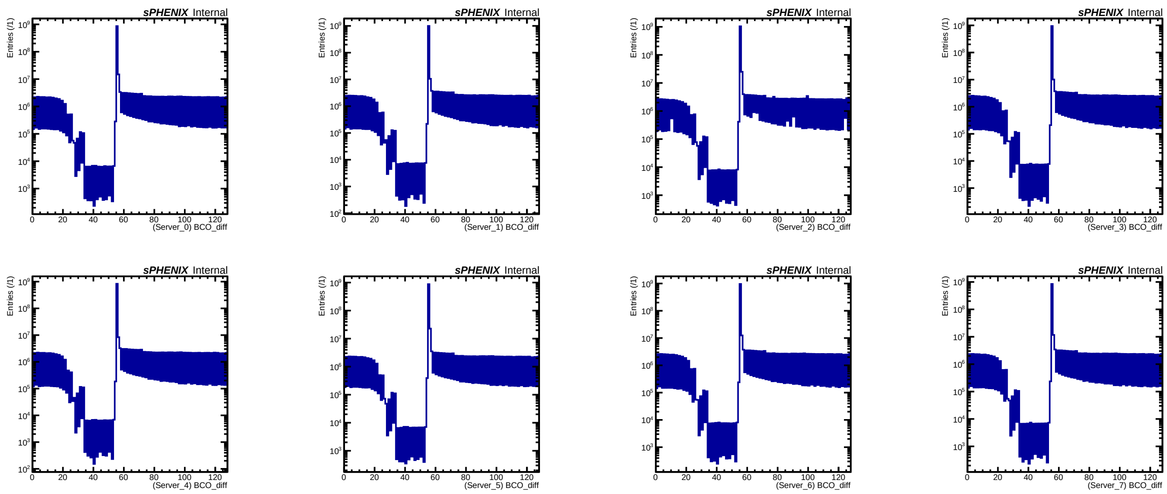

Figure 1: The BCO difference between hits and the GTM clock for each FELIX server.

In general, the readout chain of the INTT is the same as that of PHENIX Forward Silicon Vertex Detector (FVTX) [35]. The timing distribution of the hits are expected to be within one BCO, 106 ns, as shown in Figure 2. The coarse delay controls the shift of the hit timing relative to the beam clock. An imperfect coarse delay setting can lead to hits falling outside the corresponding expected timing window, resulting in incorrect hit timing assignments. To account for this, the hit timing is not considered in the clustering step.

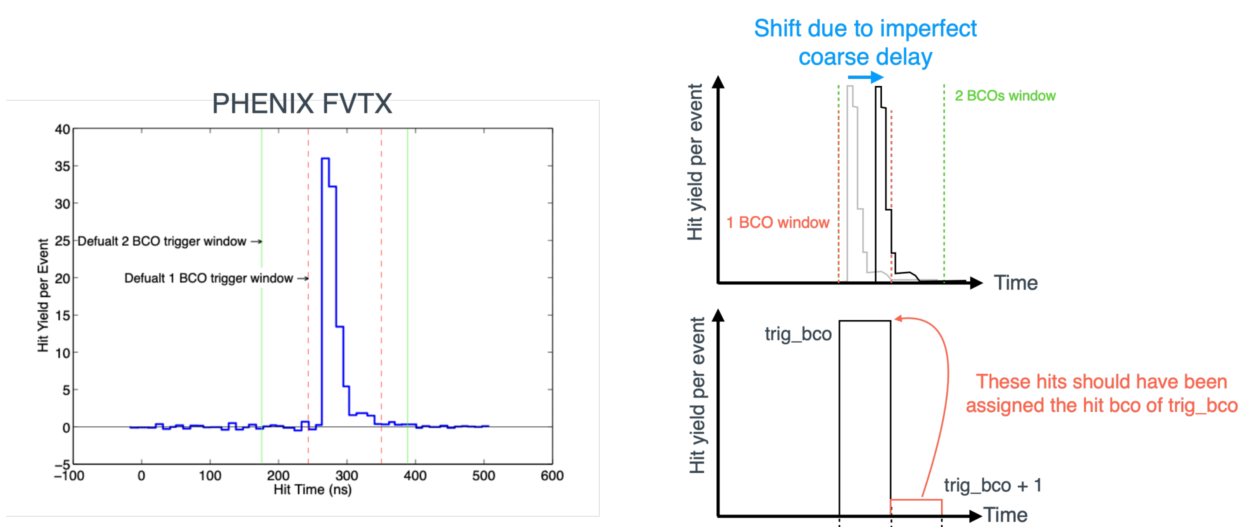

Figure 2: (Left) The timing distribution of the FVTX hits relative to the RHIC beam clock. (Right) Demonstrating the consequence of having imperfect coarse implementation in the FELIX firmware.

2.1.3 INTT calibration – Hot, dead, and cold channel masks

NOTE: Channel masks in Appendix A will be updated shortly.

Hot, dead, and cold channels were identified using a data-driven method based on the first 50,000 events and masked during the hit unpacking process. For each channel in an INTT half-ladder, the hit rate, corrected for strip length and the radius of its position, is filled into a histogram, an example of which is shown in Figure 3. A Gaussian function is fitted to the distribution. Channels with hit rates exceeding the mean of the fitted Gaussian by 5σ are classified as hot channels, while those falling 3σ below the mean are classified as cold channels. Channels with hit rates of zero are identified as dead channels. Table 3 summarizes the classification results, and the hit distributions with bad channels masked are shown in Figure 4.

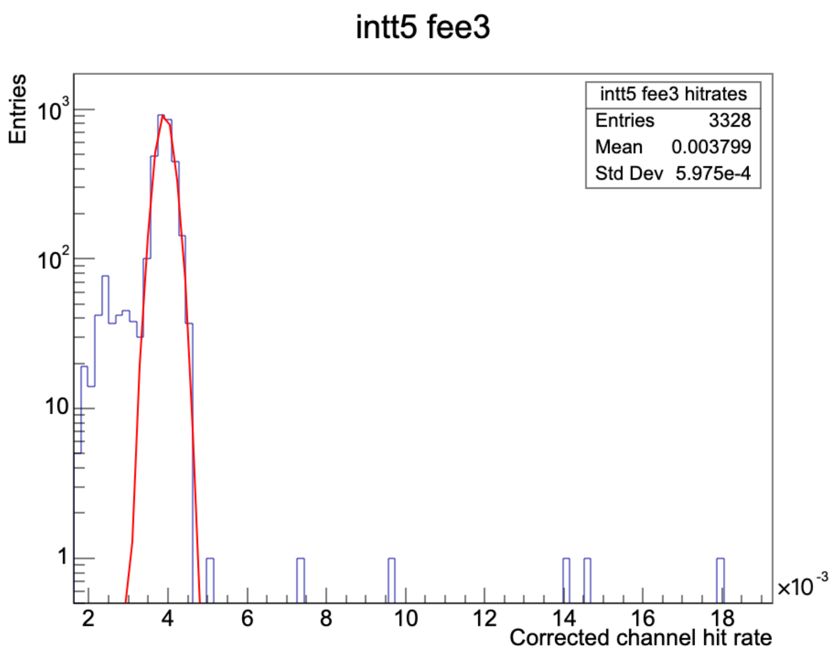

Figure 3: The corrected channel hit rate distribution of FELIX server 5 and FELIX channel 3.

Channel type	Number of channels	Ratio
Hot	36	0.01%
Dead	5547	1.49%
Cold	9119	2.45%
Good	358,034	96.06%

Table 3: The summary of channel classification of run 54280.

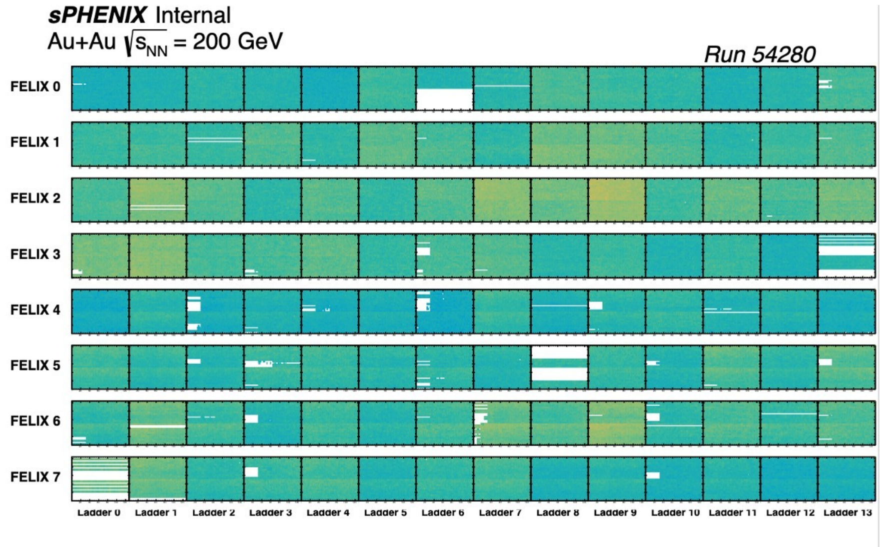

Figure 4: INTT hit map of run 54280 after applying the bad channel mask.

2.1.4 INTT calibration – Analog-to-digital conversion

The FPHX readout chip [36] used by INTT features a 3-bit analog-to-digital (ADC) converter with eight programmable signal amplitude comparators. 1 lists the threshold settings for each comparator during the zero-field data acquisition. The INTT rawhit data provide a 3-bit signal amplitude, which is mapped to its corresponding ADC threshold in the rawhit decoding process. These hit ADC values are then used in the clustering stage to determine the cluster position.

$$\text{Threshold setting} = [35, 45, 60, 90, 120, 150, 180, 210]. \tag{1}$$

2.1.5 Event BCO removal

Events with a BCO difference of less than 62 relative to their preceding event were discarded to mitigate the issue of incorrect hit association. This issue was initially identified as off-diagonal entries in the correlation between the number of inner and outer INTT clusters and the MBD charge sum, as shown in Figure 5. These off-diagonal events were not caused by the hit BCO or bad channel masks, as they persisted even when these masks were disabled. Additionally, their presence in Min. Bias events suggests that they are unlikely to originate from beam backgrounds.

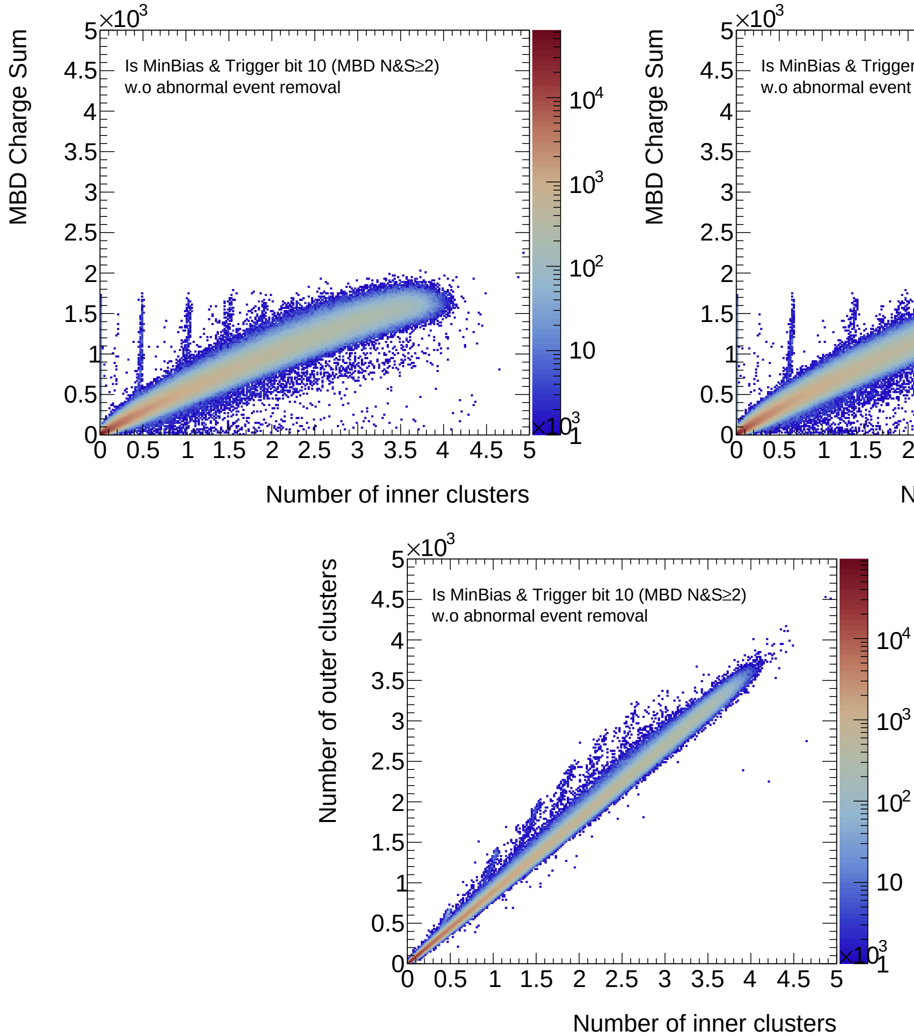

Figure 5: The correlation between the number of inner and outer INTT clusters and the MBD charge sum.

Figure 6 shows the difference in event BCO between an off-diagonal event and its next adjacent event, demonstrating that, in most cases, the adjacent event occurs within 60 BCOs[1] of the event of interest. This highlights an issue in INTT data acquisition, as illustrated in Figure 7 and detailed below.

The FPHX chip, used as the INTT readout chip, was originally designed for the PHENIX FVTX detector [37]. A key requirement of the FPHX architecture is its ability to read out an event containing four hits within four beam crossover periods. For example, when a trigger is fired and a single chip with 60 channels is assumed to be activated, it would take approximately 60 BCOs to read out all 60 hits and send them to the INTT Read-Out Card (ROC). However, during Run2024, the sPHENIX DAQ system had a hard-coded busy window of 15 BCOs. This means that a subsequent trigger signal could arrive at the subsystems only 15 BCOs after the previous trigger, as shown in Figure 8. As a result, the INTT event header, which is based on the GTM clock, could be overwritten by the new triggered GTM clock. This causes hits to be associated with the wrong GTM clock, effectively carrying them over to the next triggered event.

Figure 9 further supports this understanding. In the top two plots, two spikes are observed in the next event (BCO 1029942106894, event ID 2453, right plot) following the event of interest (BCO 1029942106868, event ID 2452, left plot). One spike, at a time bucket of 55, corresponds to the hits from the triggered BCO and is also presented in the event of interest. The second spike, at a time bucket of 29, differs from 55 by the same BCO difference between the two events, indicating that these hits are carried over from the previous event. The bottom plots compare the time buckets of hits from the event of interest (blue), the adjacent event (red), and the hits from the adjacent event recalculated relative to the event of interest (green). The overlap between the green and blue distributions shows that some hits from the next adjacent event share the same time bucket as the event of interest, providing clear evidence of incorrect hit assignment.

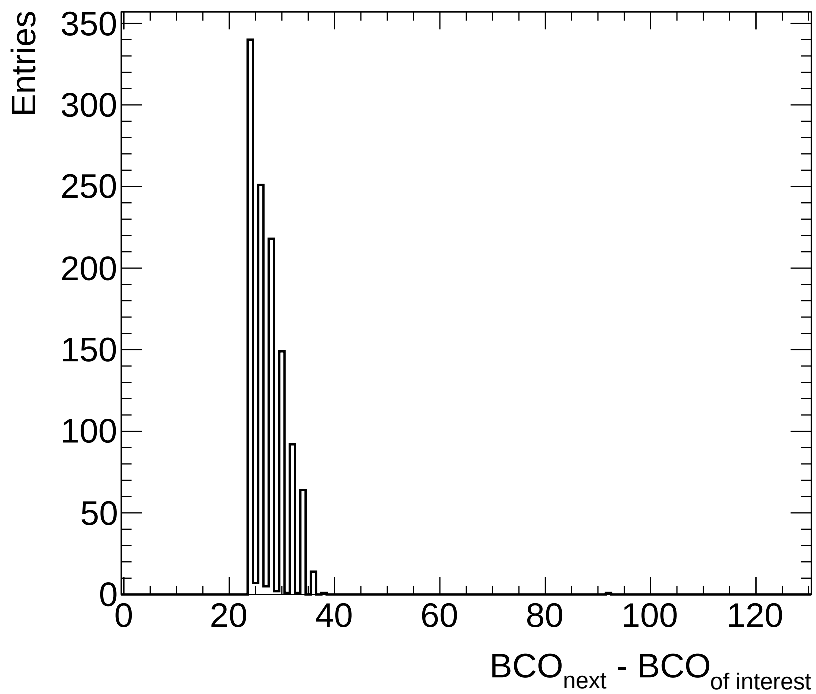

Figure 6: The difference in event BCO between the off-diagonal event (labeled as $\mathrm{BCO}_{\text{of interest}}$) and its next adjacent event (labeled as $\mathrm{BCO}_{\text{next}}$).

[1]In run 54280, the INTT "open_time" for the FELIX to read out hits is 60 BCOs.

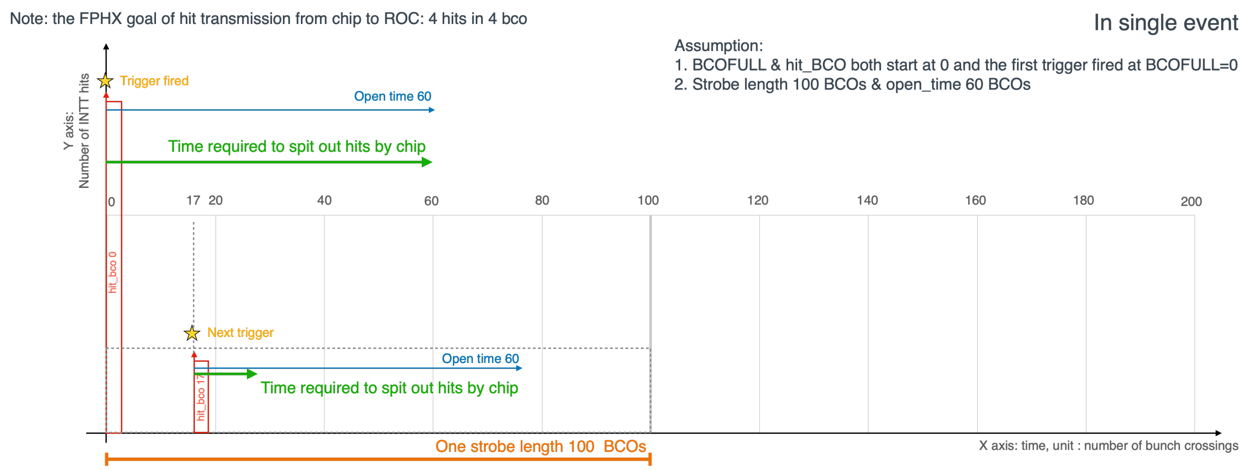

Figure 7: The data process logic of INTT in a single event.

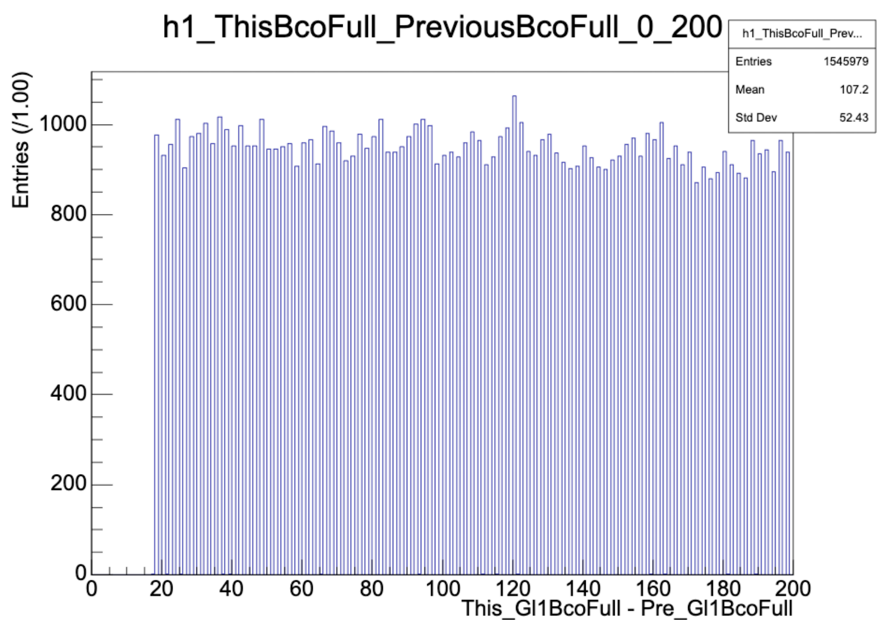

Figure 8: The event BCO spacing of run 54280. The BCO range of 0 to 200 is shown.

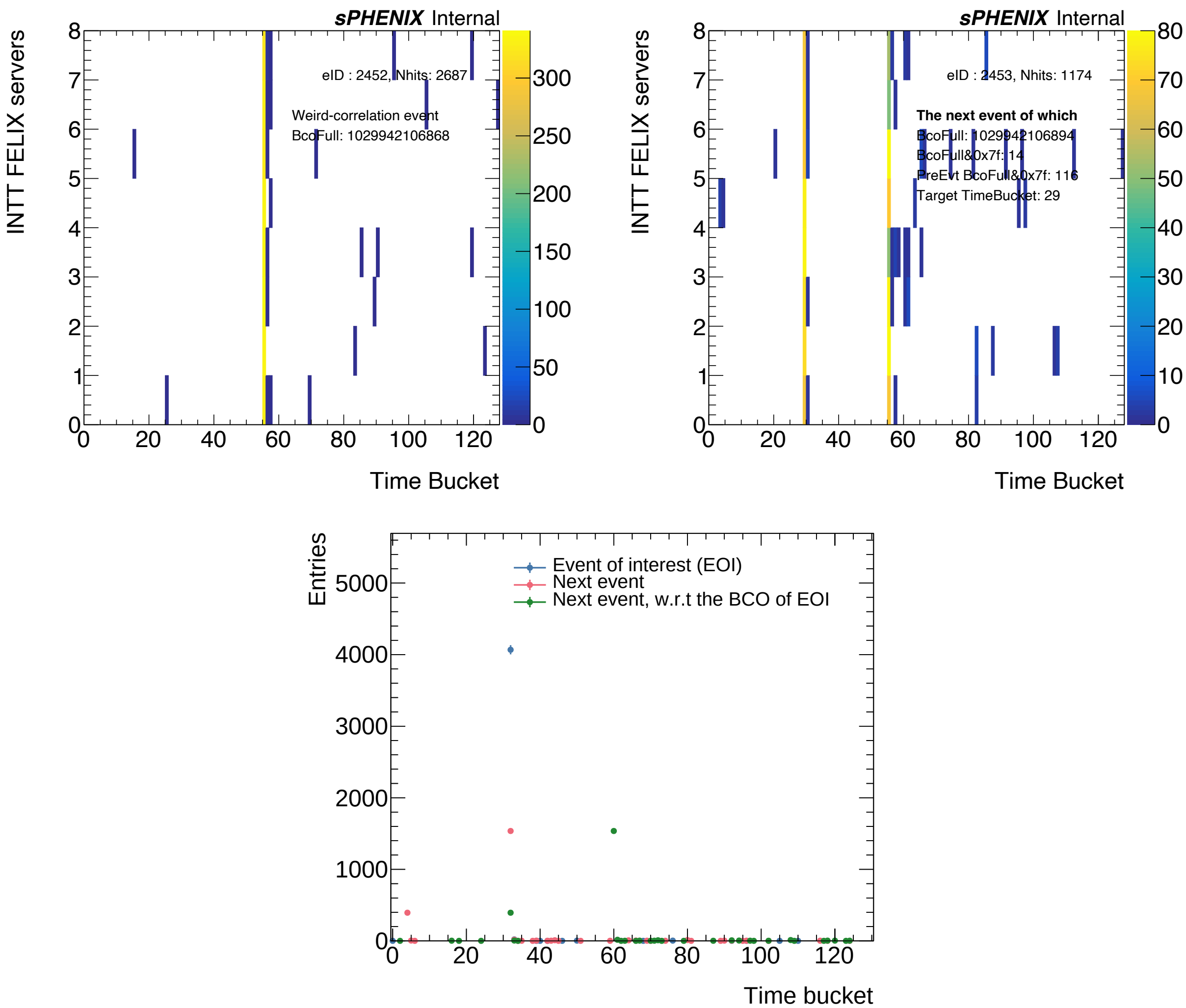

Figure 9: An example of the hit time bucket distributions for all eight INTT FELIX servers in the event of interest (top left) and its next event (top right). (Bottom) The time buckets of hits from the event of interest (blue), the adjacent event (red), and the time bucket of hits from the adjacent event recalculated relative to the event of interest (green).

Figure 10 shows the same correlations as Figure 5, but with the event BCO removal applied. After this removal process, approximately 1.4% of events were discarded, irrespective of the centrality intervals, as shown in Figure 11.

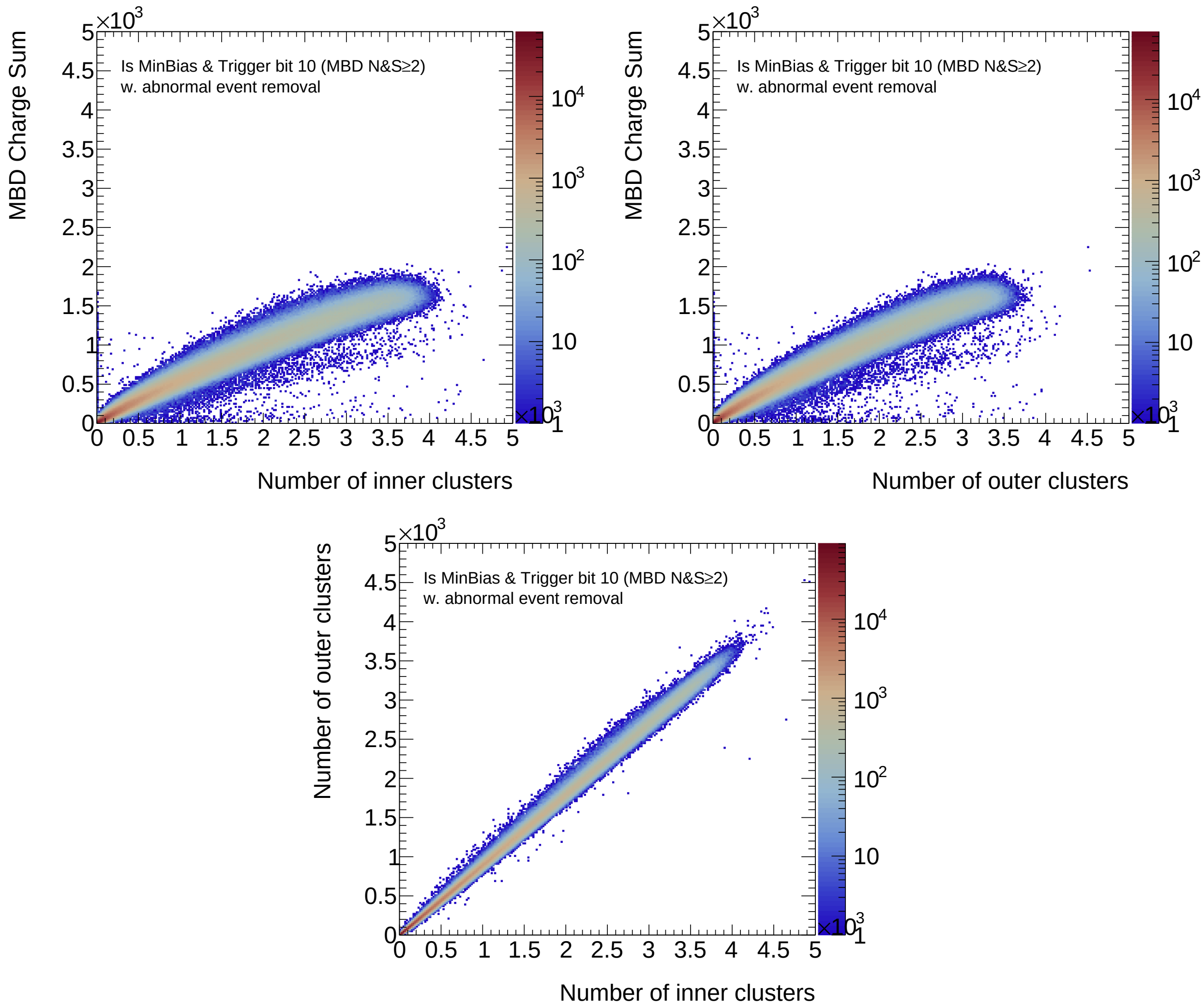

Figure 10: The correlation between the number of inner and outer INTT clusters and the MBD charge sum after the event BCO removal.

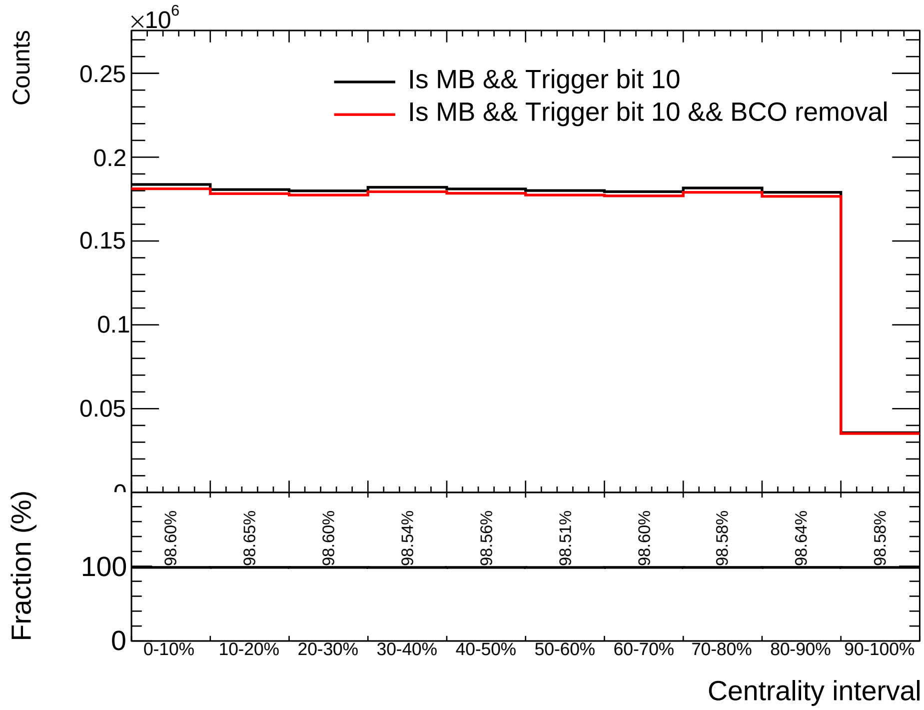

Figure 11: Fraction of events discarded by the event BCO removal as a function of centrality.

2.2 Offline selection

In addition to the Min. Bias definition, additional selections on global physics objects are applied offline for the analysis:

- Scale trigger bit 10: MBD charges in both north and south sides ≥ 2
- $-10\,\mathrm{cm} \leq$ Reconstructed vertex Z position ($\mathrm{vtx_Z}$) $\leq 10\,\mathrm{cm}$, discussed in Section 5.4.3
- Centrality interval $0 - 70\%$

3 Monte Carlo

All simulations were produced using the Fun4All framework. However, as the analysis uses non-standard detector configurations (such as a shifted Z-vertex and no magnetic field), and only requires the beam pipe, MVTX, INTT, and MBD to be simulated for a small number of events, it was decided to design our own simulation setup rather than request a centralised production.

The framework of mass simulation production via framework and all user requests are handled via a top-level python script which creates a condor submission file and any required folders. The framework has options to run single particle events of any particle type, Pythia8, or read HepMC files. There are three different generators that have produced HepMC files; HIJING, EPOS, and AMPT. All three generators are used in the analysis to verify the accuracy of the Monte Carlo samples.

To ensure the simulations are reproducible, all productions are generated using an `ana` build. An `ana` build is a permanently archived copy of the sPHENIX software stack that is created every Saturday at approximately 3 am. Using an `ana` build also ensures that simulations are performed with all calibrations, major reconstruction updates, detector geometries, and bug fixes synchronized with the simulation DSTs centrally produced by the sPHENIX software and production team.

Three methods are also used to track the production settings for each DST. The first method uses the folder structure of the file, which is the most user-friendly but the most susceptible to losing information as all a user has to do is move the file. Each DST is stored within subfolders that define the production information, for example:

```
/sphenix/tg/tg01/bulk/dNdeta_INTT_run2023/data/simulation/ana.399/EPOS/fullSim
/magOff/detectorAligned/dstSet_00000
```

All simulations appear in the directory `/sphenix/tg/tg01/bulk/dNdeta_INTT_run2023/data/simulation/` then subfolders define the software stack, generator, whether the GEANT4 simulation of sPHENIX was enabled, whether the detectors were aligned in GEANT4 and what DST revision you're looking at. DST revisions are automatically handled when the job launches. If a DST already exists with the same settings in storage then the new DST is placed into a folder with one higher value that the latest stored file, so if an identically tagged file exists `dstSet_00000` then the new file will go to `dstSet_00001`. Further, while a DST is being produced, it will exist in a subfolder called `inProduction` and is automatically moved to the top folder when the job completes. This allows analysers to immediately use DSTs while condor is still producing the rest of the data set without worrying about using unreadable files.

The second method to store production data involves a text file that is written along side the DST. This text file contains all the production information as well as the seeds used for that production so each DST can be exactly recreated if needed. The form of the text file is

Listing 1: Example metadata file

```
====== Your production details ======
Production started: 2024/01/22 16:47
Production Host: spool1068.sdcc.bnl.gov
Folder hash: 281626f
Software version: ana.399
Output file: dNdeta-sim-EPOS-000-00000.root
Output dir: /sphenix/tg/tg01/bulk/dNdeta_INTT_run2023/data/simulation/
ana.399/EPOS/fullSim/magOff/detectorAligned
Number of events: 400
Generator: EPOS
fullSim: true
turnOnMagnet: false
idealAlignment: true
=====================================
```

```
Seeds:
PHRandomSeed::GetSeed() seed: 2677558228
PHRandomSeed::GetSeed() seed: 67770606
PHRandomSeed::GetSeed() seed: 2482422915
PHRandomSeed::GetSeed() seed: 969717365
PHRandomSeed::GetSeed() seed: 4082588279
PHRandomSeed::GetSeed() seed: 1008239460
PHRandomSeed::GetSeed() seed: 280233077
PHRandomSeed::GetSeed() seed: 527826680
PHG4MvtxDigitizer random seed: 527826680
PHRandomSeed::GetSeed() seed: 3802774622
PHG4InttDigitizer random seed: 3802774622
PHRandomSeed::GetSeed() seed: 1263913743
SEEDS: PHRandomSeed::GetSeed() seed: 2677558228
PHRandomSeed::GetSeed() seed: 67770606
PHRandomSeed::GetSeed() seed: 2482422915
PHRandomSeed::GetSeed() seed: 969717365
PHRandomSeed::GetSeed() seed: 4082588279
PHRandomSeed::GetSeed() seed: 1008239460
PHRandomSeed::GetSeed() seed: 280233077
PHRandomSeed::GetSeed() seed: 527826680
PHG4MvtxDigitizer random seed: 527826680
PHRandomSeed::GetSeed() seed: 3802774622
PHG4InttDigitizer random seed: 3802774622

md5sum:
5a3910480142d71865188235bce6bba1
```

The last method to maintain the metadata is the use of a storage node directly in the DST. This means that even if the DST is downloaded and renamed then a user can access this node and print out the production details, including the seeds.

The simulation framework along with the metadata class is stored on github. Before each production is launched, the changes to the repository are pushed to github as part of the metadata information is to record the git hash of simulation framework so that this can be checked out to exactly reproduce any DST at a later date. The framework can be found at https://github.com/cdean-github/dNdeta_sPHENIX_simulations/.

The beampipe, MBD, MVTX, and INTT were simulated using Geant4 with modified geometry based on a preliminary alignment study [38, 39]. In particular, significant effort was made to update the INTT Geant4 geometry according to the survey measurements, as detailed in Appendix B.

The three INTT calibrations – the hit BCO, hot/dead/cold channel masks, and the analog-to-digital conversion map – are centrally maintained in the sPHENIX Calibration Database. These calibrations are accessed by the simulation setup through the relevant production tag (Table 2).

3.1 Primary charged hadron definition

In line with previous measurements at RHIC and LHC, the "primary" charged-hadrons are defined as prompt charged-hadrons and decay products of particles with proper decay length $c\tau < 1\,\mathrm{cm}$, where c is the speed of light in vacuum and τ is the proper lifetime of the particle. This definition excludes contributions from prompt leptons, decay products of particles with longer lifetimes, and secondary interactions. The selection criteria corresponding to the technical definition of "primary" charged hadrons are as follows:

1. The particle is a primary PHG4Particle, or equivalently, a final-state HepMC::GenParticle without a decay vertex, with a status of 1. Proper Lorentz rotation and boost are applied to account for the beam crossing and shifted vertex. This criterion excludes particles from secondary interactions
2. The particle is stable
3. The particle has a charge $\neq 0$
4. The particle is classified as a meson or baryon

3.2 Z-vertex reweighting

Figure 12 shows the vertex Z position reconstructed by INTT tracklets, detailed in Section 5.4.3. The data-to-simulation ratio is used as a per-event weight and applied to the simulation, ensuring the vertex Z position matches that observed in the data. For events with $-10\,\mathrm{cm} \leq \mathrm{vtx_Z} \leq 10\,$ cm, the reweighting factors are consistent with 1.

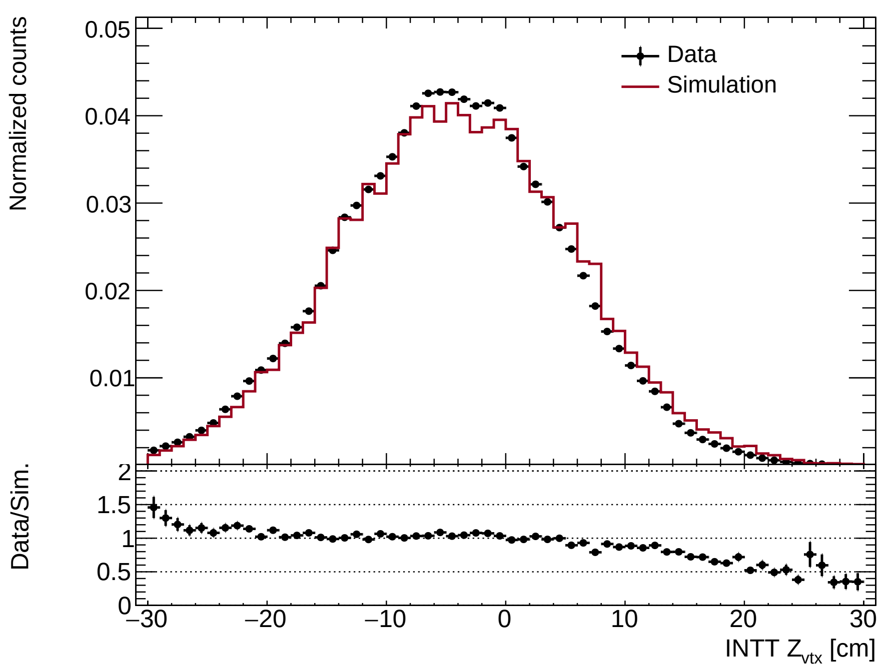

Figure 12: Distribution of the vertex Z position reconstructed by INTT tracklets in data and simulation (top panel), and the ratio of data to simulation (bottom panel).

4 Toolkit

The following list summarizes the analysis tools:

- dNdEta Fun4All ntuplizer: This Fun4All analysis module reads data and simulation DSTs and produces analysis ROOT trees. The module can be found at https://github.com/sPHENIX-Collaboration/analysis/tree/master/dNdEta_Run2023/dNdEtaINTT, while the corresponding Fun4All macros could be found at https://github.com/sPHENIX-Collaboration/analysis/tree/master/dNdEta_Run2023/macros.
- dNdEta analysis codes: The analysis codes perform the offline beamspot reconstruction, per-event vertex Z position reconstruction, tracklet reconstruction and counting, correction factor calculation and application, systematic uncertainty, and plotting utilities. The codes can be found at
  - The PHOBOS-approach analysis: https://github.com/ChengWeiShih/INTT_dNdeta_repo/tree/main/NewCode2024
  - The CMS-approach analysis: https://github.com/sPHENIX-Collaboration/analysis/tree/master/dNdEta_Run2023/analysis_INTT

5 Analysis

5.1 Centrality

The centrality determination used in this analysis was taken from the MBD and ZDC information. The sEPD was not in use at the time of the data collection. The information was taken from the centralised sPHENIX production area using the tags listed in table 2 and was calculated according to the procedure documented by Dan Lis and Jamie Nagle [34]. In this analysis, we have access to

- the Min. Bias trigger decision,
- the event number,
- the clock value,
- the from end module (FEM) clock value,
- the centrality,
- the Z vertex as determined by the MBD,
- the MBD north and south charge sums,
- the total MBD charge
- the MBD north/south charge asymmetry.

By requiring the Min. Bias and the scaled trigger bit, the centrality determination is stable up to the maximal centrality value derived, as can be seen in Figure 13. The centrality compared to the MBD Z vertex is shown in Figure 14, where no correlation between the two variables is found.

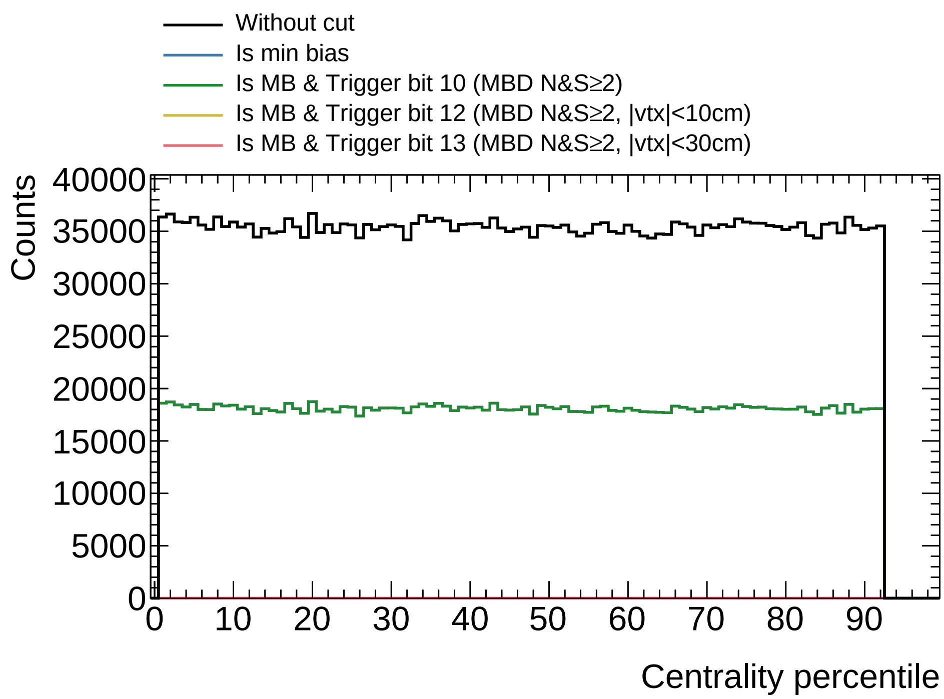

Figure 13: Centrality determined for run 54280 after applying the Min. Bias and the scale trigger bit.

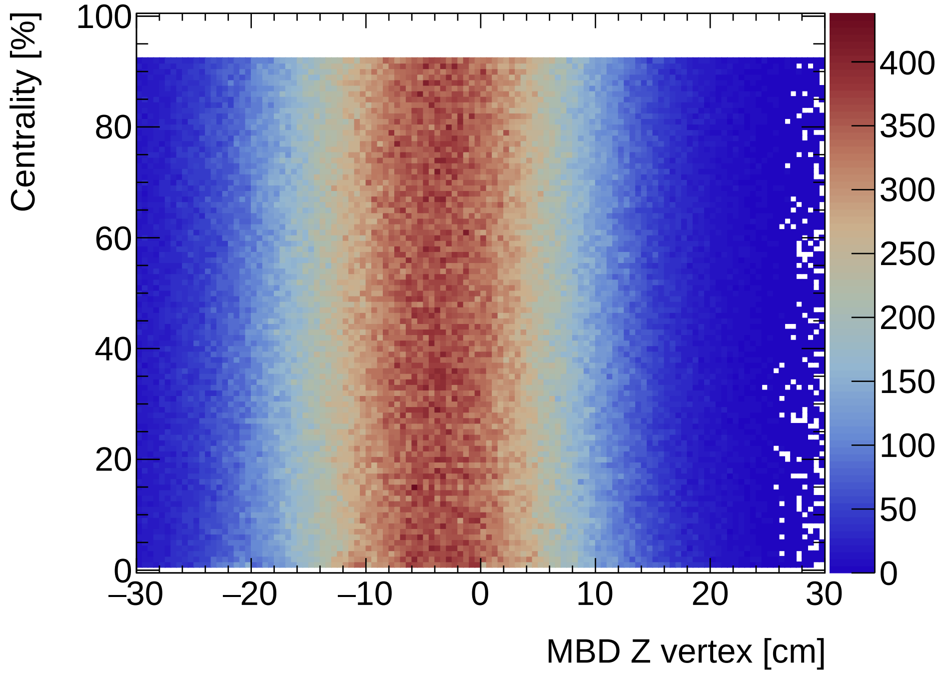

Figure 14: Centrality determined for run 54280 after applying the MIN. BIAS and the scale trigger bit, compared to the MBD-determined Z-vertex.

5.2 Cluster reconstruction

After the extraction of INTT hits from the event DST, the next step in reconstruction for this analysis is the formation of clusters of adjacent hits. These clusters ideally represent the full extent of the deposit of energy from a particular charged particle passing through a layer of the INTT, and contain information about that deposit's location, timing, size, and energy.

5.2.1 INTT clustering algorithm

The clustering of hits in the INTT is implemented using an adjacency graph, where each hit is represented as a node, and two nodes are connected by an edge if their corresponding hits are adjacent. The clusters then correspond to the connected components of this graph. Full implementation details can be found in `https://github.com/sPHENIX-Collaboration/coresoftware/blob/master/offline/packages/intt/InttClusterizer.cc`.

The characteristics of the clusters formed using this method depend on the criteria by which two hits are determined to be "adjacent." Several definitions were considered:

1. Standard clustering: two INTT hits are adjacent if and only if they are in the same column (corresponding to the same coordinate in z) and their edges touch in the ϕ direction. This is the current default definition in the INTT clusterizer.

2. Standard Z-clustering: two INTT hits are adjacent if and only if either the corners or the edges of their corresponding strips touch. In other words, hits are adjacent if

and only if their row and column coordinates both differ by at most one. This is the definition currently used in the MVTX clusterizer and can be enabled in the INTT clusterizer.

3. Modified Z-clustering: two INTT hits are adjacent if and only if the edges of their corresponding strips touch. In other words, hits are adjacent if and only if their row and column coordinates differ by at most one, excluding the case where both differ by exactly one. (See Figure 15 for an example of how this differs from definition 2.)

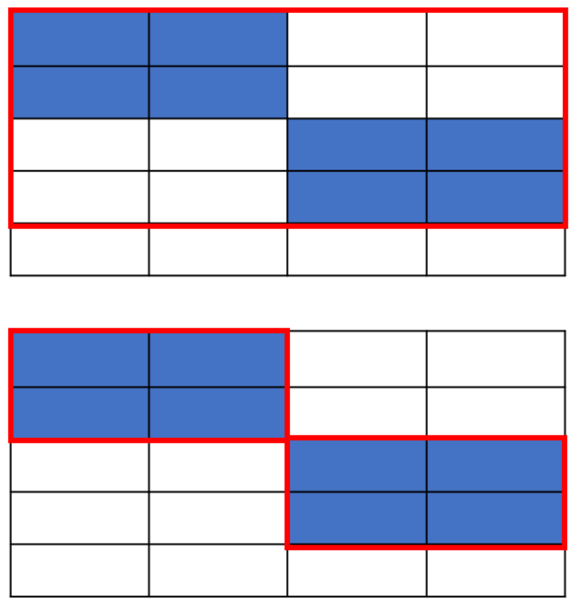

Figure 15: Illustration of one case in which the definitions of adjacency lead to differing results. In the top plot, the second definition of adjacency (including strip corners) is used, in which one cluster, outlined here in red, is formed. In the bottom plot, the third definition of adjacency (excluding strip corners) forms two clusters.

A comparison of the performance of each of these adjacency definitions required the development of a benchmark for clustering performance in simulation.

5.2.2 Clustering performance benchmarks

To objectively compare the effects of changes to the INTT clustering algorithm and its configurable settings, a method for evaluating the performance of the INTT clusterizer on simulated hits was developed. This method evaluates how well a clustering algorithm replicates the following two features of an ideal clustering algorithm:

1. All of the hits created by a given truth particle within a given layer are contained in exactly one reconstructed cluster, and

2. Each reconstructed cluster contains the hits created by exactly one truth particle.

These two features suggest two corresponding histograms as figures of merit:

1. The number of reconstructed clusters associated with the hits generated by a given truth particle, and
2. The number of truth particles associated with the hits contained in a given reconstructed cluster.

For an ideal clustering algorithm, in a detector with an extremely fine-grained sensor layout, the entries in both histograms should be entirely concentrated at a value of exactly 1. Deviations from this are generated both by coarse-grained sensor layouts and by shortcomings in the clustering algorithm used; this means that, for a given fixed sensor layout, the relative difference between these sets of histograms provides a direct comparison of clustering performance.

In order to make this comparison maximally compatible with the way that the INTT clusterizer operates, the reconstructed hits associated with each truth particle were grouped by TrkrHitSet, and the subsequent comparison with reconstructed clusters occurred only within the relevant TrkrHitSet. The method outlined here is implemented in the dNdEtaINTT Fun4All ntuplizer.

The results of this comparison, for hits simulated using the HIJING generator, applied to all three definitions of hit adjacency, are shown in Figure 16.

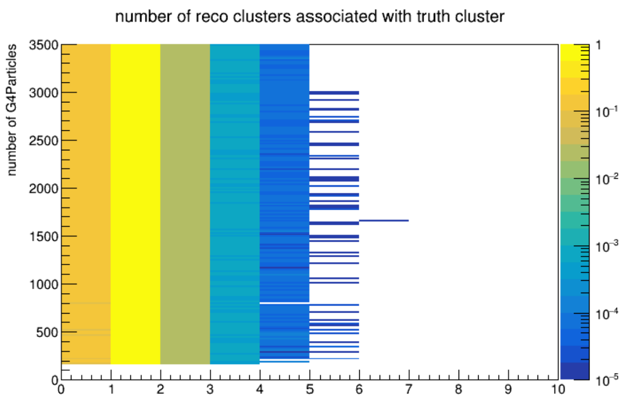

(a) Standard clustering, criterion 1

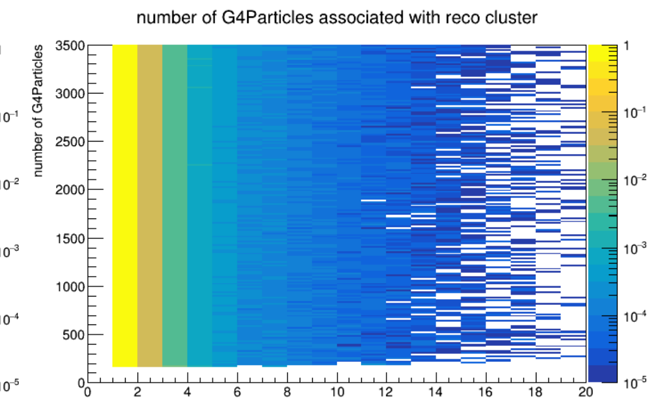

(b) Standard clustering, criterion 2

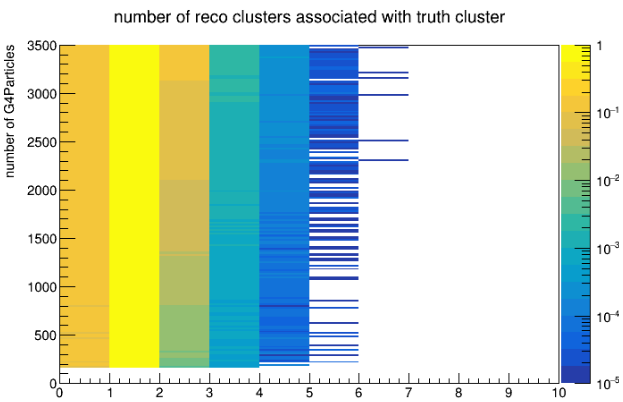

(c) Standard Z-clustering, criterion 1

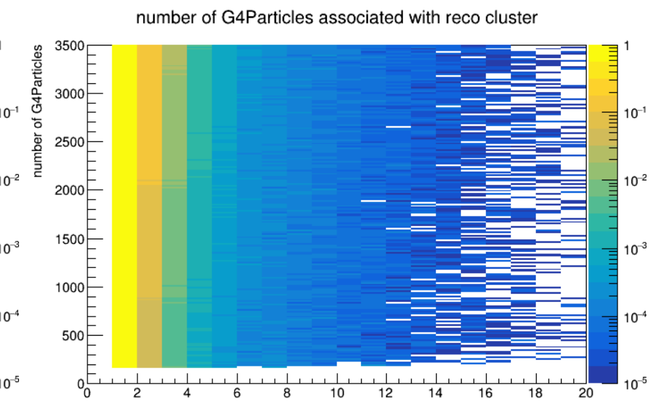

(d) Standard Z-clustering, criterion 2

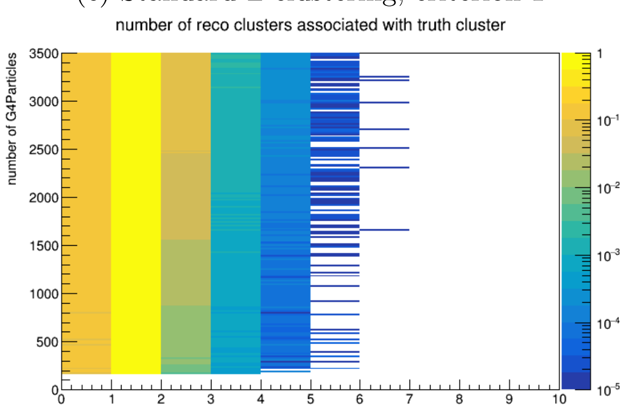

(e) Modified Z-clustering, criterion 1

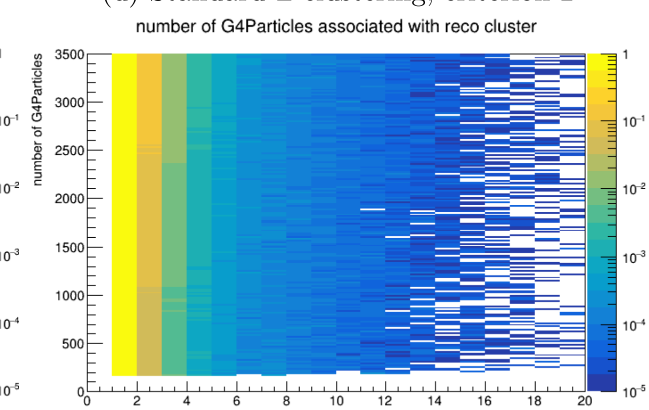

(f) Modified Z-clustering, criterion 2

Figure 16: Clustering performance comparison, differentially in occupancy, normalized within occupancy bins.

Given that the latter two definitions are seen to have a multiplicity-dependent performance, they will not be used for further portions of this analysis; subsequent sections proceed with the standard definition of adjacency in the default INTT clusterizer, which fixes the INTT cluster size in the Z-axis to be 1.

5.2.3 Background cluster removal/mitigation

A cluster ADC threshold of > 35 was applied to exclude single-hit clusters with minimal hit ADC values, as those clusters are predominantly noise. Figure 17 shows the distribution of cluster ADC for clusters with a ϕ-size of 1. The threshold of ADC > 35 effectively rejects noise hits while retaining more than 99% of the signal. The $dN_{ch}/d\eta$ measurements with and without this cluster ADC requirement were compared, and the variation in the $dN_{ch}/d\eta$ distribution was quoted as a source of systematic uncertainty.

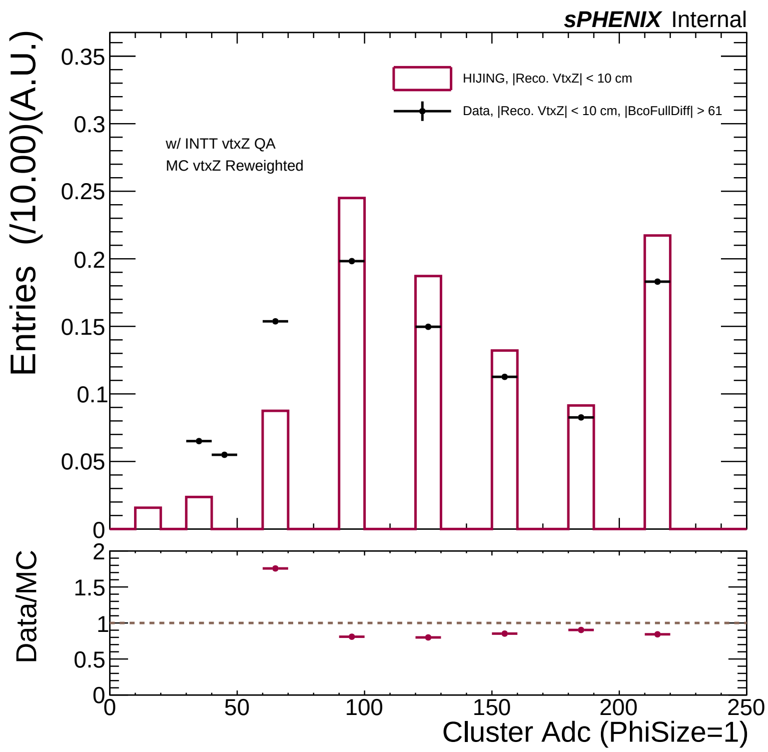

Figure 17: The cluster ADC distribution for clusters with a ϕ-size of 1.

5.2.4 Cluster distributions

The basic distributions of the clusters are shown in this section. Figure 18 shows the comparisons of the number of clusters in the INTT inner layer between data and HIJING simulation. The distributions shown are normalized to the number of events in data.

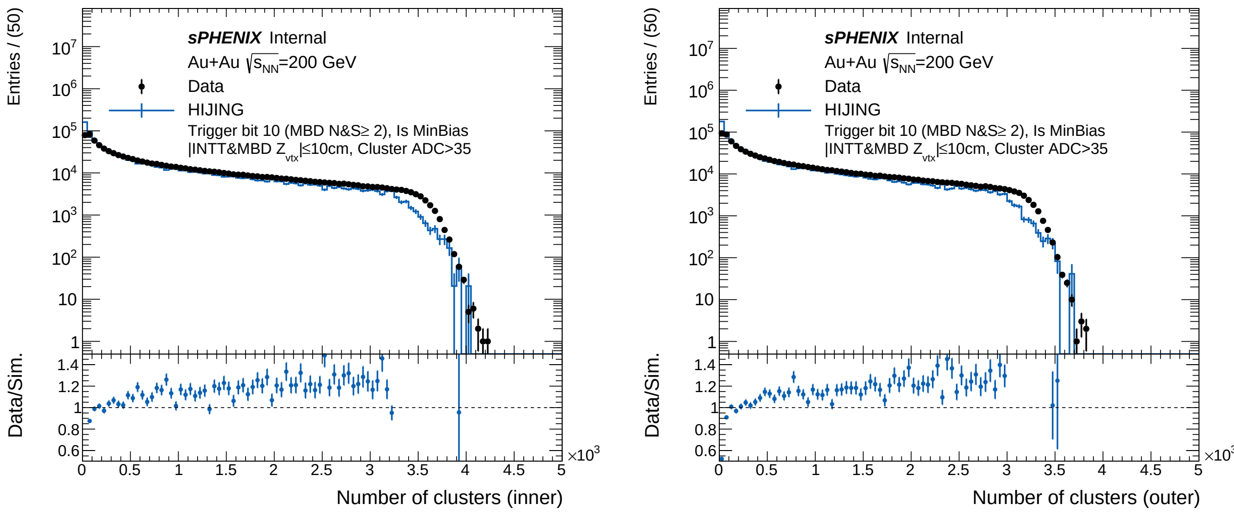

Figure 18: The number of clusters in the INTT inner (left) and outer (right) layer in data and HIJING simulation.

Figure 19 shows the cluster ϕ (left) and η (right) distributions in data and simulation, where ϕ and η are calculated with respect to the event vertex.

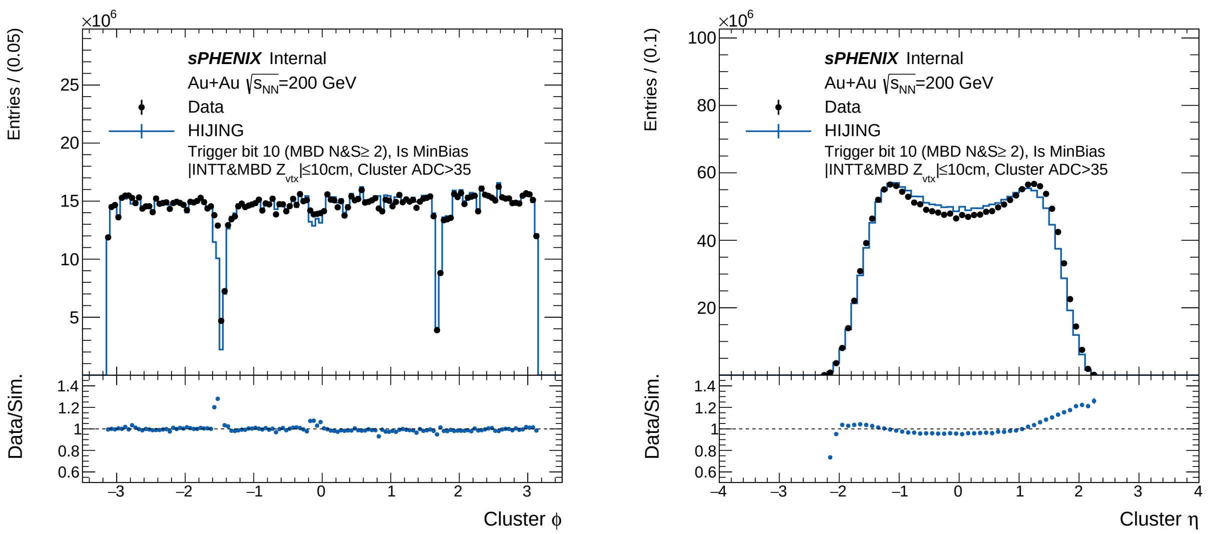

Figure 19: The cluster ϕ (left) and η (right) distribution in data and simulation.

Figure 20 shows the cluster ϕ-size (left), defined as the number of strips in the ϕ direction, and ADC (right) distribution in data and simulation. Discrepancies between data and simulation are seen in both variables. A dedicated study and an attempt to reproduce data distributions in simulation can be found in Appendix D. The impact of large ϕ-size clusters on tracklet reconstruction is studied by comparing the ϕ-sizes of constituent clusters in tracklets, detailed in Sec. 5.5.2. The discontinuity observed in the cluster ϕ-size around 50 and in the cluster ADC near 10×10^3 can be explained as follows: If a cluster has a sufficiently large energy deposit to extend over a range in the ϕ direction, it is more likely to span two or more strips in the Z direction (i.e., with a cluster Z-size ≥ 1). However, since Z-clustering is disabled by default, as explained in Sec. 5.2.1, this introduces a truncation effect in both variables at large values.

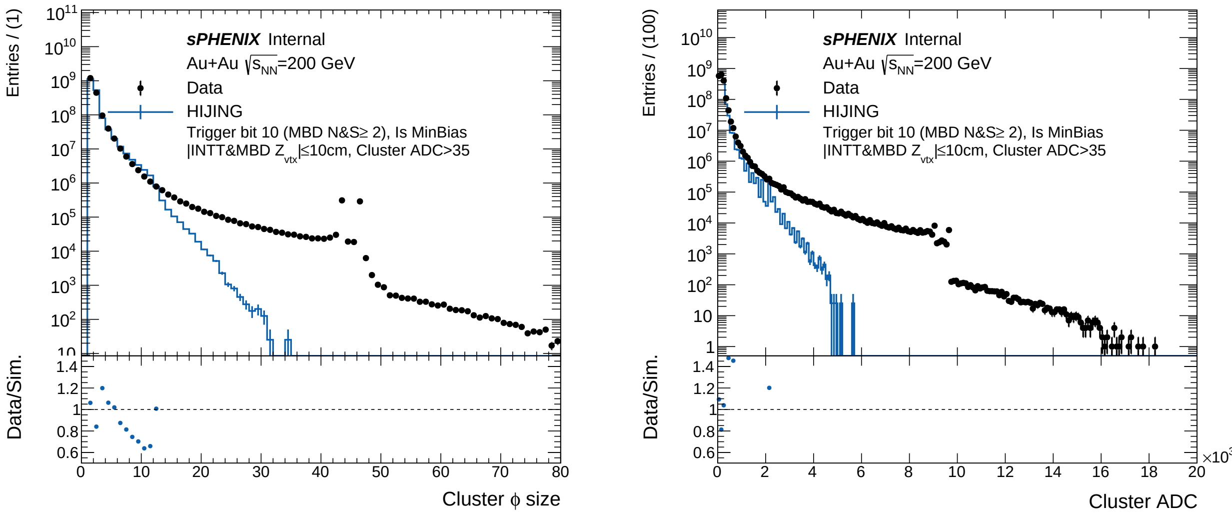

Figure 20: The cluster ϕ-size (left) and ADC (right) distribution in data and simulation.

The two distinct spikes observed in the distributions of cluster ϕ size and cluster ADC were investigated. Figure 21 shows a cutoff in the tail of the distribution showing the number of hits recorded by a single chip within 1 BCO during a single Fun4All event, indicating chip saturation. Specifically, a single chip can record a maximum of 73 hits in one BCO. The cause of this saturation is illustrated in Figure 22. For instance, if a chip has 100 channels fired within one BCO, it takes 100 BCOs for the chip to read out and send the hits to the INTT Read-Out Card (ROC). The ROC then forwards the hits downstream to the INTT FELIX server. When the FELIX server detects the first hit with a given BCO, it starts an open_time window to collect subsequent hits with the same BCO. Any hits arriving after this predefined window are rejected. In this example, 40 hits would be discarded.

An example of a hit map of a saturated chip is shown in Figure 23. A distinct feature of a chip experiencing saturation is a hit map pattern consisting of a large contiguous chunk and zebra-like crossing streaks. The cluster ϕ-size distribution for saturated chips is shown in Figure 24. Three prominent spikes are observed in the distribution: the spike at 2 corresponds to the thickness of the zebra-like crossing, while the spikes at 43 and 46 represent the cluster sizes of the large chunks.

Based on this analysis, we conclude that the two spikes observed in Figure 20 are partially attributed to chip saturation.

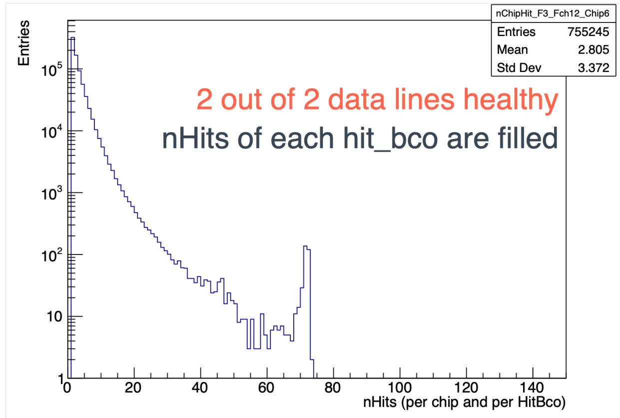

Figure 21: The number of hits of one chip in single BCO of one Fun4All event.

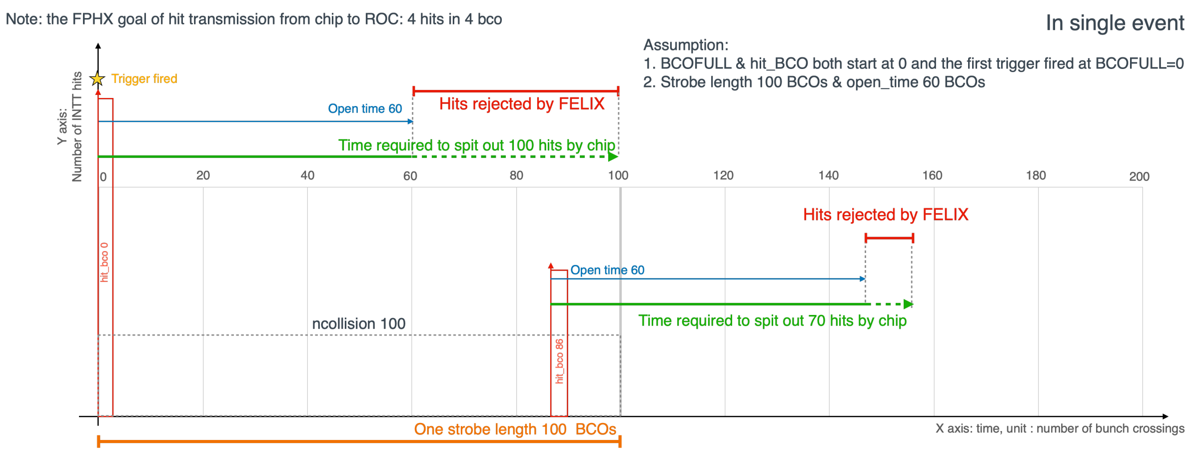

Figure 22: The illustration of INTT chip saturation issue.

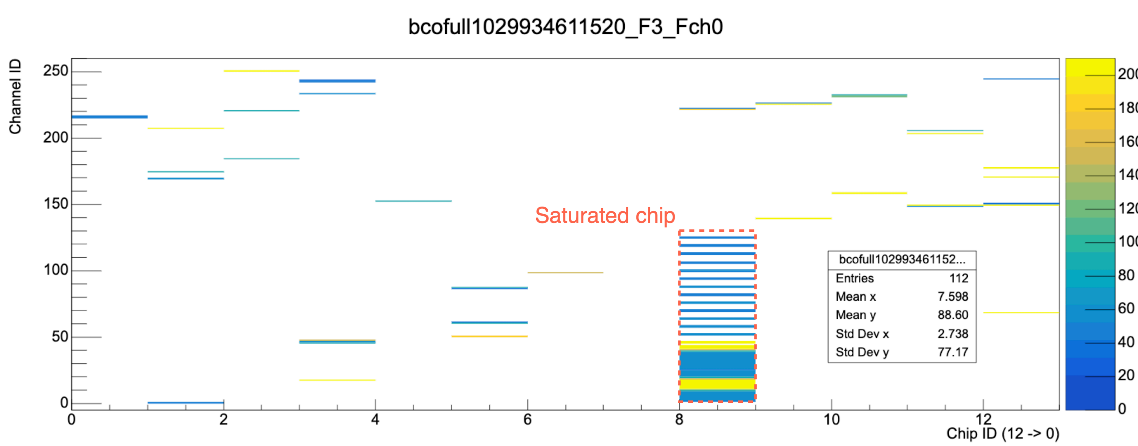

Figure 23: The hit map of one INTT half-ladder with chip saturated of one event.

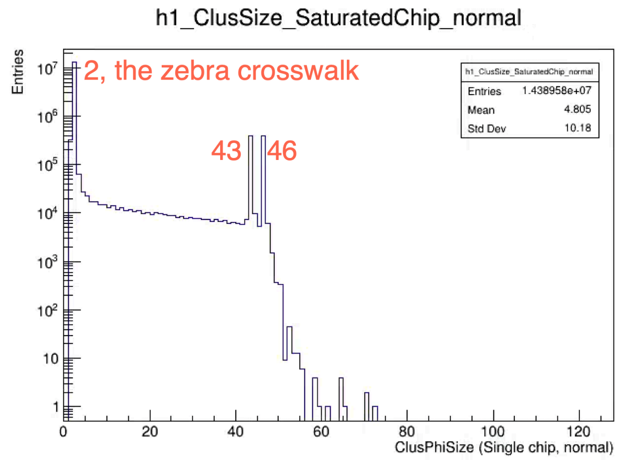

Figure 24: The cluster ϕ size distribution of the saturated chips.

The baseline analysis applies a cluster ϕ-size cut < 40, which retains all clusters in simulation but excludes clusters with a large ϕ-size in data. The analysis is repeated without the cluster ϕ-size requirement and the resulting variation in the measured $\mathrm{dN_{ch}}/\mathrm{d}\eta$ is used as a corresponding systematic uncertainty.

5.3 Tracklet analysis overview

Tracklets are defined as combinations of two clusters with a small angular separation in two detector layers. Clusters originating from a particle track associated with the event vertex exhibit small differences in pseudorapidity ($\Delta\eta$), azimuthal angle ($\Delta\phi$), and angular separation (ΔR). These three key quantities characterizing tracklets are defined as follows:

$$\Delta\eta = \eta_{\mathrm{inner}} - \eta_{\mathrm{outer}} \tag{2}$$

$$\Delta\phi = \phi_{\mathrm{inner}} - \phi_{\mathrm{outer}} \tag{3}$$

$$\Delta\mathrm{R} = \sqrt{(\Delta\eta)^2 + (\Delta\phi)^2} \tag{4}$$

Here, $\eta_{\mathrm{inner(outer)}}$ and $\phi_{\mathrm{inner(outer)}}$ represent the pseudorapidity and azimuthal angle of the cluster in the inner (outer) layer of the INTT, calculated with respect to the event vertex. Both vertex reconstruction and tracklet counting utilize the fact that tracklets associated with particles originating from the event vertex produce a coincidence peak in the $\Delta\eta$, $\Delta\phi$, and ΔR distributions. These processes are further detailed in the following subsections.

5.4 Vertex reconstruction using tracklets

The vertex reconstruction for the baseline tracklet analysis consists of two steps. The first step determines the beamspot position, specifically the average X and Y positions of the vertex (v_x and v_y), while the second step reconstructs the per-event vertex Z position. Two independent methods have been developed for beamspot determination, yielding consistent results.

5.4.1 Beam spot determination - Approach 1: DCA-ϕ fitter

The distance-of-closest-approach (DCA)-ϕ fitter closely follows Ref. [40]. This approach takes advantage of the fact that, for tracks originating from a beamspot at (x_0, y_0), the distance of closest approach to the origin follows a sinusoidal pattern with respect to the ϕ coordinate of the point of closest approach (PCA) to the origin (ϕ_{PCA}):

$$\text{DCA}(\phi_{\text{PCA}}) = R_0 \cos(\phi_{\text{PCA}} - \phi_0)$$

where $R_0 = \sqrt{x_0^2 + y_0^2}$ is the beamspot radial coordinate and $\phi_0 = \arctan\left(\frac{y_0}{x_0}\right)$ is the beamspot ϕ coordinate. Plotting the tracklet DCA and ϕ_{PCA}, as shown in Figure 25, and fitting the resulting sinusoidal ridge allows for the extraction of the two fit parameters R_0 and ϕ_0.

Beamspot reconstruction is performed on sub-samples of data and simulation events with cluster multiplicity $20 < N_{\text{clusters}} < 350$. For each sub-sample, tracklets, constructed by pairs of clusters that pass the cluster ADC cut and with a $\Delta\phi < 0.122$ radians, are selected. Then, the sinusoidal correlation is extracted by profiling the noise-subtracted tracklet DCA and ϕ_{PCA} distribution, constructed by identifying the peak DCA for each slice of ϕ of the point of closest approach, ϕ_{PCA} and removing values less than 99.5% of this peak DCA. A graph is created with the cleaned sinusoidal correlation and fitted with the cosine function to extract R_0 and ϕ_0. Figure 25 and 26 show the tracklet DCA and ϕ_{PCA} distribution in one sub-sample, before the noise removal on the left and after on the right with the graph and cosine function fit, for simulation and data respectively. The final beamspot position is the average of PCA over all sub-samples.

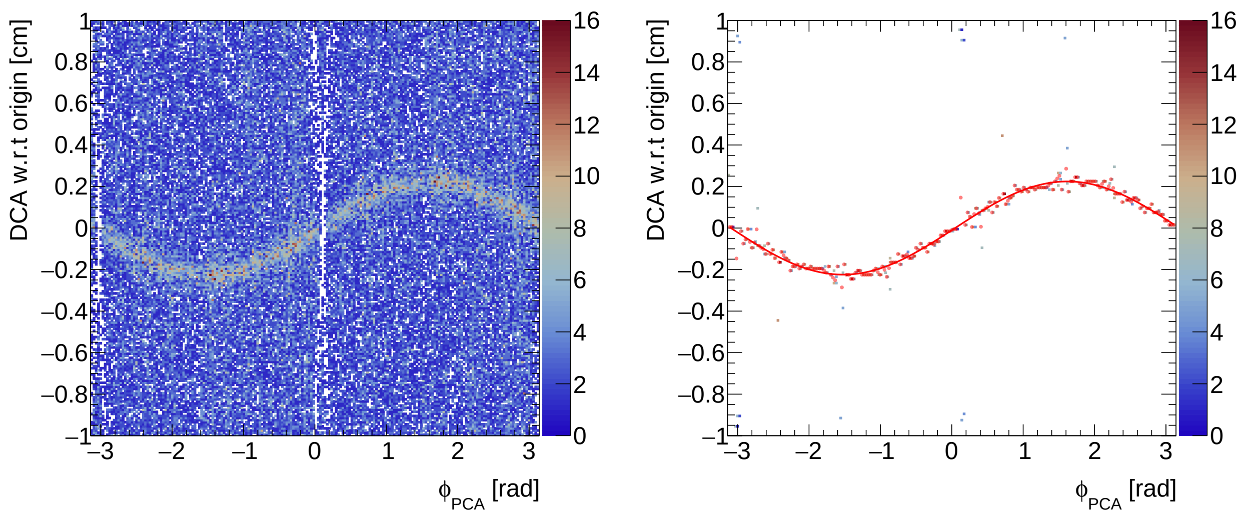

Figure 25: The DCA-ϕ method on simulated data generated with HIJING. (Left) without noise removal; (right) after noise removal and the graph with the cleaned sinusoidal correlation and the fit.

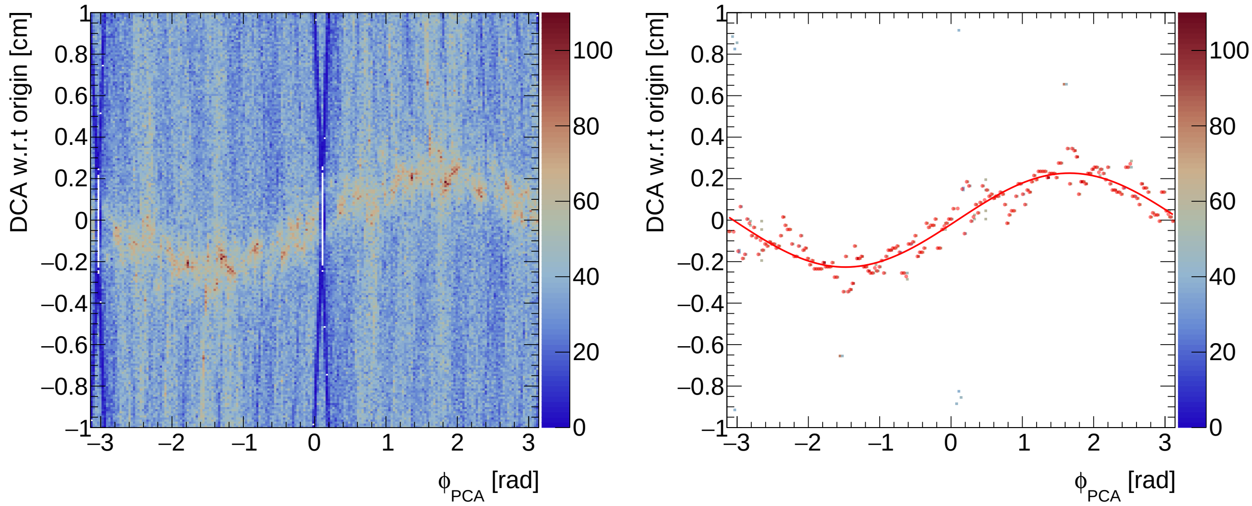

Figure 26: The DCA-ϕ in data. (Left) without noise removal; (right) after noise removal and the graph with the cleaned sinusoidal correlation and the fit.

Figure 27 shows the reconstructed beamspot position as a function of the sub-sample index for simulation events, consistent with the simulated truth vertex position ($v_x^{\text{truth}}, v_y^{\text{truth}} = (-0.022, 0.223)\,\text{cm}$). Figure 28 shows the beamspot position as a function of the median of INTT BCO of the sub-sample in data and indicates that the beamspot position is stable throughout run 54280.

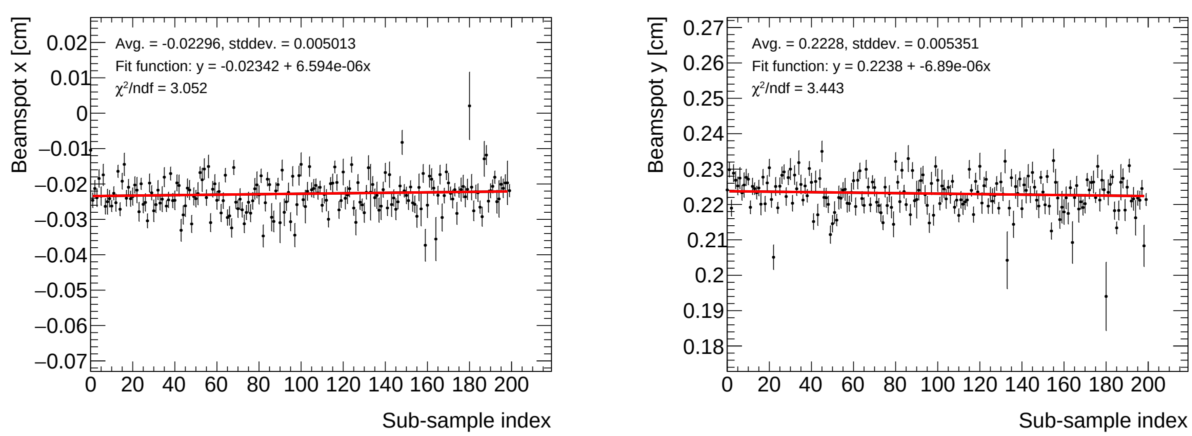

Figure 27: The reconstructed beamspot position as a function of the sub-sample index.

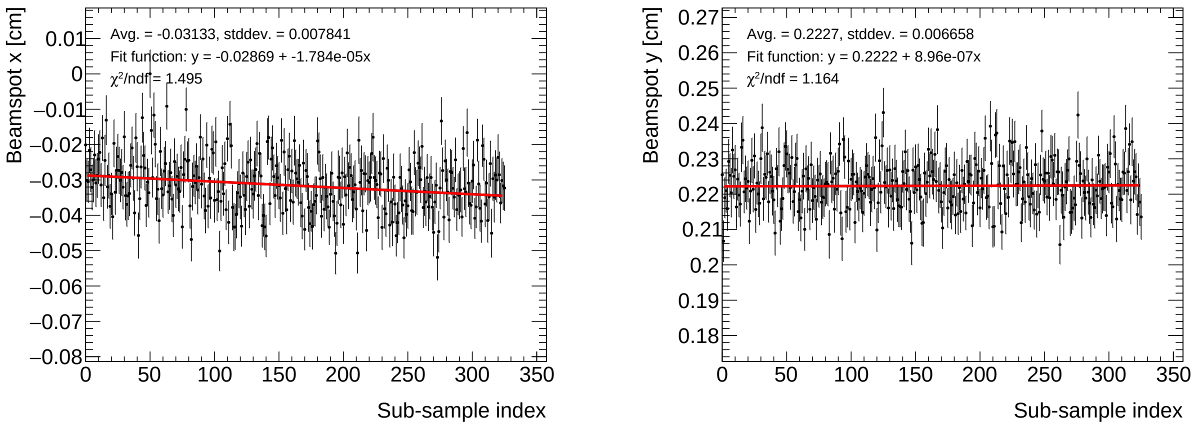

Figure 28: The beamspot position as a function of the median of INTT BCO of the subsample.

5.4.2 Beam spot determination - Approach 2: Iterative quadrant search and 2D tracklet fill

This approach involves two methods to reconstruct the averaged beam spot position. The derived final beam spot is used in the PHOBOS-style analysis.

The procedure of iterative quadrant search is detailed as follows and illustrated in Figure 29:

1. Events are divided into subsamples, each containing 15,000 events.

2. To make sure the sufficient number of tracks reconstructed while minimizing the combinatorial background, only the low-multiplicity events with the number of clusters more than 20 and less than 350 are included.

3. Within each event, start with a cluster in the inner layer and loop through the clusters in the outer layer. Cluster pairs with $\Delta\phi < 0.122$ radian are kept. This step is repeated for all events in a subsample.

4. A square of size 8×8 mm^2 centered at $(x, y) = (0, 0)$ is defined. The corners of the square are considered as vertex candidates. For each candidate, the Distance of the Closest Approach (DCA) and $\Delta\phi$ of the cluster pairs are evaluated. An example 2D histogram of the inner cluster ϕ versus DCA and ϕ versus $\Delta\phi$ for one corner is shown in Figure 30.

5. For each corner, background removal is performed to exclude irrelevant entries. After background removal, the histograms are fitted with a Polynomial-0 function, as shown in Figure31. A Polynomial-0 function is used because DCA and $\Delta\phi$ show no correlation with ϕ when tested against the true vertex, as demonstrated in Figure32. This process is repeated for all four corners of the square.

6. The quadrant containing the corner with the smallest fit errors is selected. Steps 4 and 5 are repeated using a new square formed within the chosen quadrant, with its dimensions halved relative to the previous square.

7. The process is repeated until the size of the square reaches 15µm. The v_x and v_y for the subsample are calculated as the average positions of the corners and the center of the square from the final iteration.

8. The final values of v_x and v_y are obtained by averaging the v_x and v_y values across all subsamples.

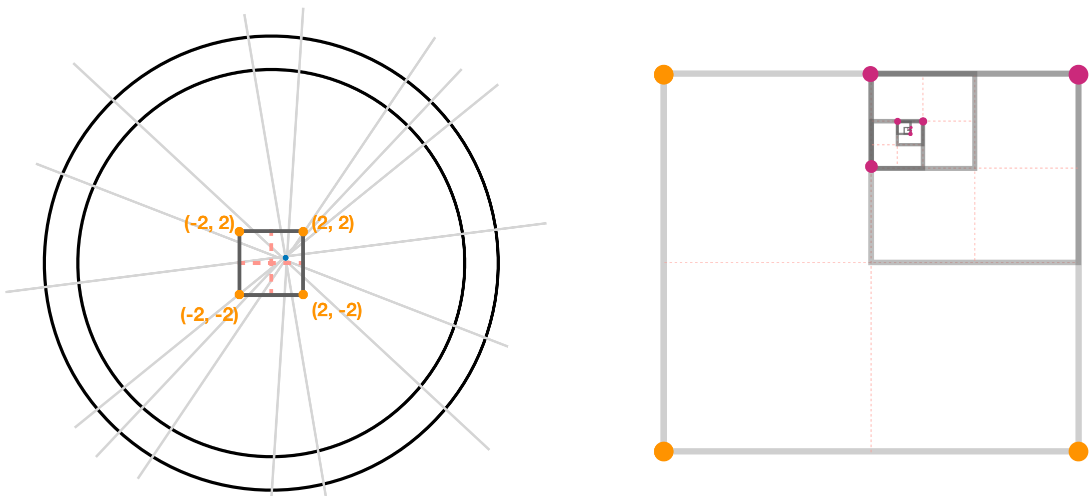

Figure 29: Iterative quadrant search

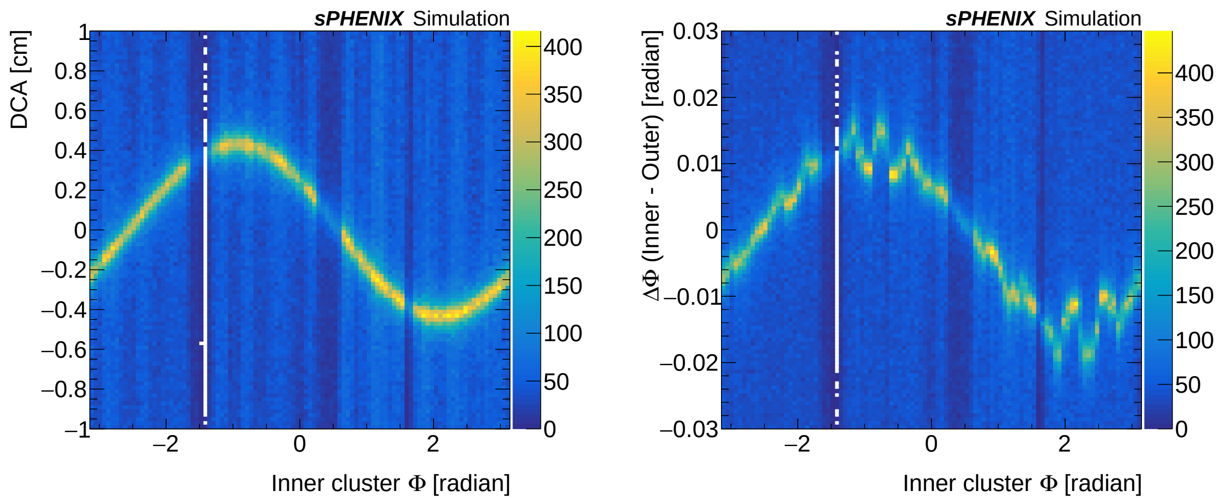

Figure 30: DCA (left) and cluster $\Delta\phi$ (right) as a function of inner cluster phi.

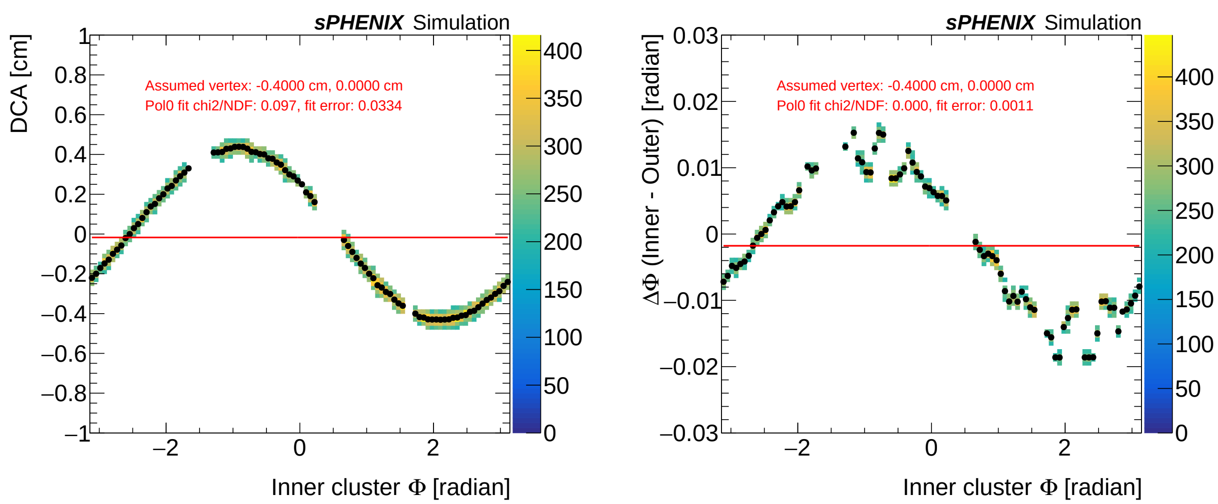

Figure 31: DCA (left) and cluster $\Delta\phi$ (right) as a function of inner cluster phi, post background removal.

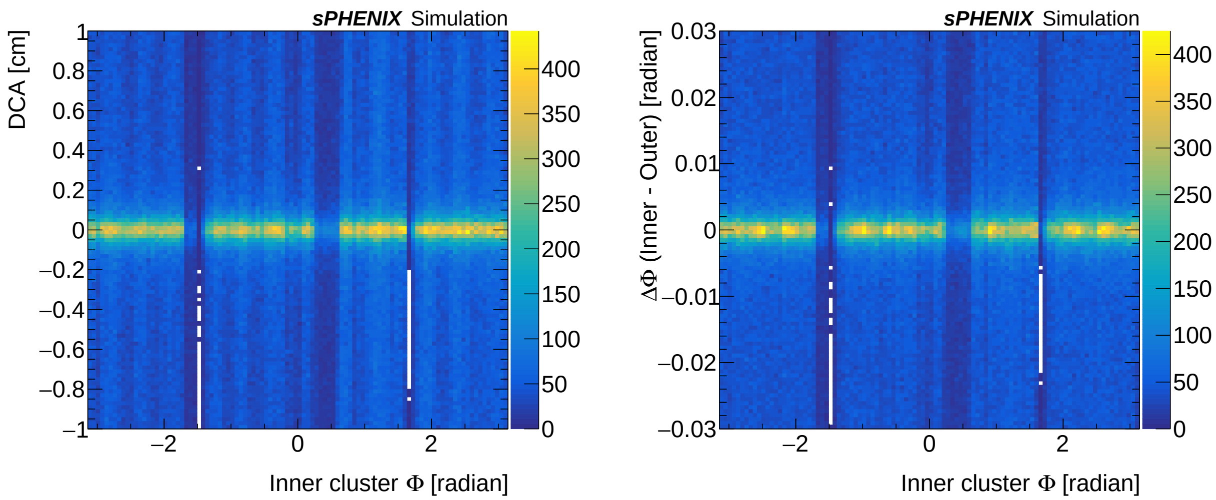

Figure 32: DCA (left) and cluster $\Delta\phi$ (right) as a function of inner cluster phi where the true vertex is taken as the tested vertex.

A closure test is performed in simulation, generated by HIJING, with the truth vertex position set at $(v_x, v_y) = (-0.02204\,\text{cm}, 0.2229\,\text{cm})$. A vertex of $(v_x, v_y) = (-0.02132\,\text{cm}, 0.2235\,\text{cm})$ is obtained from the method, in good agreement with the assigned position.

The 2D tracklet fill method complements the iterative quadrant search. Ideally, the position of the beam spot can be obtained by populating the tracklets into a 2D histogram. Taking the same batch used in the method validation of Approach 2 as an example, the procedures are described in the following:

1. Define the dimensions and center of a finely-binned 2D histogram. The central point is determined by the vertex XY position acquired through Approach 2, which is (-0.02132 cm,0.2235 cm) in the validation test. In the standard configuration, this corresponds to a 0.25 cm $\times$ 0.25 cm square with bin sizes of 50 µm $\times$ 50 µm.

2. Populate the trajectories of the combinations outlined in step 1 of Approach 2 into the 2D histogram. The example is shown in Figure 33.

3. Remove the background of the histogram.

4. The v_x and v_y are obtained by taking the averages on both axes of the histogram, as shown in Figure 33. The vertex position (-0.02167 cm, 0.2230 cm) is obtained. The measurement agrees with truth and the reconstructed vertex of Approach 2.

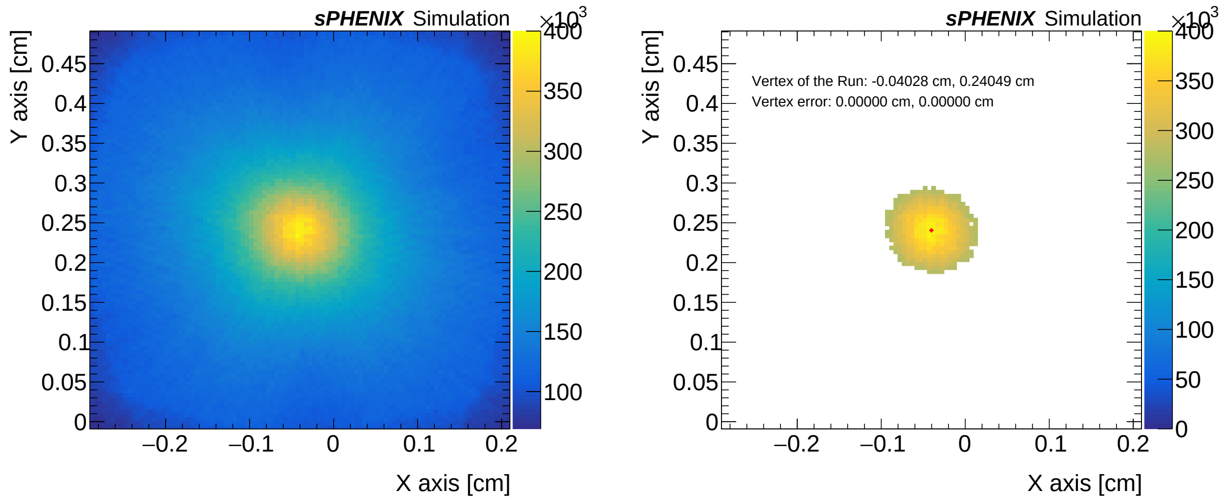

Figure 33: 2D histogram filled by the trajectories of combinations (left) and post background removal (right). The red full cross mark represents the reconstructed vertex XY. Events with a number of $20 < \text{clusters} < 350$ are included.

Figure 34 shows the full closure test of the methods in the simulation. The two methods agree in all the subsamples. And the stability of the vertex X and Y positions in the data is evaluated. Figure 35 shows the average vertex X and Y positions calculated every fifteen thousand events as a function of the averaged event ID in data, measured by the two approaches. The discrepancy between the measured vertices from the two approaches can be attributed to detector misalignment, as discussed in Section 7.1.1. The observed consistency in the vertex positions throughout the run indicates stable performance, supporting the adequacy of reconstructing the tracklets based on the average beam spot. In data, the final beam spot $(v_x, v_y) = (-0.0233\,\mathrm{cm}, 0.2232\,\mathrm{cm})$ was obtained and used in the PHOBOS-style analysis.

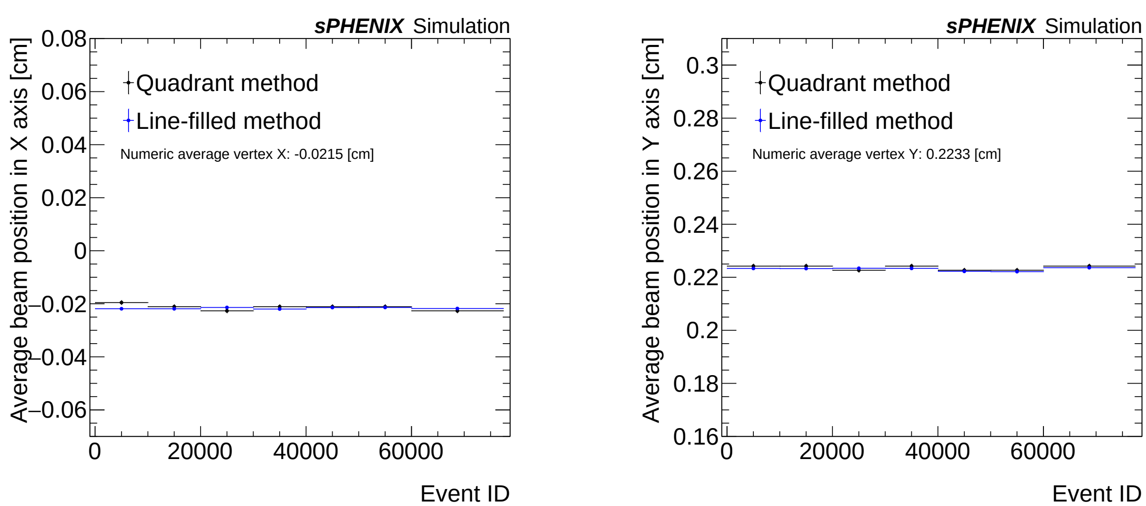

Figure 34: In simulation, vertex positions averaged over every fifteen thousand events as a function of averaged event ID for X position (left) and Y position (right).

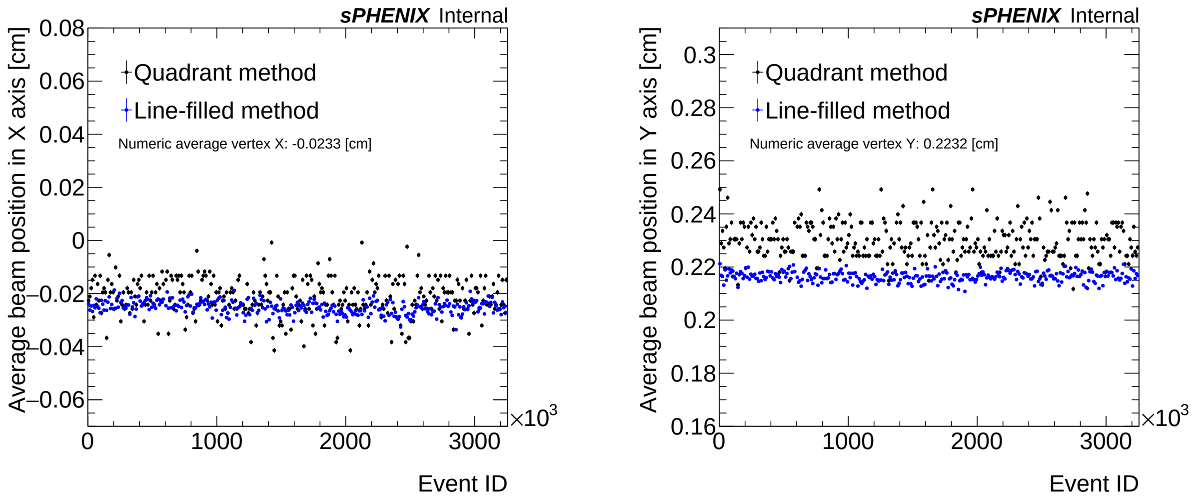

Figure 35: In data, vertex positions averaged over every fifteen thousand events as a function of averaged event ID for X position (left) and Y position (right).

5.4.3 Per-event vertex Z position reconstruction

The lengths of the INTT strips, either 1.6 or 2.0 cm, inherently limit the precision of the vertex Z position. To address this, two reconstruction methods have been developed, both leveraging the fact that a single pair of inner and outer clusters defines only a range within which the vertex could potentially lie.

The first method, adopted in the CMS approach, is described step-by-step below:

1. The cluster ϕ is calculated and updated relative to the beamspot coordinates v_x and v_y.

2. For each cluster in the inner layer, loop through the clusters in the outer layer. Cluster pairs that satisfy $\Delta\phi \leq \Delta\phi_{\text{cut}}$ and $\text{DCA} \leq \text{DCA}_{\text{cut}}$ are retained, where DCA (Distance of Closest Approach) is defined as:

$$\text{DCA} = \frac{|m \cdot v_x - v_y + b|}{\sqrt{m^2+1}} \tag{5}$$

$$m = \frac{y_{\text{outer}} - y_{\text{inner}}}{x_{\text{outer}} - x_{\text{inner}}} \tag{6}$$

$$b = y_{\text{inner}} - m \cdot x_{\text{inner}} \tag{7}$$

$$\tag{8}$$

Here, $x_{\text{outer(inner)}}$ and $y_{\text{outer(inner)}}$ are the X and Y coordinates of the clusters in the outer (inner) layer. Repeat this process for all clusters in the inner layer.

3. Cluster pairs that pass the $\Delta\phi$ and DCA requirements form vertex Z candidates. Each candidate defines a range bounded by two edges, v_z^{edge1} and v_z^{edge2}, which are calculated

by linearly extrapolating from the paired clusters to the beamspot (v_x, v_y). These edges are defined as:

$$v_z^{\text{edge1}} = z_{\text{inner}}^{\text{edge1}} - \rho_{\text{inner}} \cdot \frac{z_{\text{outer}}^{\text{edge2}} - z_{\text{inner}}^{\text{edge1}}}{\rho_{\text{outer}} - \rho_{\text{inner}}} \tag{9}$$

$$v_z^{\text{edge2}} = z_{\text{inner}}^{\text{edge2}} - \rho_{\text{inner}} \cdot \frac{z_{\text{outer}}^{\text{edge1}} - z_{\text{inner}}^{\text{edge2}}}{\rho_{\text{outer}} - \rho_{\text{inner}}} \tag{10}$$

$$\rho_{\text{inner}} = \sqrt{(x_{\text{inner}} - v_x)^2 + (y_{\text{inner}} - v_y)^2} \tag{11}$$

$$\rho_{\text{outer}} = \sqrt{(x_{\text{outer}} - v_x)^2 + (y_{\text{outer}} - v_y)^2}. \tag{12}$$

4. The vertex Z candidate range is divided into fine segments, which are filled into a one-dimensional histogram. Examples of these histograms are shown in Figure 36.

5. The histogram is fitted with a combination of a Gaussian and a constant offset. The mean value of the Gaussian fit is taken as the reconstructed vertex Z position, vtx_z.

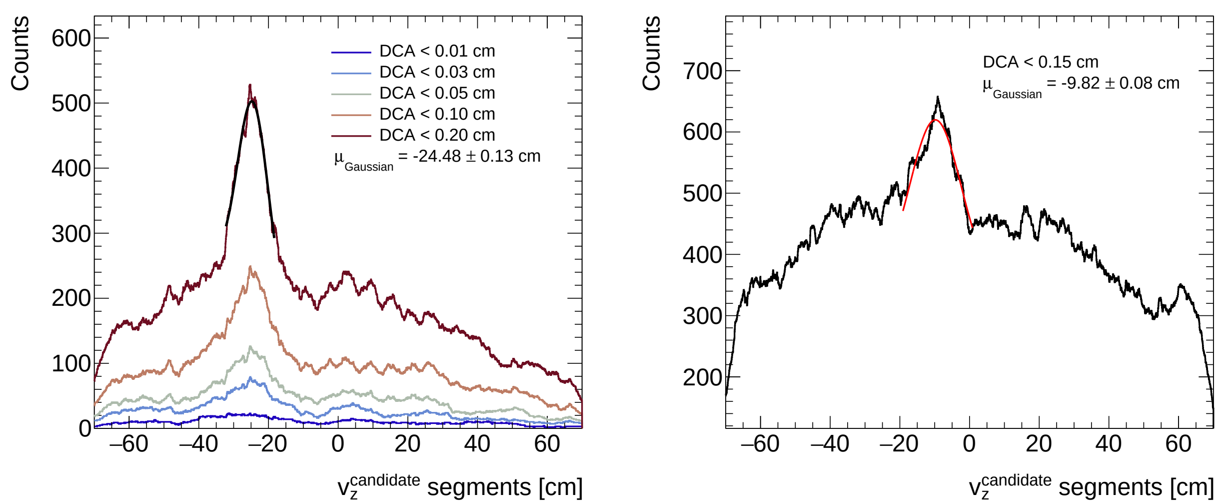

Figure 36: The histogram of segments in simulation (left) and in data (right).

The parameters $\Delta\phi_{\text{cut}}$ and DCA_{cut} are optimized by scanning across ranges of $\Delta\phi$ and DCA to achieve the best vertex reconstruction resolution. Figure 97 in Appendix F illustrates the vertex reconstruction resolution as a function of $\Delta\phi_{\text{cut}}$ and DCA_{cut}. The final selection criteria are determined to be $\Delta\phi_{\text{cut}} = 0.000523$ radians and $\text{DCA}_{\text{cut}} = 0.15\,\text{cm}$ for the analysis.

To quantify the vertex reconstruction bias and resolution, events are subdivided by centrality class. For each centrality interval, the difference between the reconstructed event vertex and the truth event vertex is fitted with a Gaussian distribution. The Gaussian fit's mean value quantifies the reconstruction bias, while the width represents the resolution. Figure 37 shows the bias and resolution of the vertex reconstruction as functions of centrality.

The resolution ranges from 0.175 cm for the most central events to 1.73 cm for the most peripheral events, while the bias remains below 0.05 cm across all centrality classes. Gaussian fits for all centrality classes are shown in Figure 99 in AppendixF.

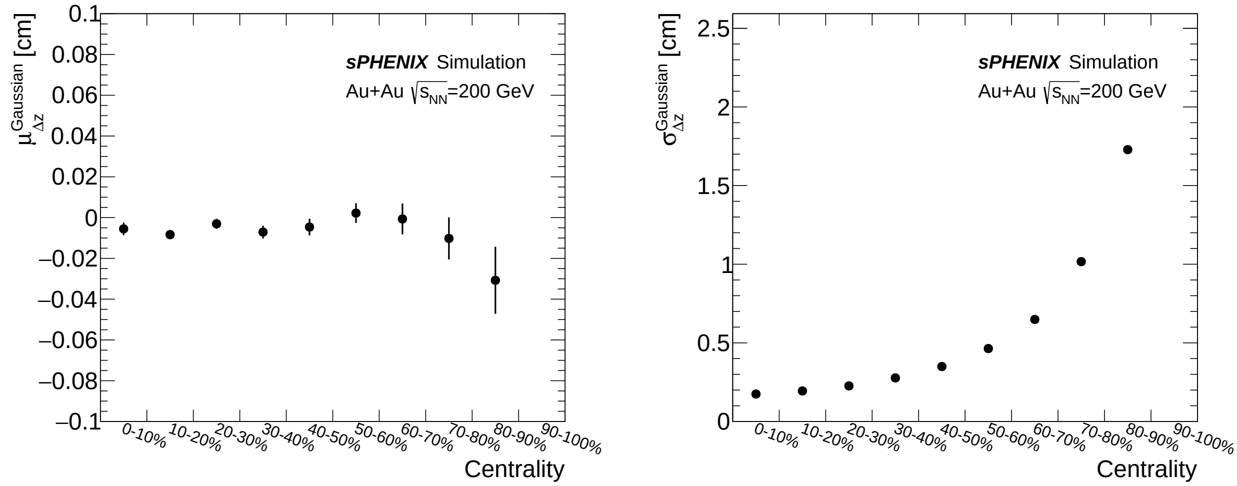

Figure 37: (Left) Vertex reconstruction bias as a function of centrality; (Right) Vertex reconstruction resolution as a function of centrality.

The vertex reconstruction efficiency, $\epsilon_{\mathrm{Reco.\ vertex}}$, defined in Equation 13, is shown as a function of cluster multiplicity and $\mathrm{vtx}_z^{\mathrm{Truth}}$ with a loose quality cut of $|\Delta(\mathrm{vtx}_z^{\mathrm{Reco}}, \mathrm{vtx}_z^{\mathrm{Truth}})| \leq$ 60 cm in Figure 38.

$$\epsilon_{\mathrm{Reco.\ vertex}} = \frac{\text{Number of events with 1 vertex}_{\mathrm{Reco}} \text{ with } |\Delta(\mathrm{vtx}_z^{\mathrm{Reco}}, \mathrm{vtx}_z^{\mathrm{Truth}})| \leq 60\,\mathrm{cm}}{\text{Number of events with 1 vertex}_{\mathrm{Truth}}} \tag{13}$$

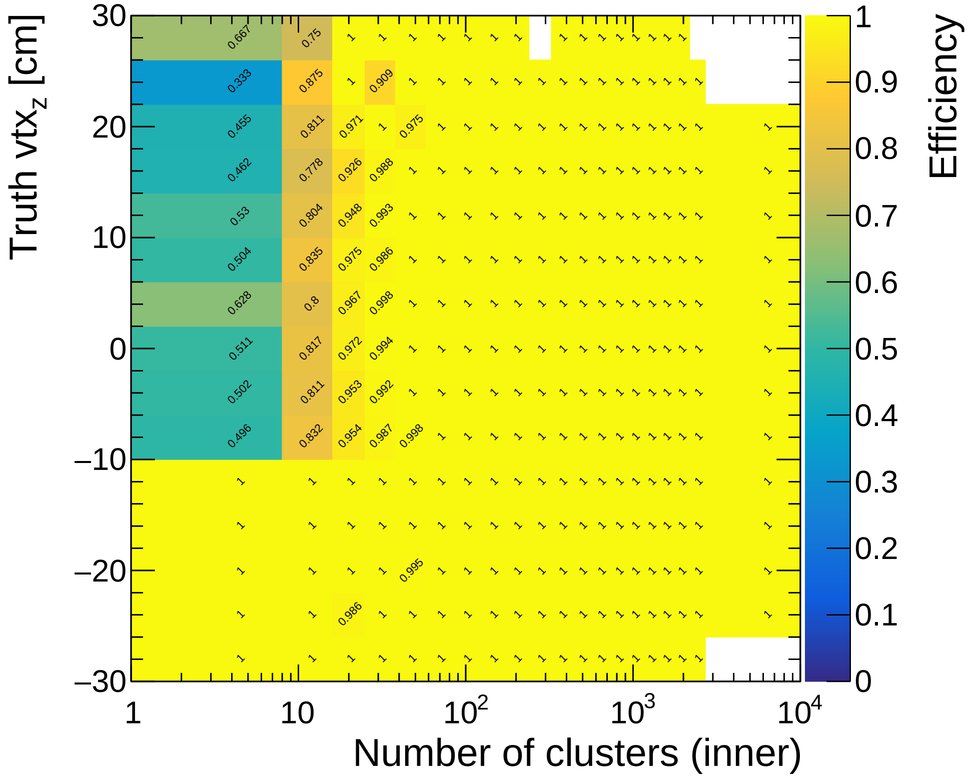

Figure 38: The vertex reconstruction efficiency as a function of cluster multiplicity and $\mathrm{vtx}_z^{\mathrm{Truth}}$.

547 Figure 12 in Section 3.2 presents the reconstructed vertex Z position in both data and simulation. The reconstructed vertex distributions for centrality intervals up to 70% are consistent, as shown in Figure 39.

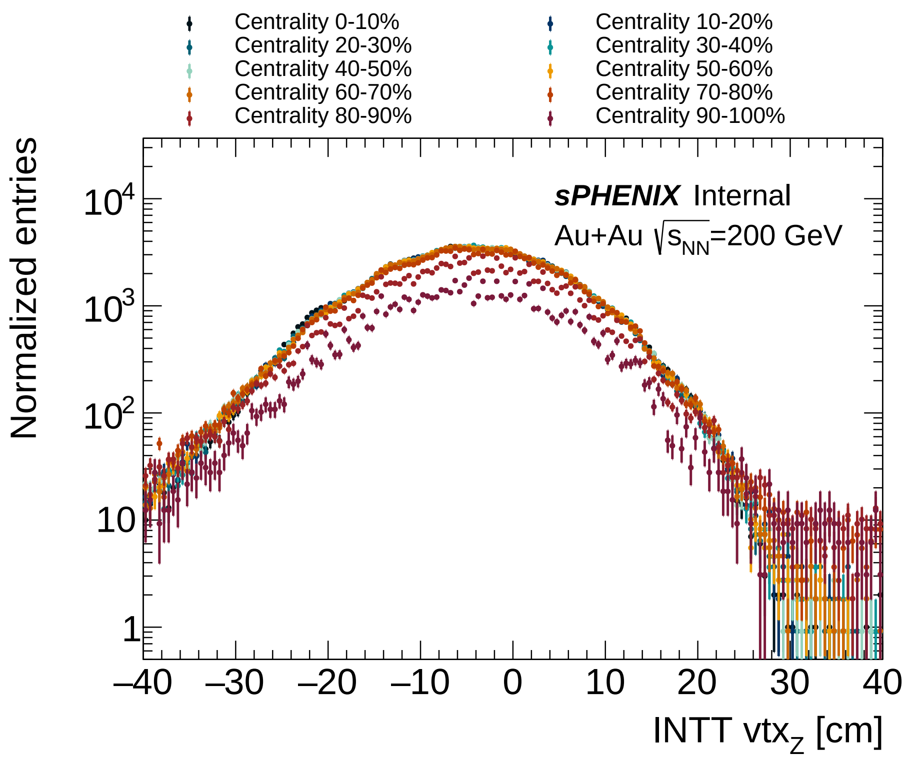

Figure 39: Reconstructed vertex Z position in different centrality intervals in data.

The reconstructed vertex Z distribution in both data and the simulation sample is fitted with a double-sided Crystal Ball (DBCB) function, as defined in Equation 14, and shown in Figure 40. In simulation, the fit results, particularly the mean and sigma values, are consistent, within uncertainties, with the initial vertex position settings. This confirms that the vertex reconstruction does not introduce a systematic bias in the vertex position.

The DBCB function is defined as:

$$\mathrm{DBCB}(z) = \begin{cases} e^{-\frac{1}{2}\cdot(\frac{z-\mu}{\sigma})^2} & , \; -a_L < \frac{z-\mu}{\sigma} < a_H \\ f\cdot(\frac{n_L}{a_L})^{n_L}\cdot e^{-\frac{a_L^2}{2}}\cdot\left[\frac{n_L}{a_L} - a_L - (\frac{z-\mu}{\sigma})\right]^{-n_L} + (1-f)\cdot e^{-\frac{1}{2}\cdot(\frac{z-\mu}{\sigma})^2} & , \; \frac{z-\mu}{\sigma} \le -a_L \\ (1-f)\cdot(\frac{n_H}{a_H})^{n_H}\cdot e^{-\frac{a_H^2}{2}}\cdot\left[\frac{n_H}{a_H} - a_H + (\frac{z-\mu}{\sigma})\right]^{-n_H} + f\cdot e^{-\frac{1}{2}\cdot(\frac{z-\mu}{\sigma})^2} & , \; \frac{z-\mu}{\sigma} \ge a_H \end{cases} \tag{14}$$

where μ is the peak position of the Gaussian component, a_L and a_H define the transitions to the power-law behavior on the low-z and high-z sides, and n_L and n_H are the exponents of the power-law tails.

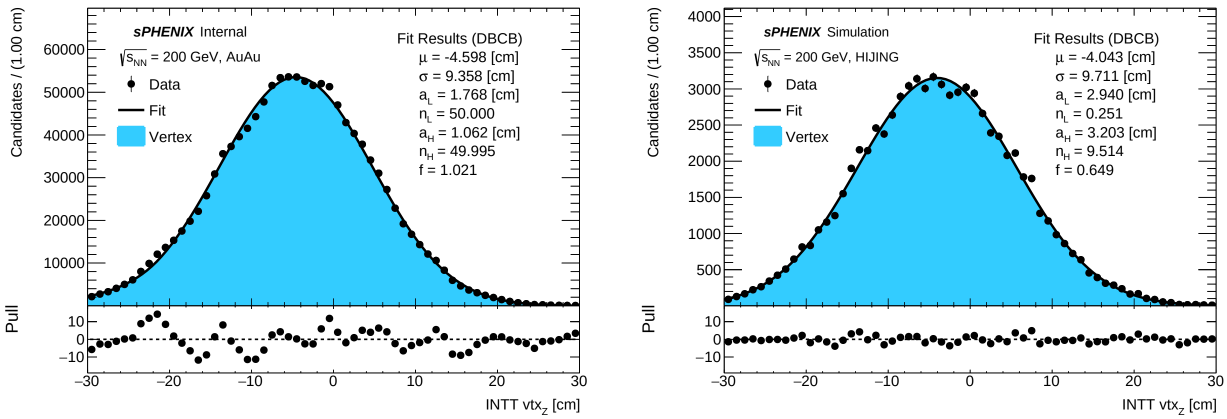

Figure 40: Double-side Crystal Ball fit to the reconstructed vertex in data (left) and simulation (right).

The INTT tracklet vertex Z reconstruction is compared to the MBD vertex Z calculation, as shown in Figure 41, using events from the 0–70% centrality intervals. The strong correlation indicates an agreement between the two independent measurements[2].

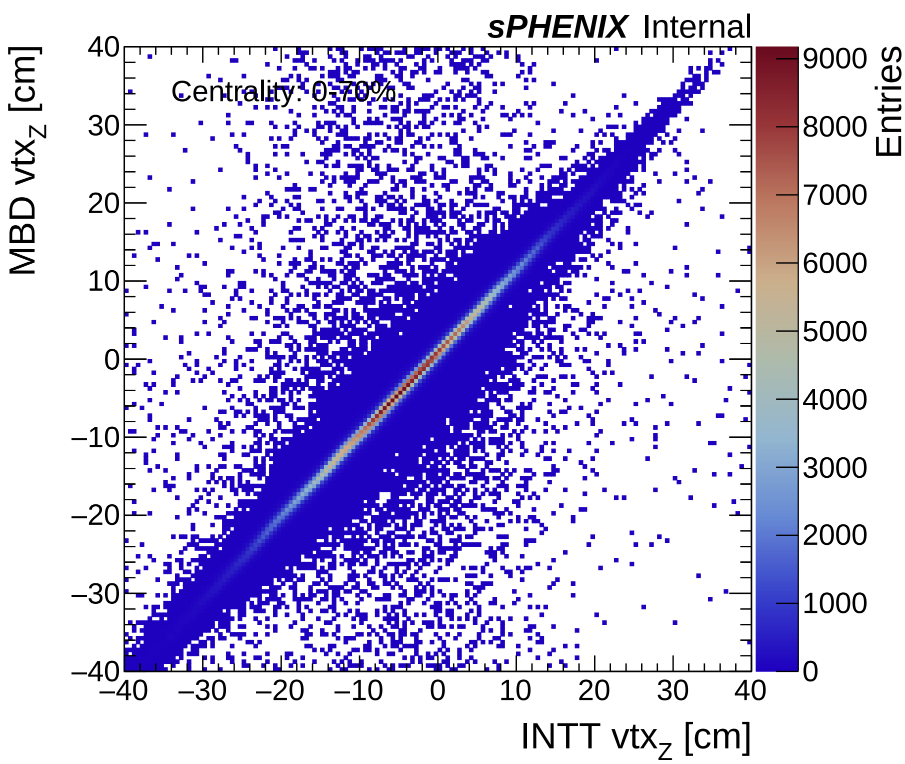

Figure 41: A comparison between the INTT tracklet vertex Z reconstruction and the MBD vertex determination.

[2]The MBD determines the relative vertex Z by calculating the time difference of the Cherenkov light detected by its calorimeters at both ends. A correction is then applied to obtain the absolute vertex Z.

The second approach, detailed in a separated internal note [41] and utilized in the PHOBOS-style analysis, constructs vertex candidates as trapezoidal shapes by assuming a uniform distribution of particle hit positions along the Z-axis of a strip. On the top of this method, the INTT vertex Z Quality Assurance (QA) is performed as described below.

In one event, after stacking up the trapezoidal shapes formed by all the valid cluster pairs, the distribution is fitted with 7 Gaussian functions with different fit ranges for each, as an example of one data event shown in Figure 42. And the vertex Z is determined by the average of the fit Gaussian means.

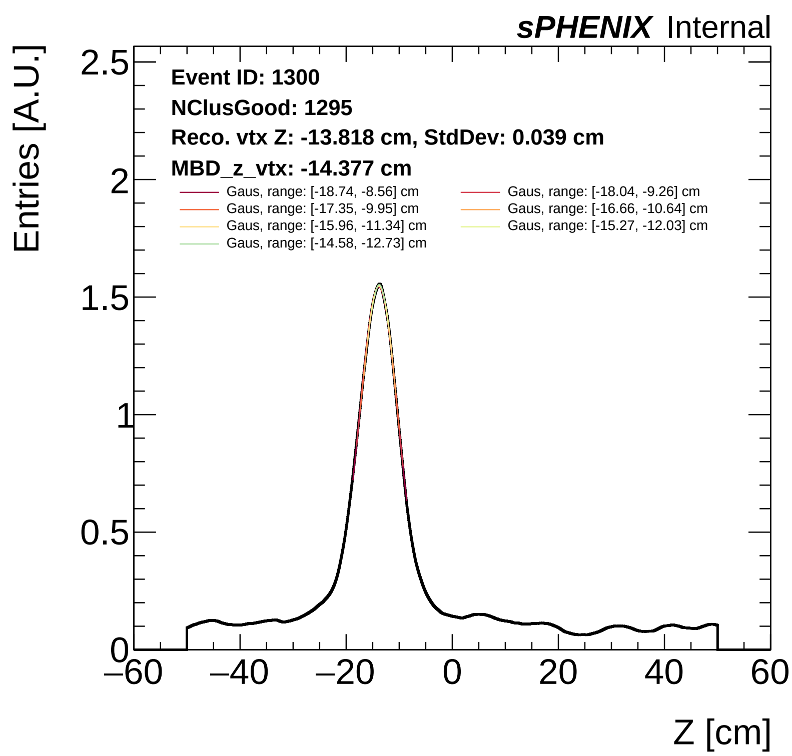

Figure 42: The probability distribution of the vertex Z in single event by stacking up the trapezoidal shapes formed by the valid cluster pairs.

Three properties are checked to assure the reliability of the reconstructed INTT vertex Z, the fit Gaussian width of the distribution, the Full Width Half Maximum (FWHM) of the distribution and the vertex Z difference between INTT and MBD, respectively, as shown in Figure 43. The table 4 summarizes the selected range of each checked property. The distributions of which after the QA selection are presented in Figure 44.

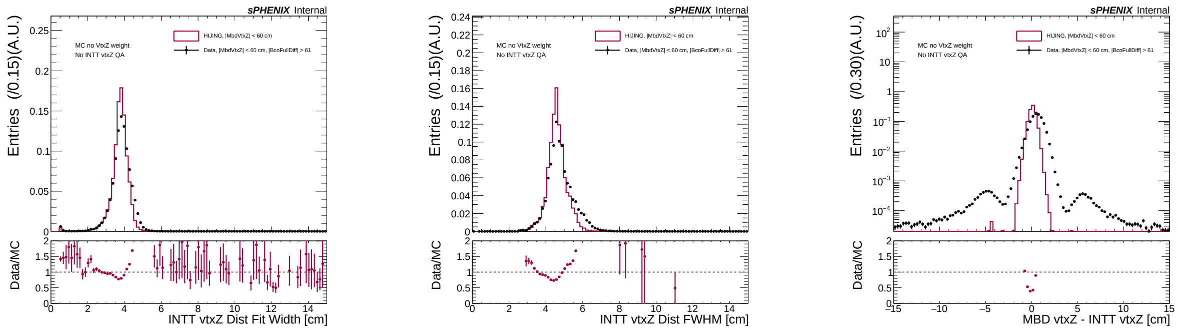

Figure 43: The properties of the reconstructed vertex Z before the QA check. (Left) The fit Gaussian width of the distribution. (Middle) The FWHM of the distribution. (Right) The vertex Z difference between the INTT and MBD.

Property	Cut Minimal [cm]	Cut Maximal [cm]
Fit Gaussian Width	1.5	5.5
FWHM	2	8
VtxZ Difference	-3	4

Table 4: The selections used in the INTT vtxZ QA.

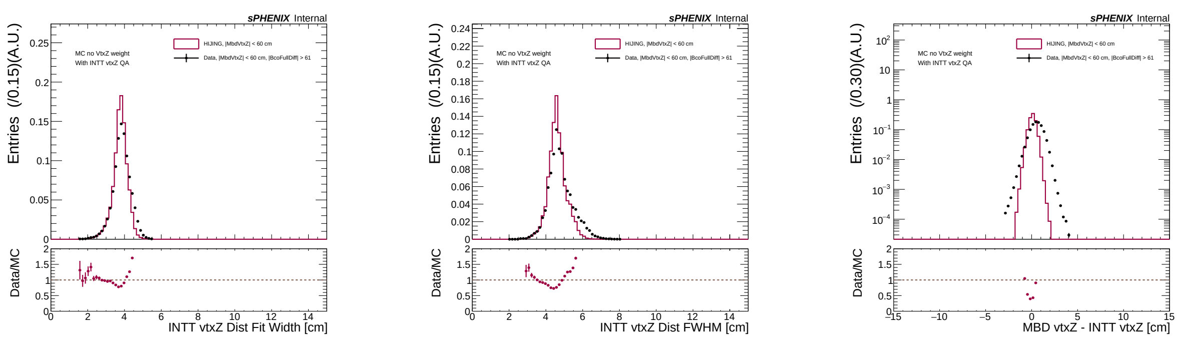

Figure 44: The properties of the reconstructed vertex Z after the QA check. (Left) The fit Gaussian width of the distribution. (Middle) The FWHM of the distribution. (Right) The vertex Z difference between the INTT and MBD.

One way to evaluate the performance of the selections is by checking the distribution of standard deviation of the reconstructed INTT vertex Z, as shown in Figure 45. The standard deviation of the vertex Z of single event is given by the standard deviation of the means of the seven fit Gaussian functions. The long tail in the distribution are minimized after the selection. And distributions of data and MC agree within the uncertainties. The performance of vertex Z reconstruction by this method is presented in Appendix E.

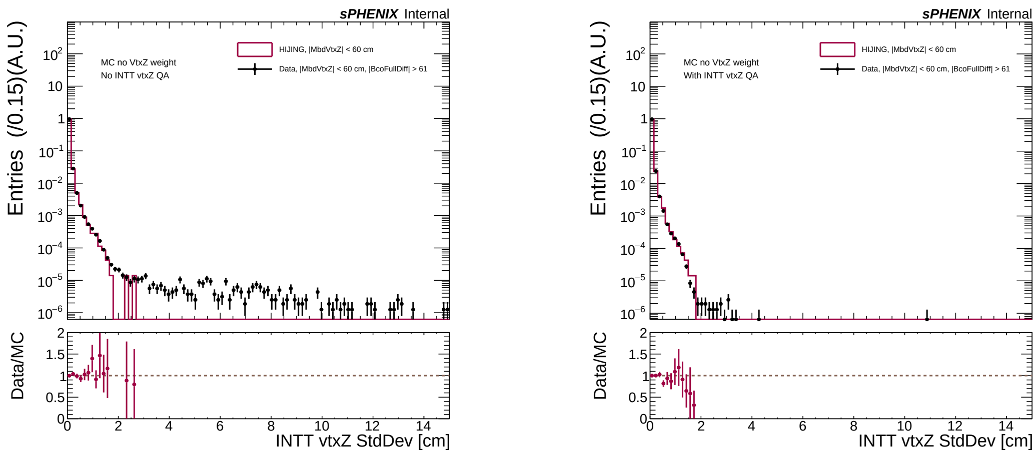

Figure 45: The distribution of the standard deviation of the reconstructed INTT vertex Z before the QA selection (Left) and after the QA selection (Right).

5.5 Tracklet reconstruction

Two approaches are developed for the tracklet reconstruction.

5.5.1 PHOBOS approach

In this approach, one step prior to the tracklet reconstruction, the INTT column uniformity is performed as the second confirmation after the bad channel masking in the level of the clusters with the simulation sample as the reference. The procedures are described as follows:

1. INTT, the two-layer barrel strip tracker, can be considered as 26 chip rings, as illustrated in Figure 46. There are 56 columns in one chip ring.

2. In data and simulation, and in one chip ring, the number of clusters of each column corrected for strip length and its ϕ acceptance, is accumulated, and normalized by the column with highest count, as shown in Figure 47.

3. The corrected multiplicity of each column in data is divided by that of in simulation afterwards, as shown in the right plot of Figure 47. Most of the columns are with the ratios around 1 while a few of columns is with the ratio away from 1, which indicates the disagreement in the multiplicity uniformity between data and simulation. Note that the normalization is performed in each chip ring, and the ratio is calculated column by column. Therefore, this method is generator model and vertex Z distribution independent. The only assumption made is the uniformity of the particle emission along the azimuthal angle.

4. The steps 2 and 3 are repeated for all the chip rings, and the result is shown in Figure 48. The distribution peaked at one indicating a good column uniformity.

5. The columns with the ratios outside the range of 0.8 to 1.2 are discarded in both data and simulation. The map of the columns used in the following analysis is shown in Figure 49.

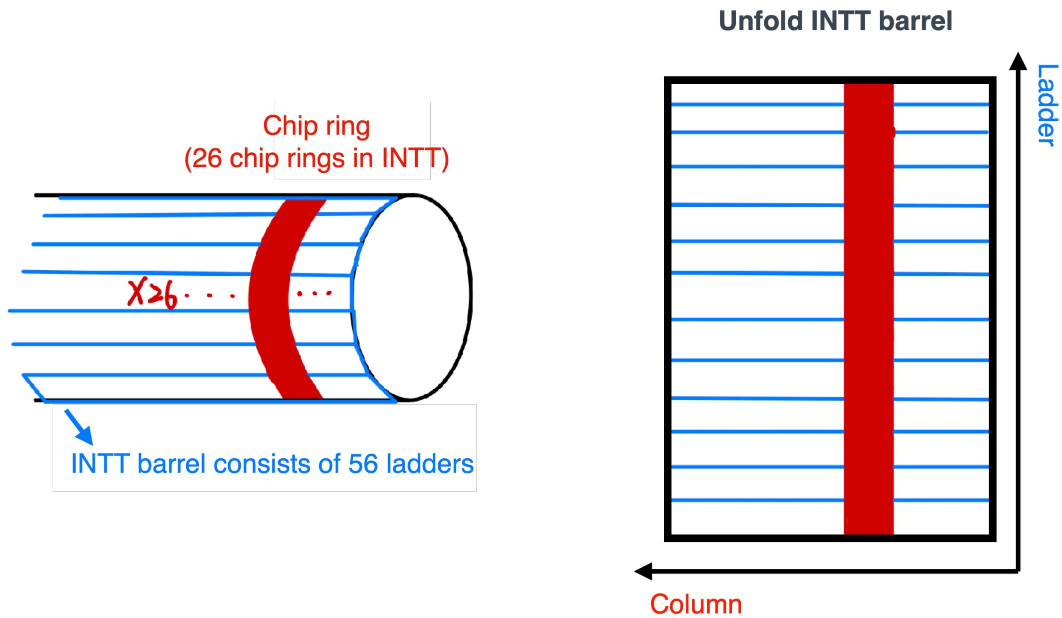

Figure 46: Cartoon showing the structure of INTT column ring.

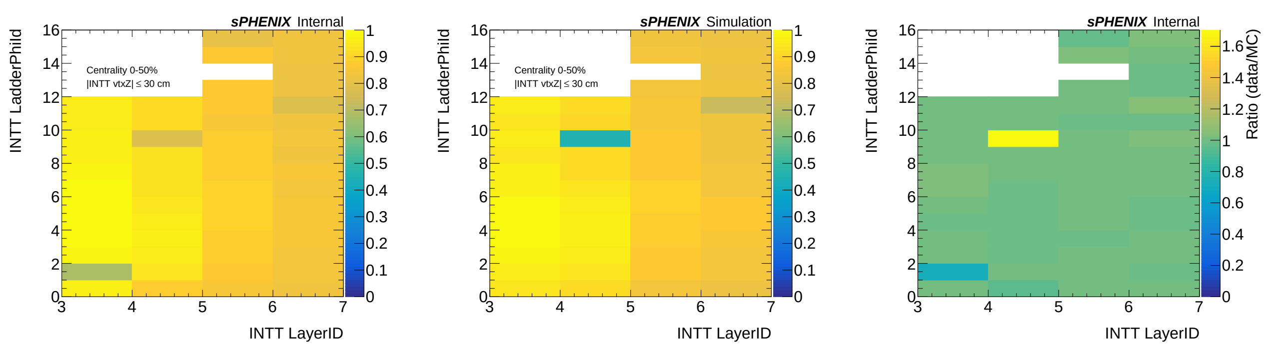

Figure 47: The corrected and normalized multiplicity of all 56 columns in one INTT chip ring in data (left) and simulation (middle). Right: The ratio between data and simulation.

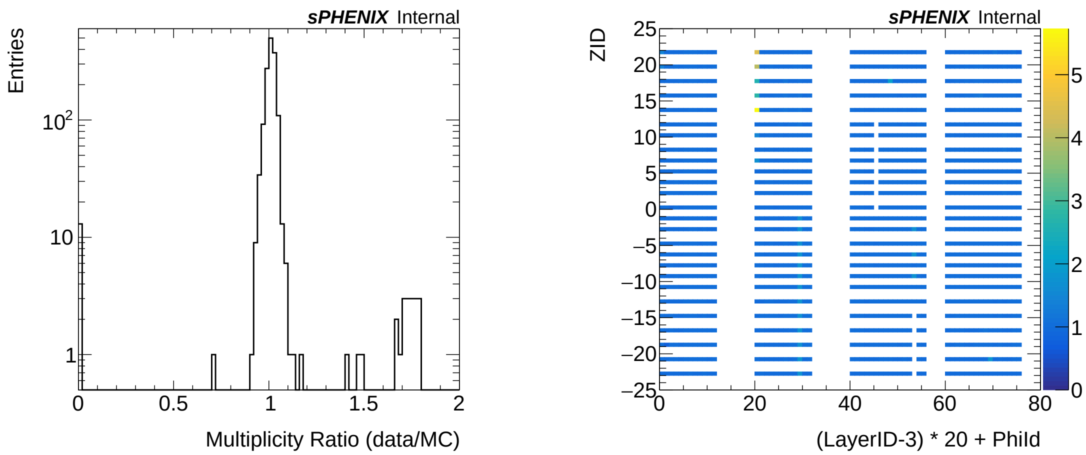

Figure 48: The ratio of the corrected multiplicity between data and simulation of each of all the 1456 INTT columns presented in 1D (left) and 2D (right).

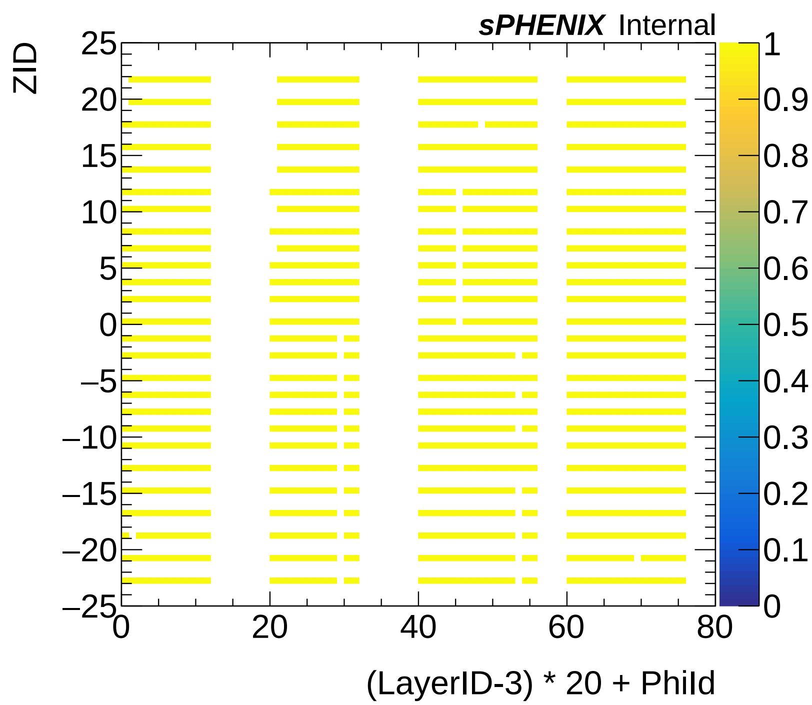

Figure 49: The column map used in the following analysis.

The main concept of tracklet reconstruction of PHOBOS approach is to allow single cluster to be involved in multiple pairs introduced as follows:

1. The cluster η and ϕ are corrected based on the reconstructed average vertex X and Y, v_x and v_y, and per event vertex Z, v_z.

2. In an event, loop over all the cluster pairs formed by one cluster in inner barrel and one cluster in outer barrel.

3. The extrapolated possible vertex Z range of a cluster pair not able to link to the reconstructed v_z is discarded, as demonstrated in Figure 50. Such requirement is equivalent to a cut $|\Delta\eta| \leq 0.25$, as shown in the right plot of Figure 50. The η angle of the cluster pair satisfied the requirement is given by the average of the two cluster η angles.

4. Fill the $\Delta\phi$ of the pair into the corresponding one-dimensional $\Delta\phi$ histogram according to its η angle, and centrality and reconstructed v_z of the event.

5. Repeat the steps 3 and 4 for all the combinations and step 2 for all the events.

6. After the loop, stack over the $\Delta\phi$ distributions for each tracklet η bin according to the selected region, as the example shown in left plot of Figure51. The statistic can therefore be increased.

7. The $\Delta\phi$ distribution is composed of two components, the entries of the signal and the contribution of combinatorial background due to incorrect pair formations which results in a bulk underneath the signal. The combinatorial background is estimated by rotating the inner-barrel clusters by π in ϕ angle, as shown in the right plot of Figure 51. The signal is extracted by the subtraction of the two distributions, as shown in Figure 52.

8. The number of tracklets of a given η region is determined by the entries of the subtracted $\Delta\phi$ distribution within the region of 0.021 radians for baseline.

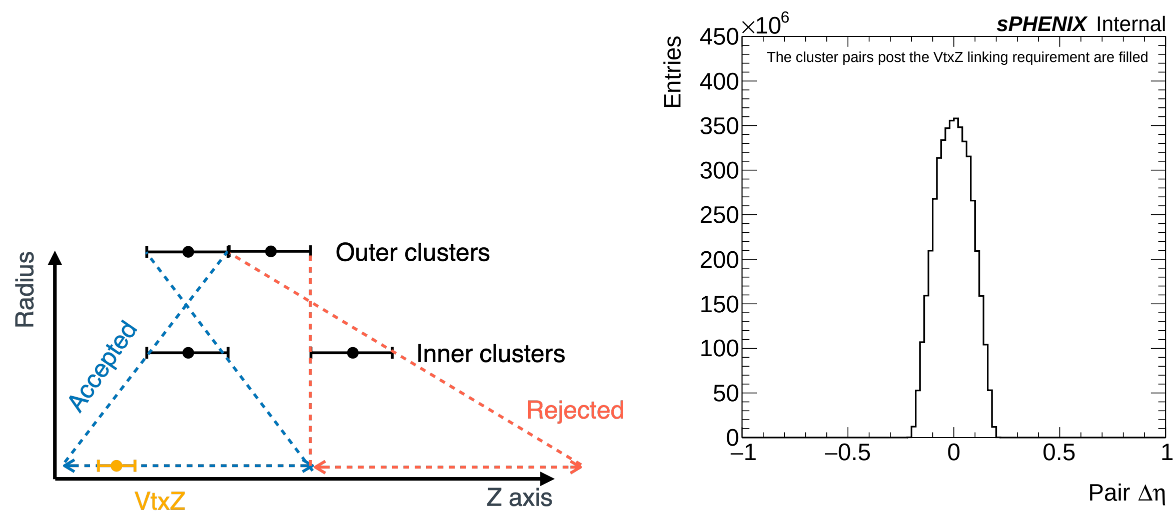

Figure 50: Left: Demonstrating the requirement of cluster pair linking to the reconstructed vertex Z. Right: The $\Delta\eta$ distribution of the cluster pairs satisfied the vertex Z linking requirement.

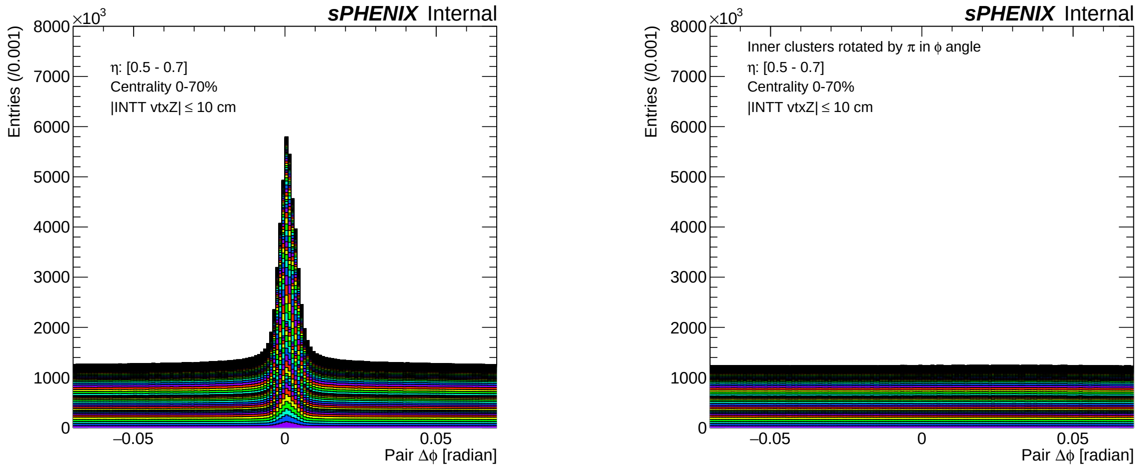

Figure 51: Left: The stacked $\Delta\phi$ distribution in the ranges of $|v_z| \leq 10$ cm, tracklet η 0.5 to 0.7, and centrality 0 to 70 %. Right: The same stacked distribution while having the inner clusters rotated by π in ϕ angle.

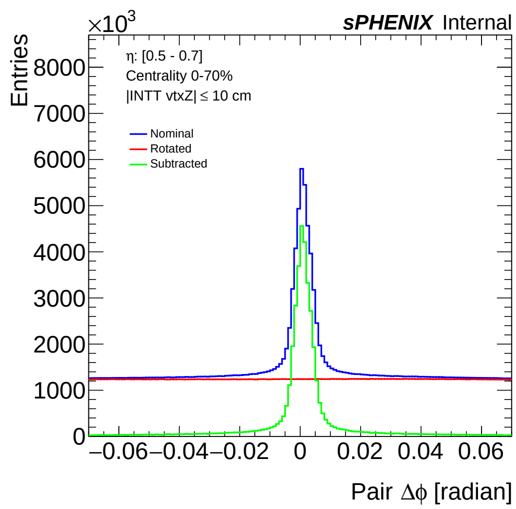

Figure 52: The $\Delta\phi$ distributions of a given region.

The distribution of average number of reconstructed tracklets per event is shown in Figure 53.

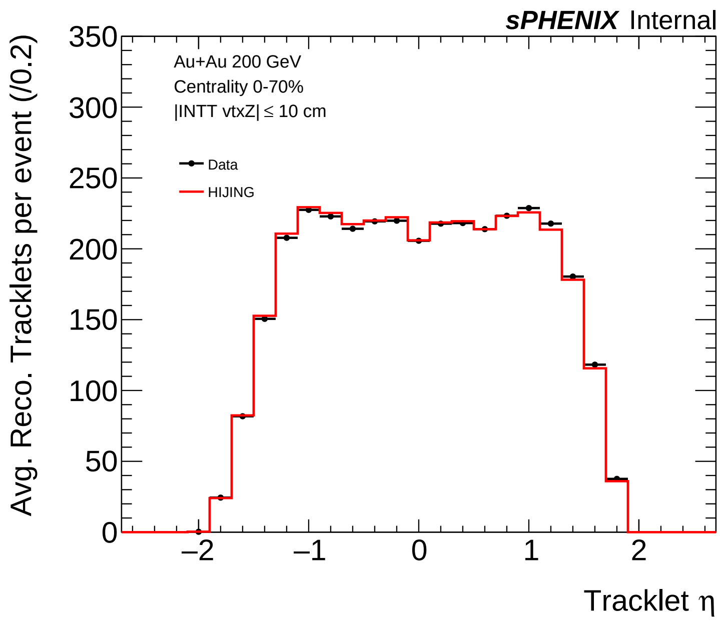

Figure 53: The average number of reconstructed tracklets per event as a function of η.

5.5.2 CMS approach

The reconstruction of tracklets is performed in a 3-step process:

1. The cluster η and ϕ values are updated using the reconstructed event vertex
2. For each cluster in the inner layer, loop through the clusters in the outer layer. Combinations with ΔR (as defined in Eq. 4) less than 0.5 are kept and sorted by ΔR
3. In cases of multiple matches for a cluster, the combination with the smallest ΔR is selected and forms the collection of reconstructed tracklets

Figure 54 and 55 show the number of reconstructed tracklets, tracklet ϕ, tracklet η, tracklet $\Delta\phi$, tracklet $\Delta\eta$, and tracklet ΔR.

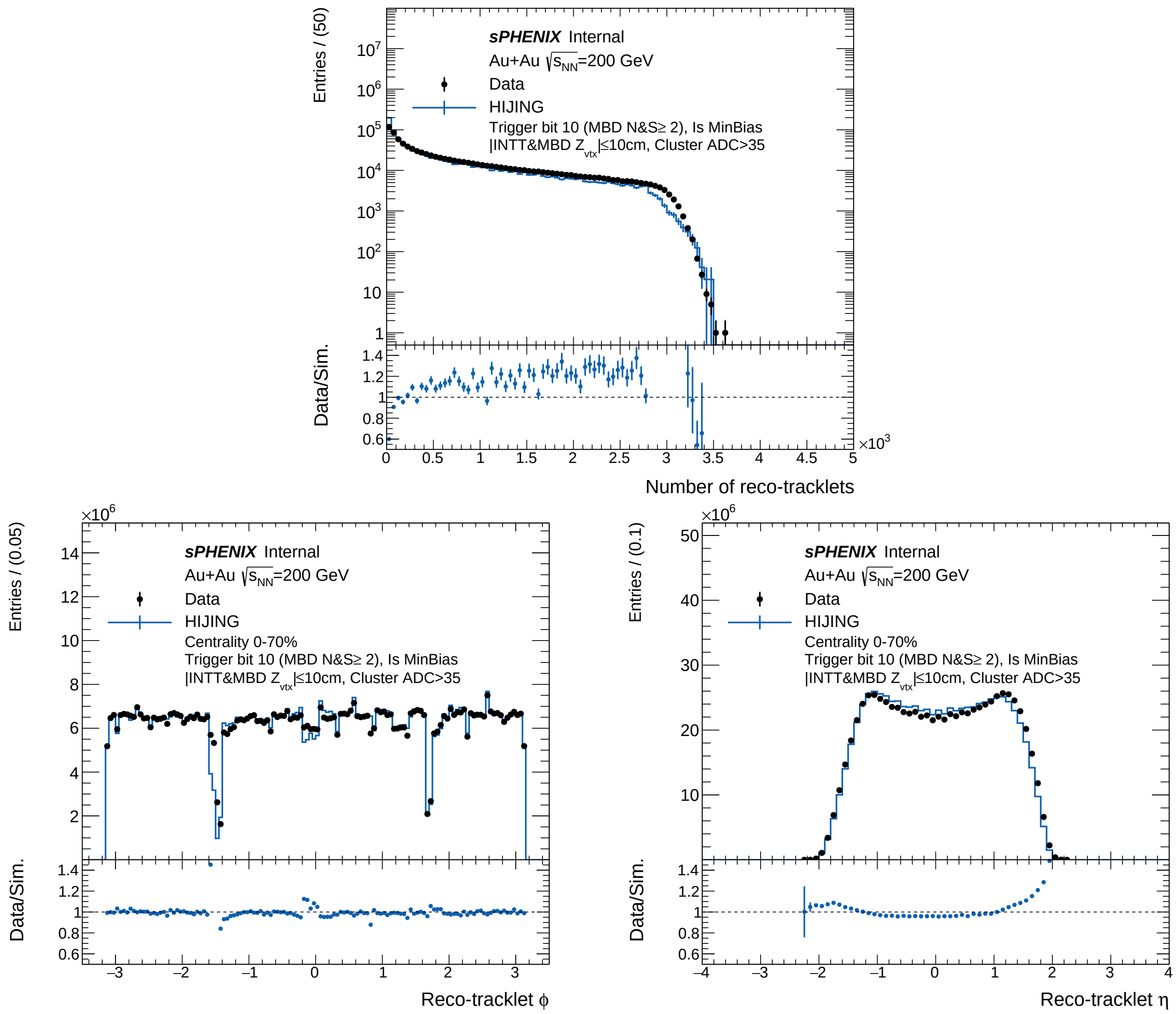

Figure 54: The number of reconstructed tracklets (top), tracklet ϕ (bottom left), tracklet η (bottom right).

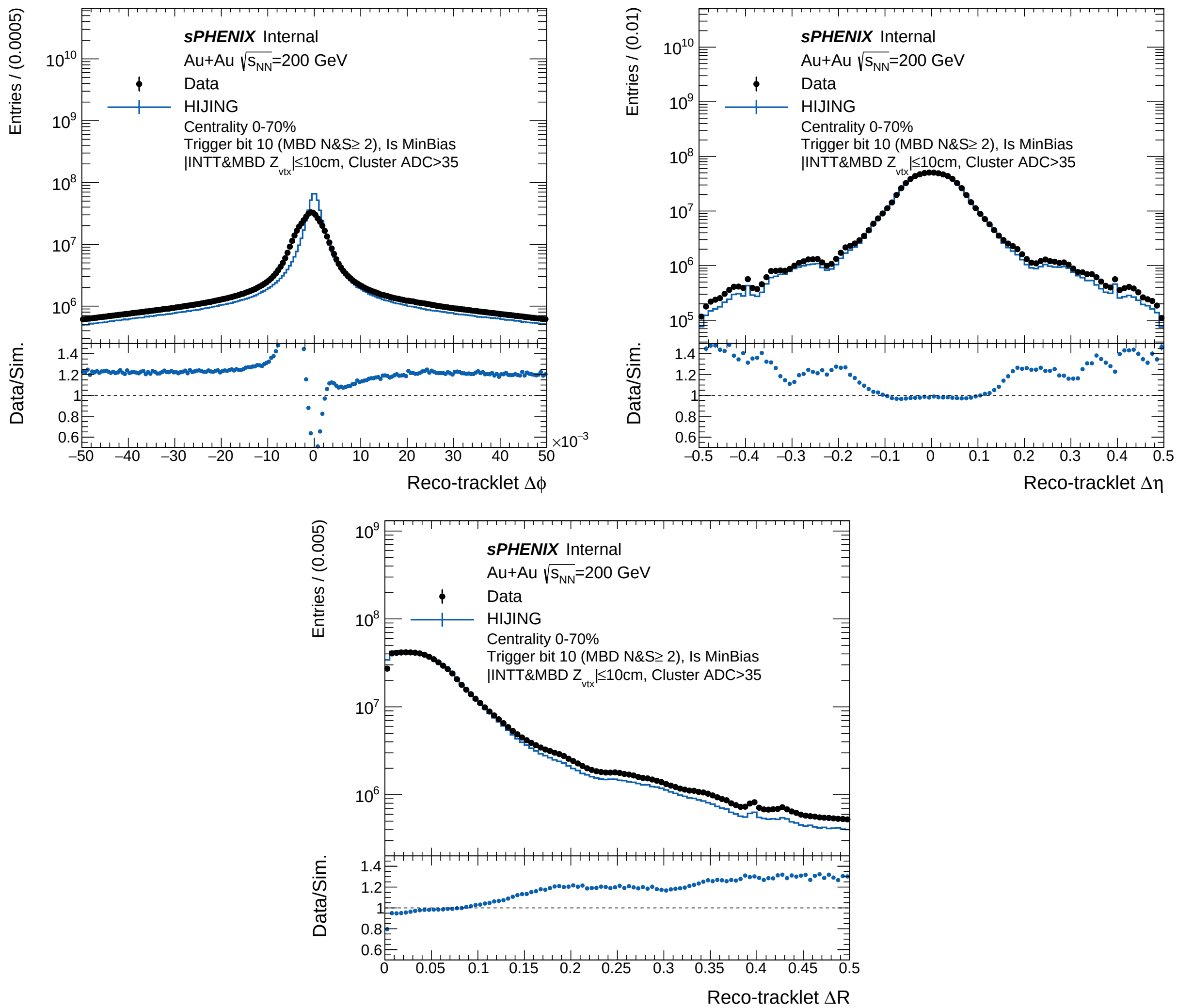

Figure 55: The tracklet $\Delta\phi$ (top left), tracklet $\Delta\eta$ (top right), and tracklet ΔR (bottom).

Figure 56 compares the ϕ-sizes of constituent clusters in tracklets, where the number of tracklets in which both constituent clusters have a ϕ-size of 43 or 46, as well as those where either constituent cluster has a ϕ-size of 43 or 46 are listed in Table 5. Despite the unexpectedly large number of clusters with ϕ-sizes of 43 and 46, the results indicate that only a negligible fraction of tracklets are formed by these clusters.

Category	Count	Fraction
Total number of tracklets	$8.018{\times}10^{8}$	–
Number of tracklets in which both constituent clusters have a ϕ-size of 43 or 46	12	$1.522{\times}10^{-5}$ %
Number of tracklets in which either constituent cluster has a ϕ-size of 43 or 46	$3.577{\times}10^{4}$	$4.462{\times}10^{-3}$ %

Table 5: The number of tracklets in which both constituent clusters have a ϕ-size of 43 or 46, as well as those where either constituent cluster has a ϕ-size of 43 or 46.

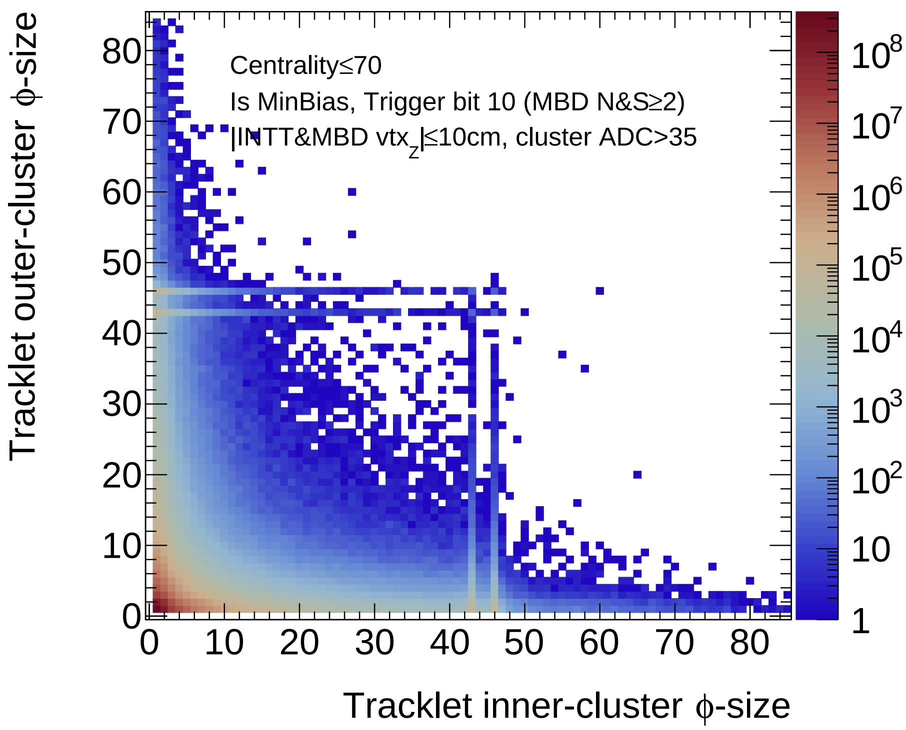

Figure 56: The ϕ-size of constituent clusters on tracklets.

6 Correction factors

Correction factors are applied to correct the reconstructed tracklet spectra to the "prompt" charged hadron definition, properly accounting for acceptance and efficiency. The correction factors derived from the HIJING generator are used as the baseline for the final results.

The PHOBOS and CMS analyses differ in the tracklet reconstruction and counting. Consequently, as in the previous section, the correction factors are discussed separately.

6.1 PHOBOS approach

In the PHOBOS approach the items considered are summarized below:

1. **Column uniformity corrections**: This performs as a column multiplicity uniformity check after the bad channel masking in the level of cluster as described in 5.5.1.

2. **Acceptance and efficiency corrections**: This accounts for the discrepancies between the number of charged hadrons emitted from the collisions and the number of the reconstructed tracklets, as described in Section 6.1.1.

3. **Misalignment in data**: An alternative method has been developed to account for misalignment in the INTT ladders by introducing random displacements, as detailed in Section 7.1.1. The impact of misalignment in the data is quantified as a source of systematic uncertainty in the PHOBOS approach, and no correction is applied.

6.1.1 Acceptance and efficiency correction

This correction is to account for the discrepancies between the number of charged hadrons emitted from the collisions and the number of reconstructed tracklets due to the acceptance and geometry limit of INTT. In the PHOBOS approach, one set of the average numbers of reconstructed tracklets per event in different η bins are derived with the full vertex Z range used in the analysis, as shown in Figure 57. Therefore, the corrections are derived by taking the ratio between the number of reconstructed tracklets per event and number of charged hadrons per event in the generator level with the same range of the vertex Z in a given centrality bin. Figure 58 shows the corrections in the centrality interval 0-70% as an example. Such ratios take the acceptance and the efficiency effects into account together. In the mid-rapidity region, the corrections are around 90 % indicating the good reconstruction efficiency. The steep correction reduction in both sides of the distribution are mostly due to the acceptance limit of INTT. The relatively lower correction at $\eta = 0$ is due to the geometry limit of INTT. Figure 59 shows the valid cluster pair multiplicity as a function of pair η and v_z. The tilted pointed-ellipse shapes at pair $\eta = 0$ across the vertex Z do not refer to the dead acceptance regions. The particles are captured. However, the resolution of tracklet η reconstruction is rather poor, which leads to almost no tracklet with $\eta \sim 0$ can be reconstructed. The η bin with correction < 0.5 is discarded in the following analysis due to its low reconstruction efficiency.

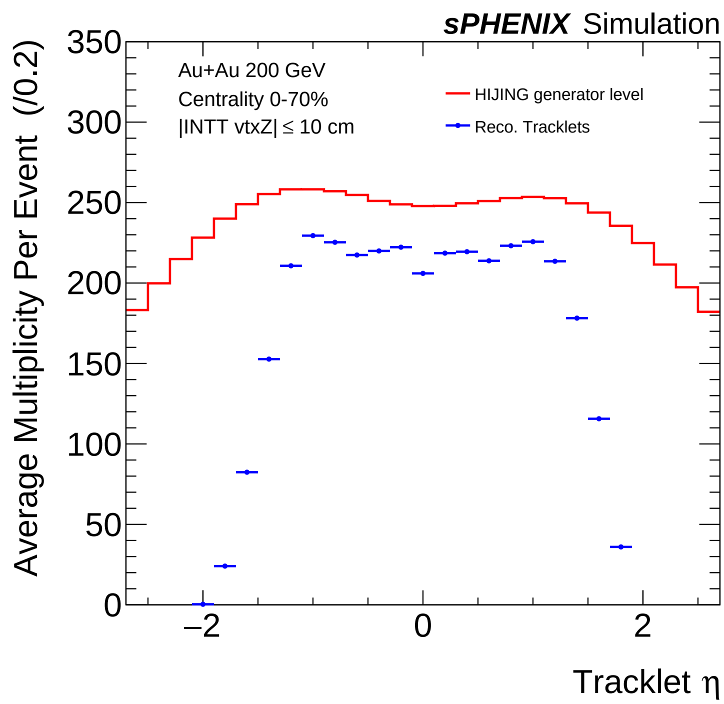

Figure 57: The numbers of reconstructed tracklets and truth hadrons per event for the centrality interval 0-70% as a function of η.

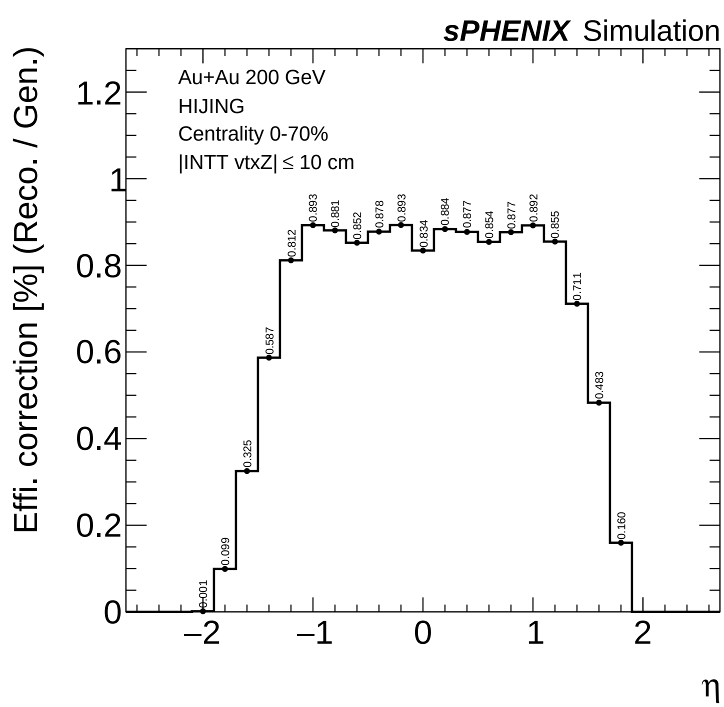

Figure 58: The acceptance and efficiency corrections for the centrality interval 0-70% as a function of η.

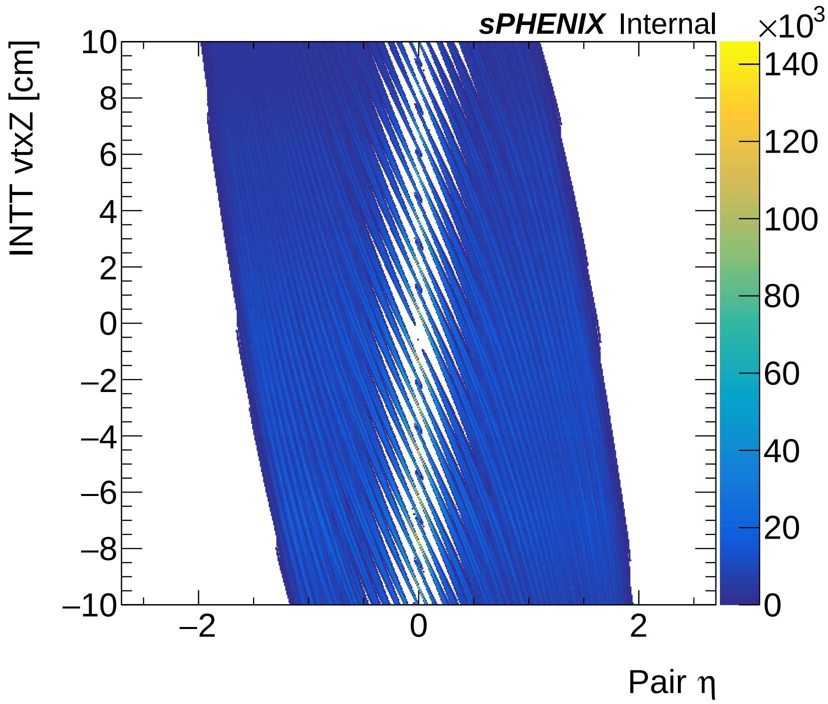

Figure 59: The finely-binned histogram filled by valid cluster pairs.

6.2 CMS approach

6.2.1 Geometry difference between data and simulation

This correction accounts for the geometry difference between data and simulation. The GEANT4 geometry is modified based on survey measurements, and the reconstruction geometry is built to match the implemented GEANT4 geometry. However, neither geometry perfectly replicates the actual INTT geometry in the physical world. As a result, in simulations, hits are generated and reconstructed using the same geometry, whereas in data, hits are recorded by the detector at physical locations that differ from those reconstructed in the software. This correction factor compensates for the effects of this discrepancy.

The correction is derived in the following steps:

1. Each event is assigned a random vertex Z position, uniformly sampled from -10 to 10 cm. Clusters η and ϕ values are updated accordingly, and "fake" tracklets that do not pass through gaps are reconstructed using the assigned vertex.

2. "Fake" tracklets are filled into a finely binned histogram in the (η, vtx_z) space. Bins containing at least one fake tracklet are normalized to 1, while empty bins are set to 0.

3. The bins of the histogram are weighted by the vertex distribution in data, and the histograms are re-binned into coarser bins. The final correction factor is calculated as the ratio of the simulation histogram to the data histogram.

Figure 60 shows the correction factor for geometric differences as a function of tracklet η and the event vertex vtx_z. The correction factor remains close to 1 throughout most of the acceptance range, with noticeable deviations near the edges. Regions where the correction factor falls below 0.75 or exceeds 1.25 are excluded from the analysis, as marked by the red lines. This correction factor does not depend on centrality, as it is purely driven by the detector geometry.

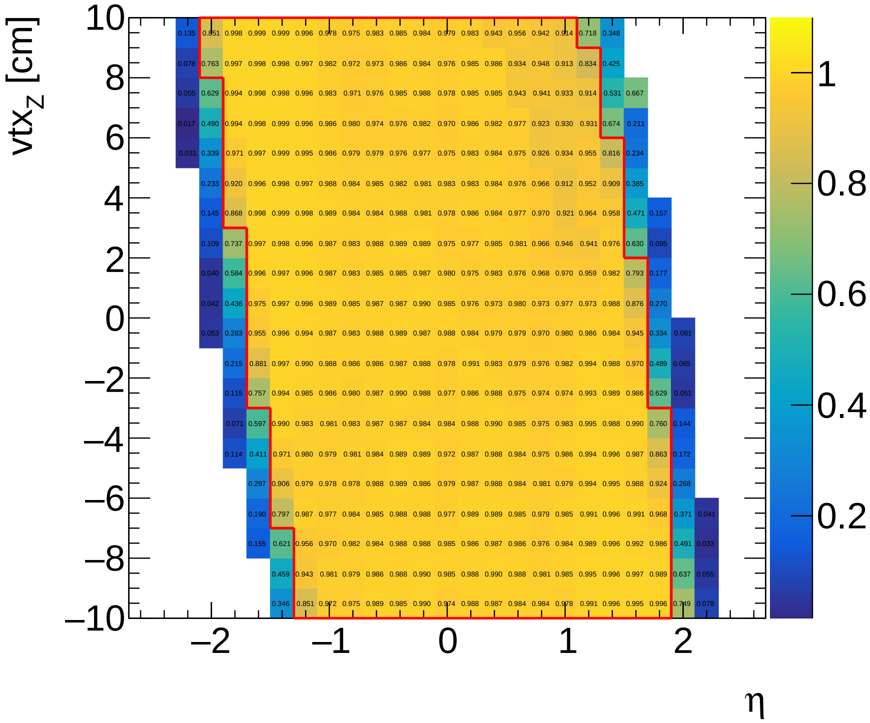

Figure 60: The geometric correction as a function of tracklet η and v_z.

6.2.2 Acceptance and efficiency correction

The reconstructed tracklets are corrected for inefficiencies in the tracklet reconstruction. This correction, referred to as the α factor, is defined as the ratio of the total number of primary charged hadrons in the simulation to the number of uncorrected reconstructed tracklets. To maintain good control over the correction factors, the α factor in each bin is required to satisfy the following conditions :

1. $0 \leq \alpha \leq 3.6$

2. $(\frac{\alpha}{\sigma_\alpha} > 5 \ \&\& \ \alpha < 3) \ || \ (\alpha < 2)$

where σ_α is the statistical error of the α. Regions in the (η, vtx_z) phase space where the α factor does not satisfy these criteria are excluded from the analysis. The acceptance correction accounts for the fact that the detector does not have infinite phase-space coverage. For instance, the length of the INTT ladders provides full acceptance only within $|\eta| \leq 1.2$ for an event vertex at $|\mathrm{vtx}_z| \leq 10$ cm, while clusters with larger $|\eta|$ cannot be recorded when the event vertex is shifted. To derive this correction, a two-dimensional histogram of (η, vtx_z) is first filled with the number of tracklets per vtx_z bin. A second two-dimensional histogram of (η, vtx_z) is then filled with the number of tracklets reconstructed in regions with a valid α factor. The correction factor is calculated by taking the ratio of the two histograms and projecting it into the η dimension.

Figure 61 shows the α factor as a function of η and vtx_z and the acceptance correction for events in the centrality interval 0–70%. Corrections in different centrality intervals can be found in Appendix G.

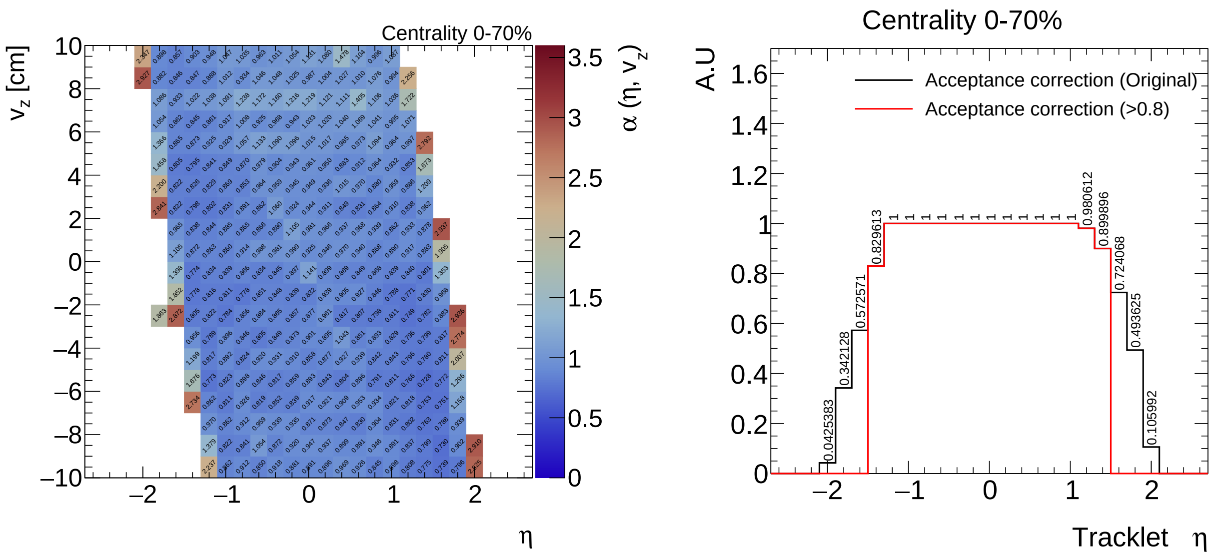

Figure 61: The α factor (left) and acceptance correction (right) for centrality 0–70%.

7 Systematic uncertainties

Systematic uncertainties considered in the two analyses are discussed separately below.

7.1 PHOBOS approach

The following sources of systematic uncertainty are considered:

- **Tracklet counting region.** The tracklet counting region in the subtracted $\Delta\phi$ distribution is varied to $|\Delta\phi| \leq 0.018$ and $|\Delta\phi| \leq 0.024$.
- **Cluster ADC cut.** Same as described in Section 7.2.
- **Cluster ϕ-size cut.** Same as described in Section 7.2.
- **Run segmentation.** The full set of data DST available is used as the baseline $dN_{ch}/d\eta$, while the maximum variation observed in the the segments of first and second 1.5 million events is quoted as a systematic uncertainty.

- **Geometry misalignment.** This accounts for the remaining misalignment in data. The method is described in Section 7.1.1.
- **(To be included) Event generator.** Same as described in Section 7.2.
- **(To be included) Strangeness decay.** Same as described in Section 7.2.

7.1.1 The uncertainty due to the geometry misalignment

Figure 62 shows the $\Delta\phi$ of cluster pairs as a function of the inner cluster ϕ angle for one of the subsamples in data, where the cluster ϕ angles have been updated based on the assigned beam spot. While a generally flat correlation is observed, ladder-by-ladder fluctuations persist in data. In contrast, no such fluctuations are seen in the simulation, as shown in Figure 32. This is expected since the INTT geometry in GEANT4 and the offline geometry are perfectly aligned in simulation and suggests that the observed fluctuations in data are due to residual misalignment.

To quantify the impact of these residual misalignments, a strategy is implemented that introduces random displacements to cluster positions, effectively simulating the effects of misalignment in the data. The procedures are outlined as follows:

1. Introduce displacements in three dimensions (X, Y, Z) to each of 56 ladders. The clusters in a given ladder are therefore shifted from nominal positions systematically.
2. Process all simulation events through the full PHOBOS-approach analysis, including event vertex and tracklet reconstructions.
3. Repeat the procedures 500 times

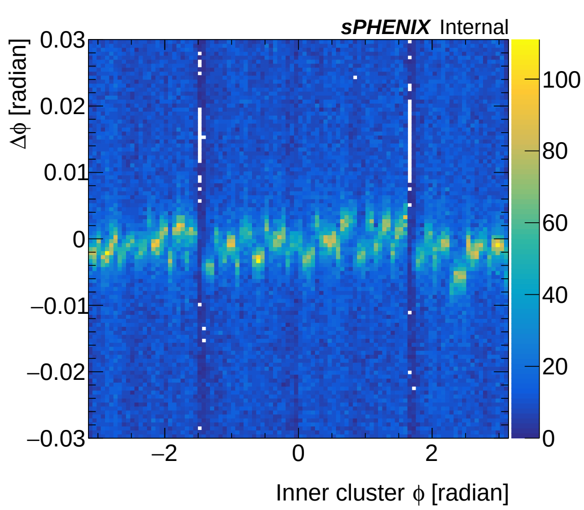

Figure 62: The $\Delta\phi$ of cluster pairs as a function of inner cluster ϕ angle.

Figure 63 shows the distributions of the amount of the introduced offsets to each ladder in all the trials in three dimensions. And the variation of the reconstructed beam spot is shown in Figure 64. The standard deviations of the variation are around 230μm in both axes. Figure 65, 66 and 67 show the variations of the reconstructed vertex Z, $\Delta\phi$ of valid cluster pairs, and the average number of reconstructed tracklets, respectively. The $\Delta\phi$ distribution is wider when the offsets are introduced to the offline geometry, which is similar to what observed in data, as shown in Figure 55. In each bin, the maximal relative deviation times the acceptance and efficiency correction is quoted as the systematic uncertainty.

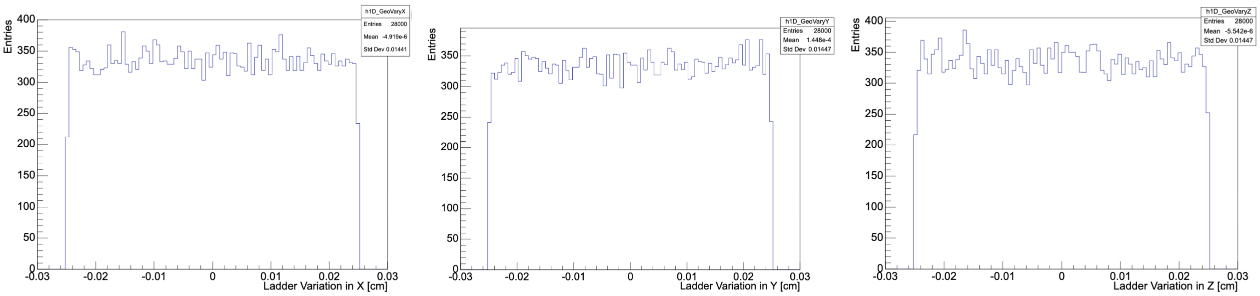

Figure 63: The distributions of introduced offsets to each ladder of all the trials in simulation.

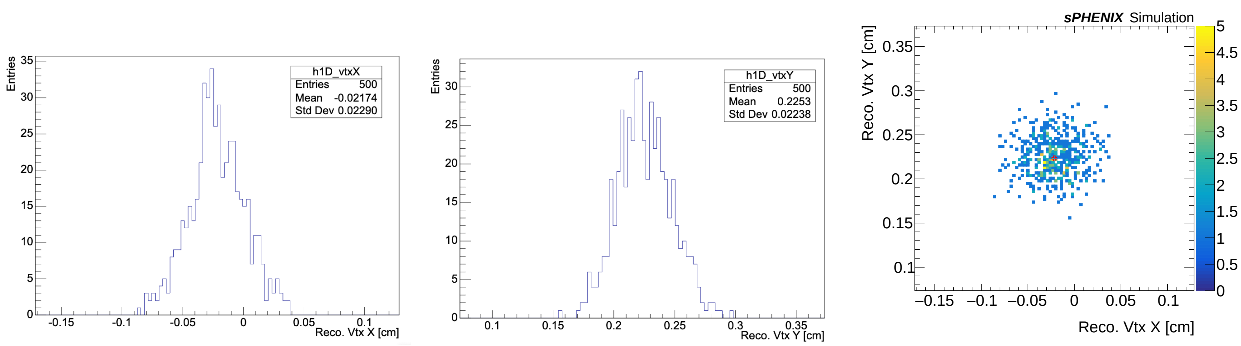

Figure 64: The variation of the reconstructed vertex X (Left) and Y (Middle). Right: The variation of which in 2D. The red cross mark corresponds to the reconstructed beam spot without the offset introduction.

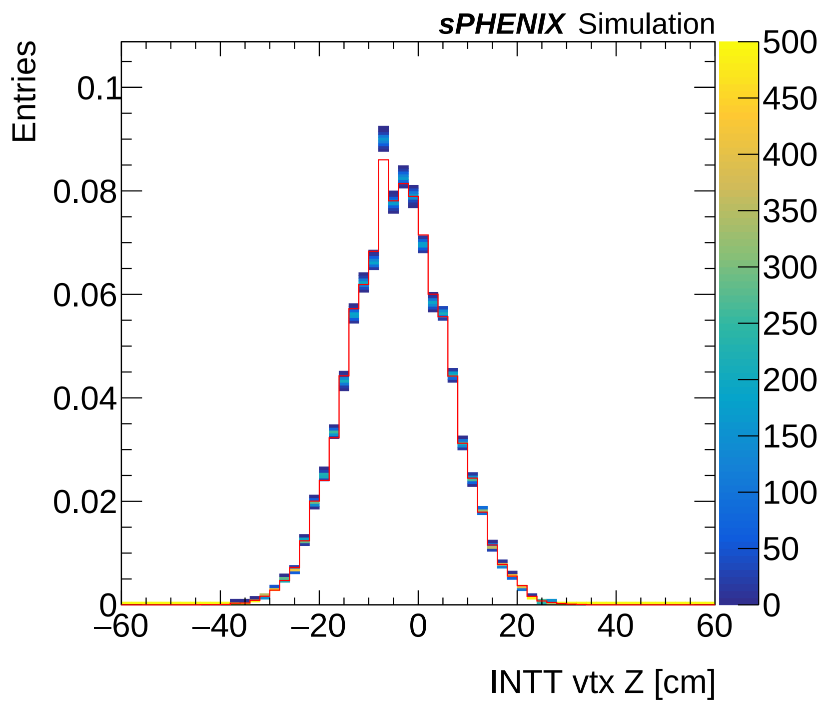

Figure 65: The variation of the reconstructed vertex Z. The distribution in red is without the offset introduction.

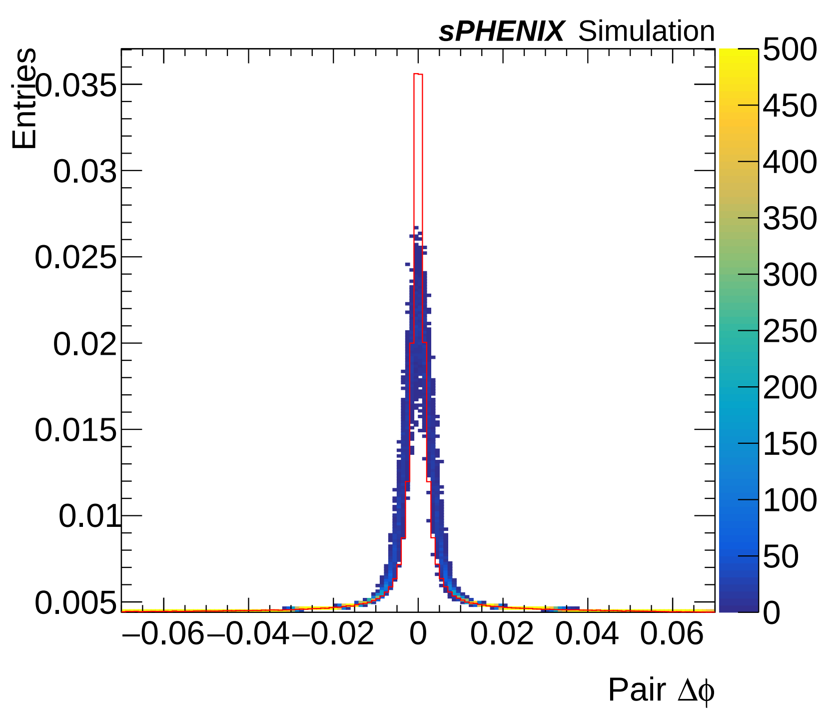

Figure 66: The variation of the $\Delta\phi$ of the valid cluster pairs. The distribution in red is without the offset introduction.

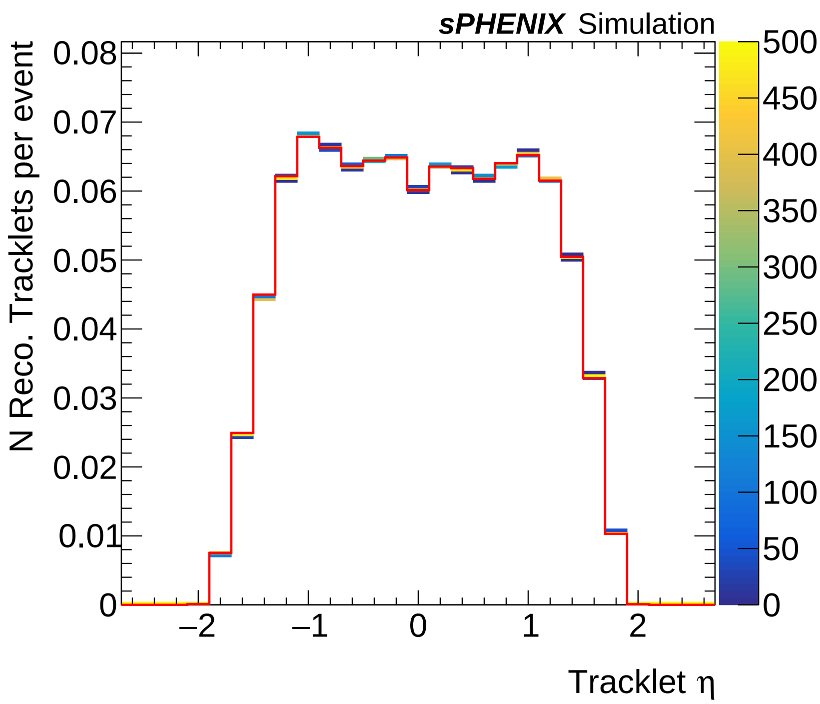

Figure 67: The variation of normalized number of reconstructed tracklet. The distribution in red is without the offset introduction.

7.1.2 The summary of the systematic uncertainties

The relative variations of the considered systematic uncertainties to the nominal $dN_{ch}/d\eta$ are shown in Figure 68 for the centrality interval 0–70%. The total uncertainty, calculated as the quadrature sum of all individual contributions, is also presented.

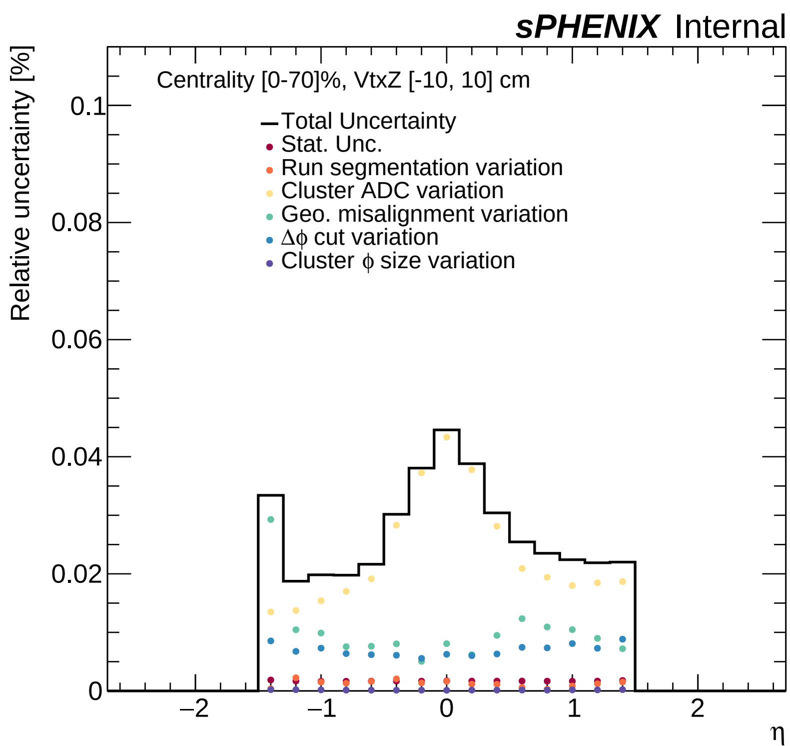

Figure 68: Systematic uncertainties for the centrality interval 0–70%.

7.2 CMS approach

The following sources of systematic uncertainty are considered:

- **Tracklet reconstruction selection**. The tracklet reconstruction selection is varied to $\Delta R < 0.4$ and $\Delta R < 0.6$. The maximum deviation in the final $dN_{ch}/d\eta$ result is taken as a systematic uncertainty.
- **Cluster ADC cut**. The baseline analysis applies a cluster ADC threshold of > 35. As a variation, this selection is disabled, and the impact on the final $dN_{ch}/d\eta$ result is quantified as a systematic uncertainty.
- **Cluster ϕ-Size cut**. In the baseline analysis, a cluster ϕ-size selection of < 40 is applied. To assess its effect, the selection is removed, and the analysis is repeated. The largest variation in the $dN_{ch}/d\eta$ distribution is taken as a systematic uncertainty.
- **Run segments**. The data DST is divided into four segments, with three containing 1 million events each and the fourth containing the remainder. The baseline $dN_{ch}/d\eta$ distribution is measured using the first segment, while the maximum variation observed in the other three segments is quoted as a systematic uncertainty.
- **(To be included) Event generator**. The baseline analysis and correction factors are derived using simulation samples generated with HIJING. Correction factors will

also be derived using samples from EPOS and AMPT, and the largest variation in the $dN_{ch}/d\eta$ distribution will be quoted as a systematic uncertainty.

- **(To be included) Strangeness decay**. Decays of strange particles can result in multiple clusters, leading to potential "double/multiple counting" in the $dN_{ch}/d\eta$ measurement. The effect is evaluated by varying the fraction of strange particles among primary particles in simulation and assessing the impact on $dN_{ch}/d\eta$.

The relative magnitudes of each systematic uncertainty, defined as the ratio of the variation to the nominal $dN_{ch}/d\eta$, are shown in Figure 69 for the centrality interval 0–70%. The total uncertainty, calculated as the quadrature sum of all individual contributions, is also presented. Systematic uncertainties for different centrality intervals are shown in Appendix I.

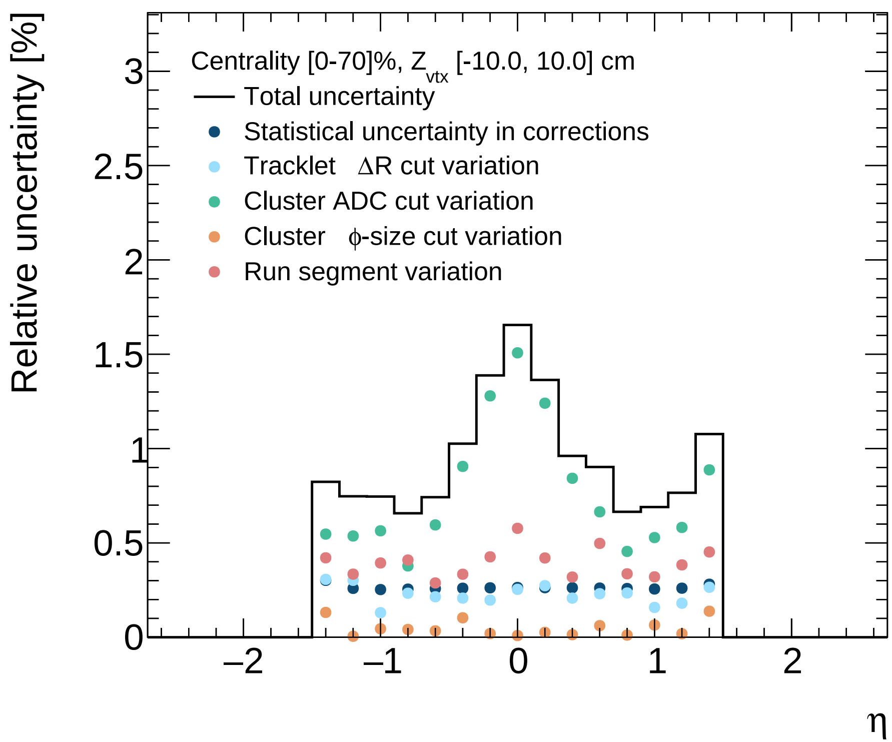

Figure 69: Systematic uncertainties for the centrality interval 0–70%.

8 Results

NOTE: Update when the centrality calibration in simulation is available

Figure 70 shows the $dN_{ch}/d\eta$ in data, HIJING generator, and HIJING simulation closure, and from the PHOBOS measurement [9] in each centrality interval.

The centrality dependence of the average $dN_{ch}/d\eta$ at midrapidity is shown in Figure 71 and is compared to previous measurements at RHIC. The $dN_{ch}/d\eta$ normalized by $\langle N_{part} \rangle$ is also shown as a function of $\langle N_{part} \rangle$ in Figure 71, where $\langle N_{part} \rangle$, listed in Table 6 are estimated from the Glauber model.

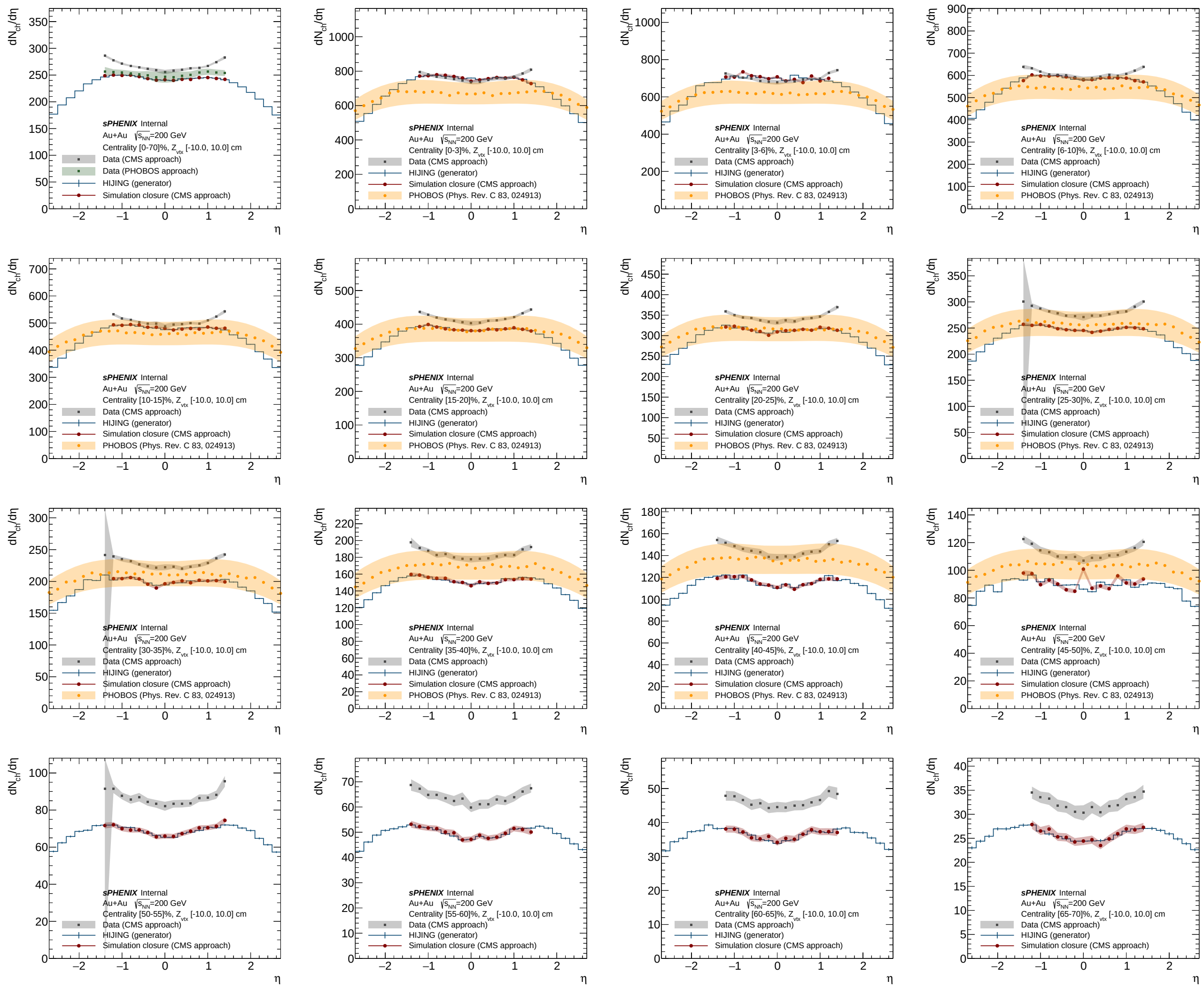

Figure 70: The $\mathrm{dN_{ch}}/\mathrm{d}\eta$ distributions in from HIJING generator, simulation closure, data, and the PHOBOS measurement in each centrality interval.

9 Conclusion

The charged-hadron pseudorapidity density, $\mathrm{dN_{ch}}/\mathrm{d}\eta$, is measured using data collected by the sPHENIX INTT detector in Au+Au collisions of $\sqrt{s_{NN}} = 200\,\mathrm{GeV}$.

Centrality interval [%]	$\langle N_{\mathrm{part}} \rangle$
0-5	348
5-10	290.8
10-20	217.9
20-30	144.7
30-40	91.04
40-50	52.42
50-60	27.77
60-70	13.78

Table 6: Centrality intervals and corresponding $\langle N_{\mathrm{part}} \rangle$ values.

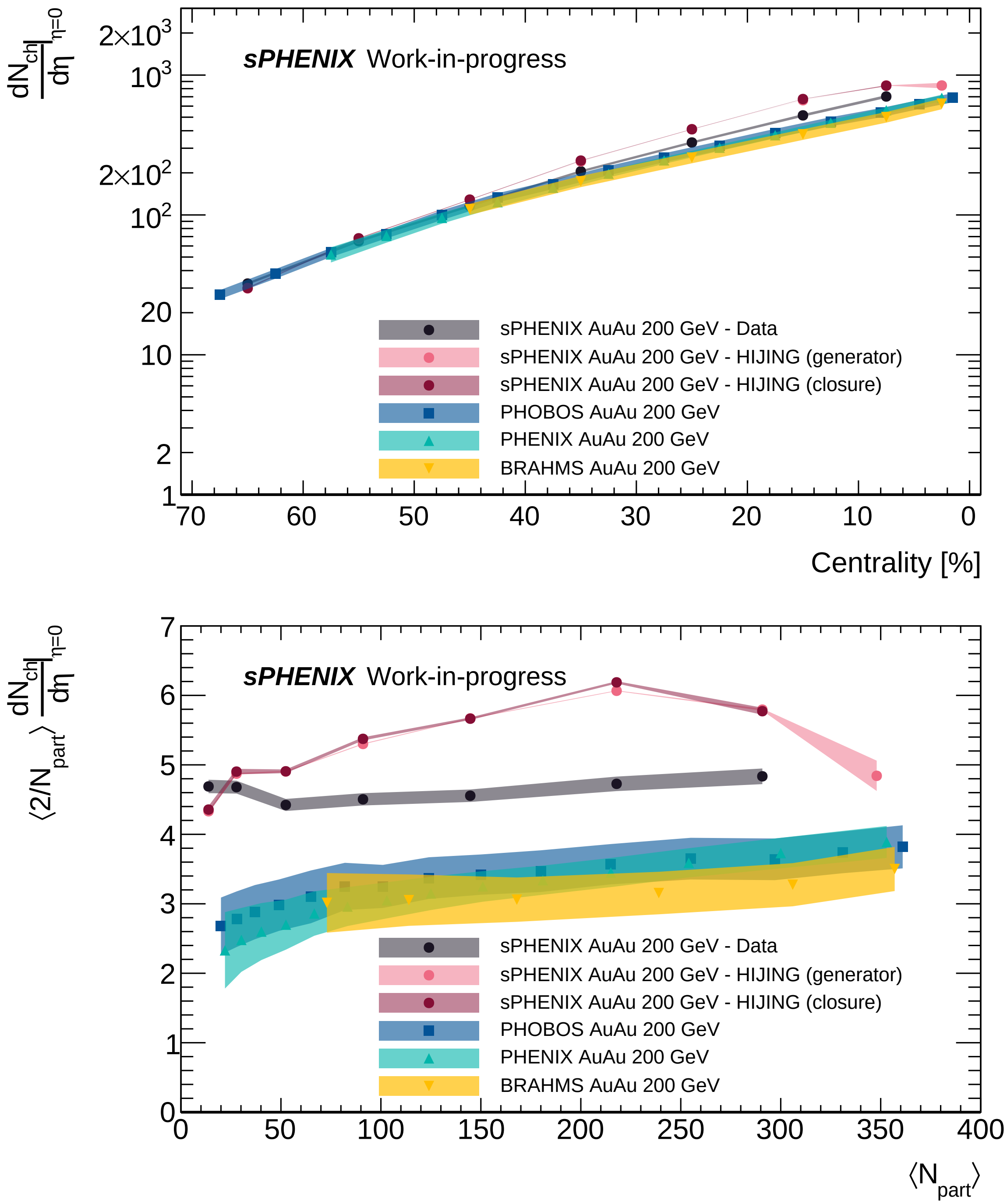

Figure 71: (Top) $\mathrm{dN_{ch}/d}\eta$ at midrapidity as a function of centrality intervals. (Bottom) The average $\mathrm{dN_{ch}/d}\eta$ at midrapidity normalized by $\langle N_{\mathrm{part}} \rangle$ as a function of $\langle N_{\mathrm{part}} \rangle$.

References

[1] Wit Busza, Krishna Rajagopal, and Wilke van der Schee. Heavy Ion Collisions: The Big Picture, and the Big Questions. Ann. Rev. Nucl. Part. Sci., 68:339–376, 2018. arXiv:1802.04801, doi:10.1146/annurev-nucl-101917-020852.

[2] Paul Romatschke and Ulrike Romatschke. Relativistic Fluid Dynamics In and Out of Equilibrium. Cambridge Monographs on Mathematical Physics. Cambridge University Press, 5 2019. arXiv:1712.05815, doi:10.1017/9781108651998.

[3] Javier L. Albacete and Cyrille Marquet. Gluon saturation and initial conditions for relativistic heavy ion collisions. Prog. Part. Nucl. Phys., 76:1–42, 2014. arXiv:1401.4866, doi:10.1016/j.ppnp.2014.01.004.

[4] Dmitri Kharzeev and Marzia Nardi. Hadron production in nuclear collisions at RHIC and high density QCD. Phys. Lett. B, 507:121–128, 2001. arXiv:nucl-th/0012025, doi:10.1016/S0370-2693(01)00457-9.

[5] David d'Enterria, Ralph Engel, Tanguy Pierog, Sergey Ostapchenko, and Klaus Werner. Constraints from the first LHC data on hadronic event generators for ultra-high energy cosmic-ray physics. Astropart. Phys., 35:98–113, 2011. arXiv:1101.5596, doi:10.1016/j.astropartphys.2011.05.002.

[6] K. Adcox et al. Centrality dependence of charged particle multiplicity in Au - Au collisions at S(NN)**(1/2) = 130-GeV. Phys. Rev. Lett., 86:3500–3505, 2001. arXiv:nucl-ex/0012008, doi:10.1103/PhysRevLett.86.3500.

[7] S. S. Adler et al. Systematic studies of the centrality and s(NN)**(1/2) dependence of the d E(T) / d eta and d (N(ch) / d eta in heavy ion collisions at mid-rapidity. Phys. Rev. C, 71:034908, 2005. [Erratum: Phys.Rev.C 71, 049901 (2005)]. arXiv:nucl-ex/0409015, doi:10.1103/PhysRevC.71.034908.

[8] B. B. Back et al. Charged particle multiplicity near mid-rapidity in central Au + Au collisions at $S^{(1/2)}$ = 56-A/GeV and 130-A/GeV. Phys. Rev. Lett., 85:3100–3104, 2000. arXiv:hep-ex/0007036, doi:10.1103/PhysRevLett.85.3100.

[9] B. Alver et al. Phobos results on charged particle multiplicity and pseudorapidity distributions in Au+Au, Cu+Cu, d+Au, and p+p collisions at ultra-relativistic energies. Phys. Rev. C, 83:024913, 2011. arXiv:1011.1940, doi:10.1103/PhysRevC.83.024913.

[10] K Aamodt et al. First proton-proton collisions at the LHC as observed with the ALICE detector: Measurement of the charged particle pseudorapidity density at s**(1/2) = 900-GeV. Eur. Phys. J. C, 65:111–125, 2010. arXiv:0911.5430, doi:10.1140/epjc/s10052-009-1227-4.

[11] K. Aamodt et al. Charged-particle multiplicity measurement in proton-proton collisions at $\sqrt{s}$ = 0.9 and 2.36 TeV with ALICE at LHC. Eur. Phys. J. C, 68:89–108, 2010. arXiv:1004.3034, doi:10.1140/epjc/s10052-010-1339-x.

[12] K. Aamodt et al. Charged-particle multiplicity measurement in proton-proton collisions at $\sqrt{s} = 7$ TeV with ALICE at LHC. Eur. Phys. J. C, 68:345–354, 2010. arXiv:1004.3514, doi:10.1140/epjc/s10052-010-1350-2.

[13] Jaroslav Adam et al. Pseudorapidity and transverse-momentum distributions of charged particles in proton–proton collisions at $\sqrt{s} = 13$ TeV. Phys. Lett. B, 753:319–329, 2016. arXiv:1509.08734, doi:10.1016/j.physletb.2015.12.030.

[14] Jaroslav Adam et al. Charged-particle multiplicities in proton–proton collisions at $\sqrt{s} =$ 0.9 to 8 TeV. Eur. Phys. J. C, 77(1):33, 2017. arXiv:1509.07541, doi:10.1140/epjc/s10052-016-4571-1.

[15] S. Acharya et al. Charged-particle multiplicity distributions over a wide pseudorapidity range in proton-proton collisions at $\sqrt{s} = 0.9$, 7, and 8 TeV. Eur. Phys. J. C, 77(12):852, 2017. arXiv:1708.01435, doi:10.1140/epjc/s10052-017-5412-6.

[16] Shreyasi Acharya et al. Pseudorapidity distributions of charged particles as a function of mid- and forward rapidity multiplicities in pp collisions at $\sqrt{s} = 5.02$, 7 and 13 TeV. Eur. Phys. J. C, 81(7):630, 2021. arXiv:2009.09434, doi:10.1140/epjc/s10052-021-09349-5.

[17] K Aamodt et al. Charged-particle multiplicity density at mid-rapidity in central Pb-Pb collisions at $\sqrt{s_{NN}} = 2.76$ TeV. Phys. Rev. Lett., 105:252301, 2010. arXiv:1011.3916, doi:10.1103/PhysRevLett.105.252301.

[18] Jaroslav Adam et al. Centrality Dependence of the Charged-Particle Multiplicity Density at Midrapidity in Pb-Pb Collisions at $\sqrt{s_{\mathrm{NN}}} = 5.02$ TeV. Phys. Rev. Lett., 116(22):222302, 2016. arXiv:1512.06104, doi:10.1103/PhysRevLett.116.222302.

[19] Shreyasi Acharya et al. Centrality and pseudorapidity dependence of the charged-particle multiplicity density in Xe–Xe collisions at $\sqrt{s_{\mathrm{NN}}}$ =5.44TeV. Phys. Lett. B, 790:35–48, 2019. arXiv:1805.04432, doi:10.1016/j.physletb.2018.12.048.

[20] CMS Collaboration. Study of Charged Hadron Multiplicity in Minimum Bias p+p Collisions at $\sqrt{s} = 0.9$ and 10 TeV. Technical report, CERN, Geneva, 2009. URL: https://cds.cern.ch/record/1194513.

[21] Vardan Khachatryan et al. Transverse Momentum and Pseudorapidity Distributions of Charged Hadrons in pp Collisions at $\sqrt{s} = 0.9$ and 2.36 TeV. JHEP, 02:041, 2010. arXiv:1002.0621, doi:10.1007/JHEP02(2010)041.

[22] Vardan Khachatryan et al. Transverse-momentum and pseudorapidity distributions of charged hadrons in *pp* collisions at $\sqrt{s} = 7$ TeV. Phys. Rev. Lett., 105:022002, 2010. arXiv:1005.3299, doi:10.1103/PhysRevLett.105.022002.

[23] Vardan Khachatryan et al. Charged Particle Multiplicities in *pp* Interactions at $\sqrt{s} =$ 0.9, 2.36, and 7 TeV. JHEP, 01:079, 2011. arXiv:1011.5531, doi:10.1007/JHEP01(2011)079.

[24] Serguei Chatrchyan et al. Measurement of pseudorapidity distributions of charged particles in proton-proton collisions at $\sqrt{s} = 8$ TeV by the CMS and TOTEM experiments. Eur. Phys. J. C, 74(10):3053, 2014. arXiv:1405.0722, doi:10.1140/epjc/s10052-014-3053-6.

[25] Vardan Khachatryan et al. Pseudorapidity distribution of charged hadrons in proton-proton collisions at $\sqrt{s} = 13$ TeV. Phys. Lett. B, 751:143–163, 2015. arXiv:1507.05915, doi:10.1016/j.physletb.2015.10.004.

[26] Albert M Sirunyan et al. Pseudorapidity distributions of charged hadrons in proton-lead collisions at $\sqrt{s_{\mathrm{NN}}} = 5.02$ and 8.16 TeV. JHEP, 01:045, 2018. arXiv:1710.09355, doi:10.1007/JHEP01(2018)045.

[27] Serguei Chatrchyan et al. Dependence on pseudorapidity and centrality of charged hadron production in PbPb collisions at a nucleon-nucleon centre-of-mass energy of 2.76 TeV. JHEP, 08:141, 2011. arXiv:1107.4800, doi:10.1007/JHEP08(2011)141.

[28] CMS Collaboration. Pseudorapidity distributions of charged hadrons in PbPb collisions at $\sqrt{s_{\mathrm{NN}}} = 5.36$ TeV. Technical report, CERN, Geneva, 2023. URL: https://cds.cern.ch/record/2871619.

[29] Albert M Sirunyan et al. Pseudorapidity distributions of charged hadrons in xenon-xenon collisions at $\sqrt{s_{\mathrm{NN}}} = 5.44$ TeV. Phys. Lett. B, 799:135049, 2019. arXiv:1902.03603, doi:10.1016/j.physletb.2019.135049.

[30] Georges Aad et al. Measurement of the centrality dependence of the charged-particle pseudorapidity distribution in proton–lead collisions at $\sqrt{s_{\mathrm{NN}}} = 5.02$ TeV with the ATLAS detector. Eur. Phys. J. C, 76(4):199, 2016. arXiv:1508.00848, doi:10.1140/epjc/s10052-016-4002-3.

[31] Georges Aad et al. Measurement of the centrality dependence of the charged particle pseudorapidity distribution in lead-lead collisions at $\sqrt{s_{NN}} = 2.76$ TeV with the ATLAS detector. Phys. Lett. B, 710:363–382, 2012. arXiv:1108.6027, doi:10.1016/j.physletb.2012.02.045.

[32] Alexander Milov. Charged particle multiplicity measurement in au-au collisions using the pad chambers of the phenix detector at rhic, May 2002. doi:10.5281/zenodo.3983557.

[33] sPHENIX Collaboration. Commissioning status: August 2023, 2023. Indico: https://indico.bnl.gov/event/20373/attachments/49393/84311/Commissioning_Status_August_2023.pdf.

[34] sPHENIX Collaboration. sphenix centrality calibration for run-23 au+au 200 gev, 2024. sPHENIX note on Invenio: https://sphenix-invenio.sdcc.bnl.gov/communities/sphenixcommunity/requests/d297c5eb-63fa-4ca5-9c43-7a77257bb593.

[35] C. Aidala et al. The PHENIX Forward Silicon Vertex Detector. Nucl. Instrum. Meth. A, 755:44–61, 2014. arXiv:1311.3594, doi:10.1016/j.nima.2014.04.017.

[36] James R. Hoff, Tom N. Zimmerman, Raymond J. Yarema, Jon S. Kapustinsky, and Melynda L. Brookes. Fphx: A new silicon strip readout chip for the phenix experiment at rhic. In 2009 IEEE Nuclear Science Symposium Conference Record (NSS/MIC), pages 75–79, 2009. doi:10.1109/NSSMIC.2009.5401873.

[37] James R. Hoff, Tom N. Zimmerman, Raymond J. Yarema, Jon S. Kapustinsky, and Melynda L. Brookes. Fphx: A new silicon strip readout chip for the phenix experiment at rhic. In 2009 IEEE Nuclear Science Symposium Conference Record (NSS/MIC), pages 75–79, 2009. doi:10.1109/NSSMIC.2009.5401873.

[38] Hao-Ren Jheng et al. Intt survey geometry. Analysis report on sPHENIX Indico, 2024. URL: https://indico.bnl.gov/event/22918/#16-intt-survey-geometry.

[39] Hao-Ren Jheng et al. Mvtx geometry. Analysis report on sPHENIX Indico, 2024. URL: https://indico.bnl.gov/event/24940/#14-mvtx-geometry-update.

[40] T. Miao, H. Wenzel, F. Yumiceva, and N. Leioatts. Beam position determination using tracks, 8 2007.

[41] sPHENIX Collaboration. Intt vertex reconstruction, 2024. sPHENIX note on Invenio: https://sphenix-invenio.sdcc.bnl.gov/communities/sphenixcommunity/requests/717c5d51-65dc-4a5b-877b-bc19789f21f7.

Appendices

A INTT bad channel masks

This section shows the supporting plots for the INTT hot, dead, and cold channel masks. Figure 72–75 show the distributions of channels classified as hot, dead, cold, and good, respectively.

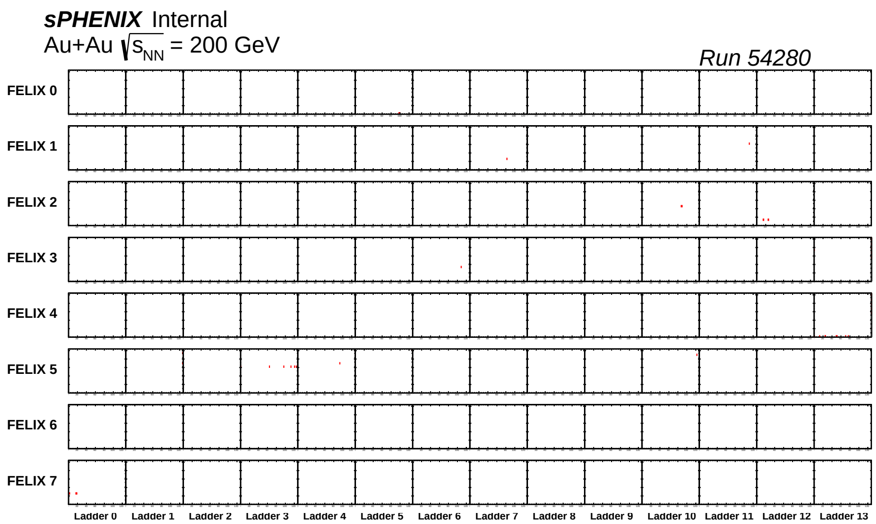

Figure 72: The map of hot channels of run 54280.

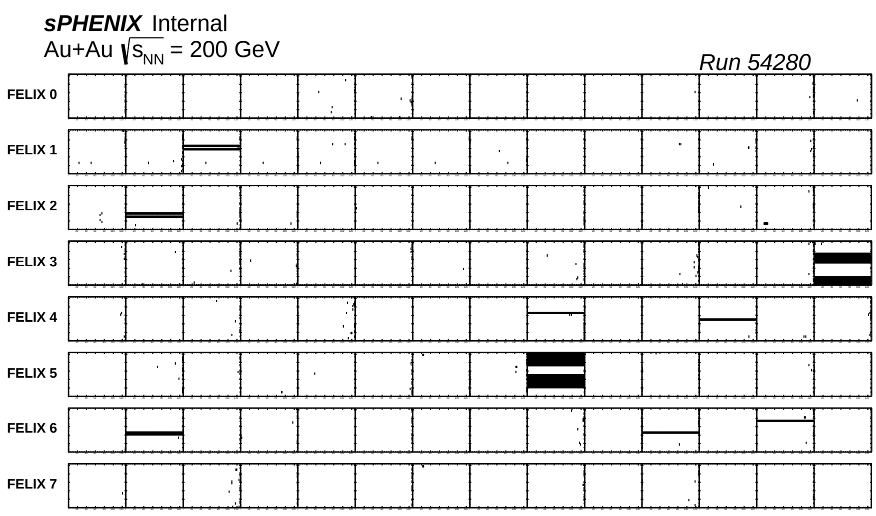

Figure 73: The map of dead channels of run 54280.

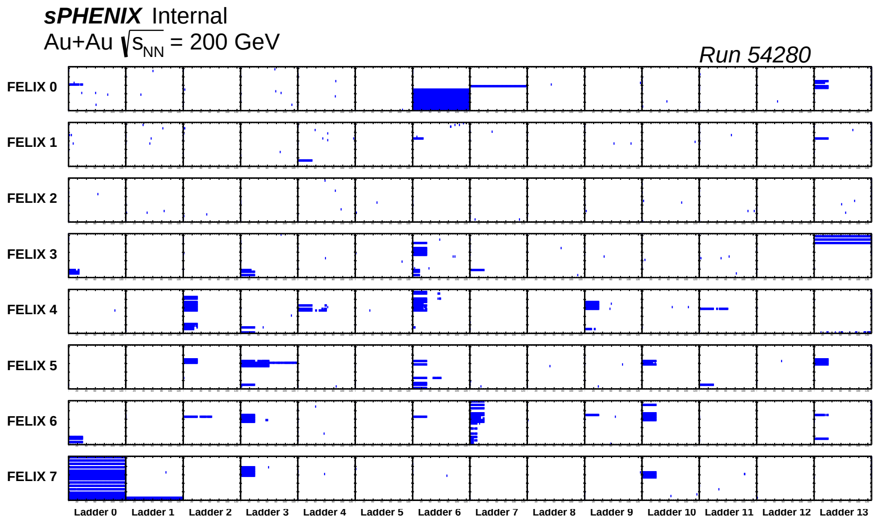

Figure 74: The map of cold channels of run 54280.

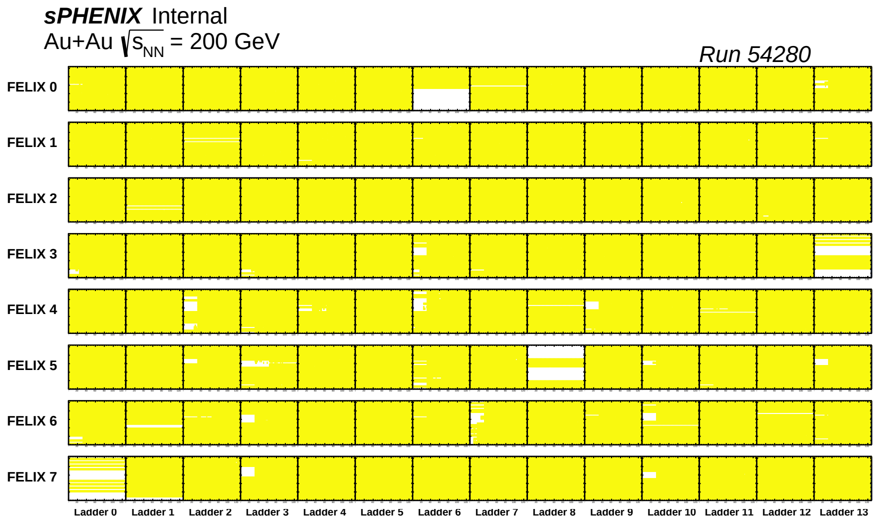

Figure 75: The map of good channels of run 54280.

B INTT geometry with survey measurement

(Numbers are quoted with 4 significant figures for consistency throughout this section.)

The survey measurement performed after the installation of INTT indicated a gap between two INTT half barrels. This gap is reflected as dips in the azimuthal angle distribution of the INTT strips, as shown in Figure 76.

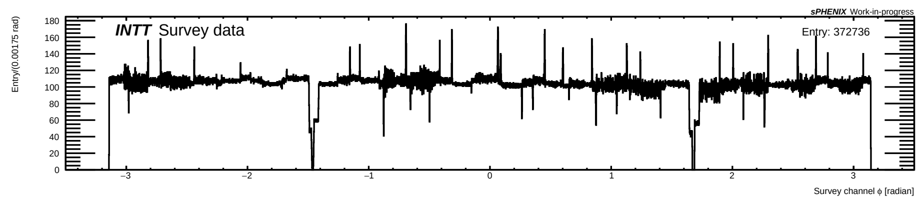

Figure 76: Azimuthal angle distribution of INTT channels, calculated from the survey measurement.

The INTT GEANT4 geometry model is modified accordingly to account for the acceptance difference between ideal and misaligned detector placement. The following list describes the modifications:

1. The dimensions of the GEANT4 volume representing the space between the active area and the stave peek are updated from an incorrect default value of 7.622 mm to 0.8000 mm based on the production design.

2. The equivalent specifications of the metal and carbon support rings representing the INTT stave peek and the INTT ladder support structure at both ends of INTT barrel are updated from 0.5000 cm to 0.7500 cm and from 0.7500 cm to 0.3125 cm in length respectively. The radii of both rings are updated such that an equivalent material budget as the production design is achieved. The detail is shown in Figure 77.

3. The physical position along the sPHENIX Z-axis of both support rings is automatically adjusted by accurately setting the values of their lengths (see item 2).

4. The center position of both support rings and the inner and outer barrel support skins with respect to the sPHENIX origin is adjusted according to the averaged X and Y positions of all INTT ladders based on the survey, which corresponds to 0.4025 mm and -2.886 mm in both X and Y axes, respectively.

5. The sensor's positions and rotations relative to the ladder remain unchanged with the default ideal geometry. The translations and rotations of the sensor relative to the sPHENIX coordinates are adjusted according to the survey measurement of the physical ladder to which the sensor belongs. These adjustments include (a) the translation in the X and Y directions of the individual ladder, (b) the average translation in the Z direction of all ladders, and (c) the rotation around the Z-axis of the ladder (which is parallel to the sPHENIX Z-axis).

6. A shift in the Z direction with respect to the sPHENIX origin is applied to both support rings and the inner and outer barrel support skins according to the average translation in the Z direction of all ladders.

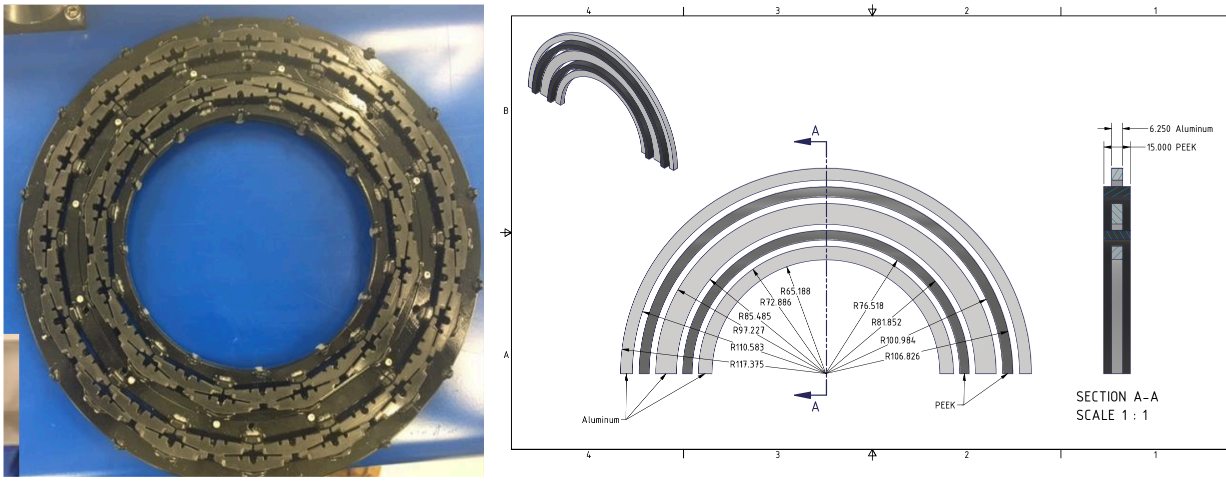

Figure 77: (Left) Mock module of the INTT endcap support structure. (Right) Simplified Geant4 volume design of the INTT endcap support structure.

An offset is applied to account for various factors when translating the survey measurement to the X and Y coordinates of the Geant4 physical volume placement for the INTT ladder. This offset encompasses the point where the survey probe touches the ladder's surface (illustrated by the dashed green line in Figure 78), as well as the thicknesses of the sensor (the bottom red box in Figure 78), glue, high-density interface (the blue box above the sensor), and carbon fiber plate (the grey shape above the high-density interface). A 0.2282 mm radially inward is given to the offset, derived by subtracting the distance of 2.386 mm between the survey measurement point and the bottom of the sensor from the 2.158 mm between the center of the INTT Geant4 physical volume and the sensor's bottom.

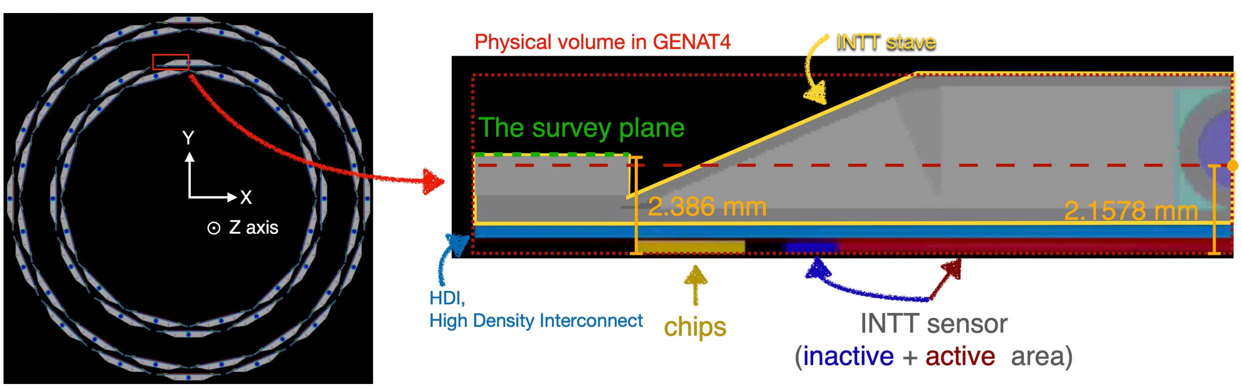

Figure 78: The drawing presents the amount of correction.

The center of INTT half barrels on the transverse plane is determined by averaging the X and Y positions of the ladders obtained from the survey measurement and found to be shifted to (0.4027 mm, −2.887 mm) relative to the ideal position at (0.000 mm, 0.000 mm). Figure 79 shows the center position of ladders in the ideal GEANT4 geometry (in red) and as measured from the survey (in blue).

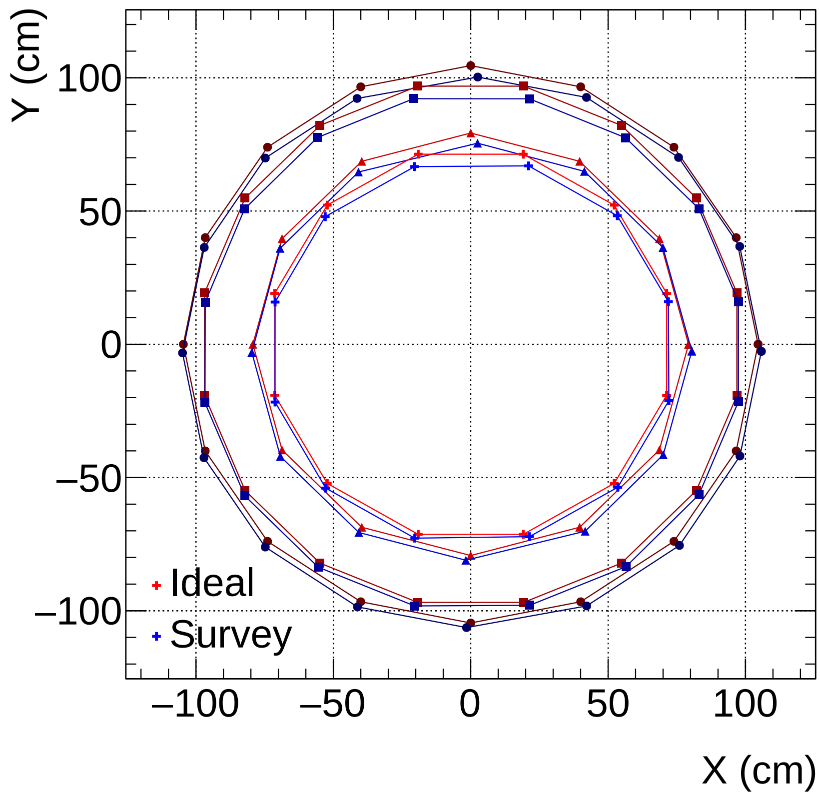

Figure 79

The INTT ladders are shifted individually along the sPHENIX Z-axis, as shown in Figure 80, resulting in an average displacement of −4.724 mm relative to the nominal position at 0 mm. The standard deviation of these longitudinal shifts is 0.1904 mm, an order of magnitude smaller than the mean shift. Consequently, a uniform translation in the Z position of the sensor is applied, as outlined in item 5 of the preceding list.

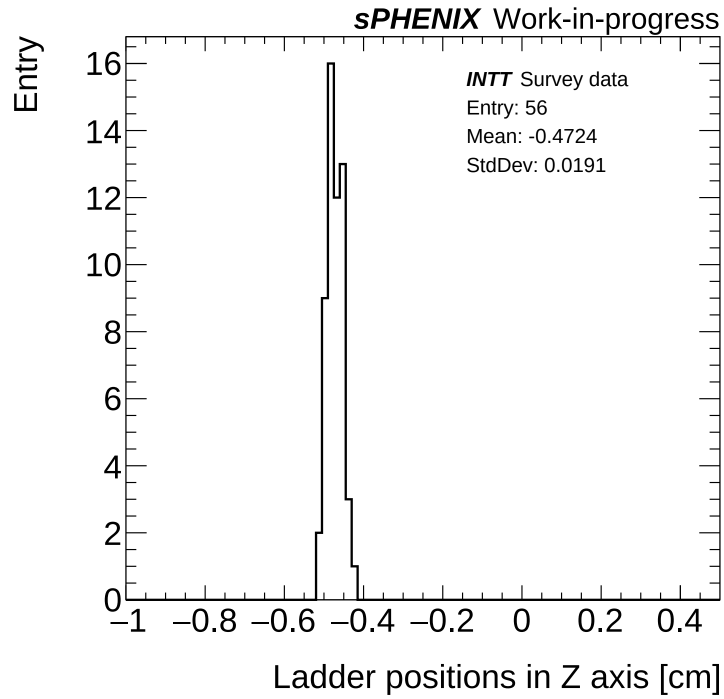

Figure 80: Center positions in the Z direction of all ladders according to the survey.

A sample of 100 simulated events is generated using the single-particle generator in the sPHENIX simulation production framework to verify the updated geometry. Within each event, 2000 charged pions are uniformly sampled in $-\pi \leq \phi \leq \pi$ and $-1 \leq \eta \leq 1$. The resulting ϕ and η distributions of reconstructed clusters, referred to as TrkrCluster in the sPHENIX software, are shown in Figure 81. The visible dips in the cluster ϕ distribution are consistent with those shown in Figure 76.

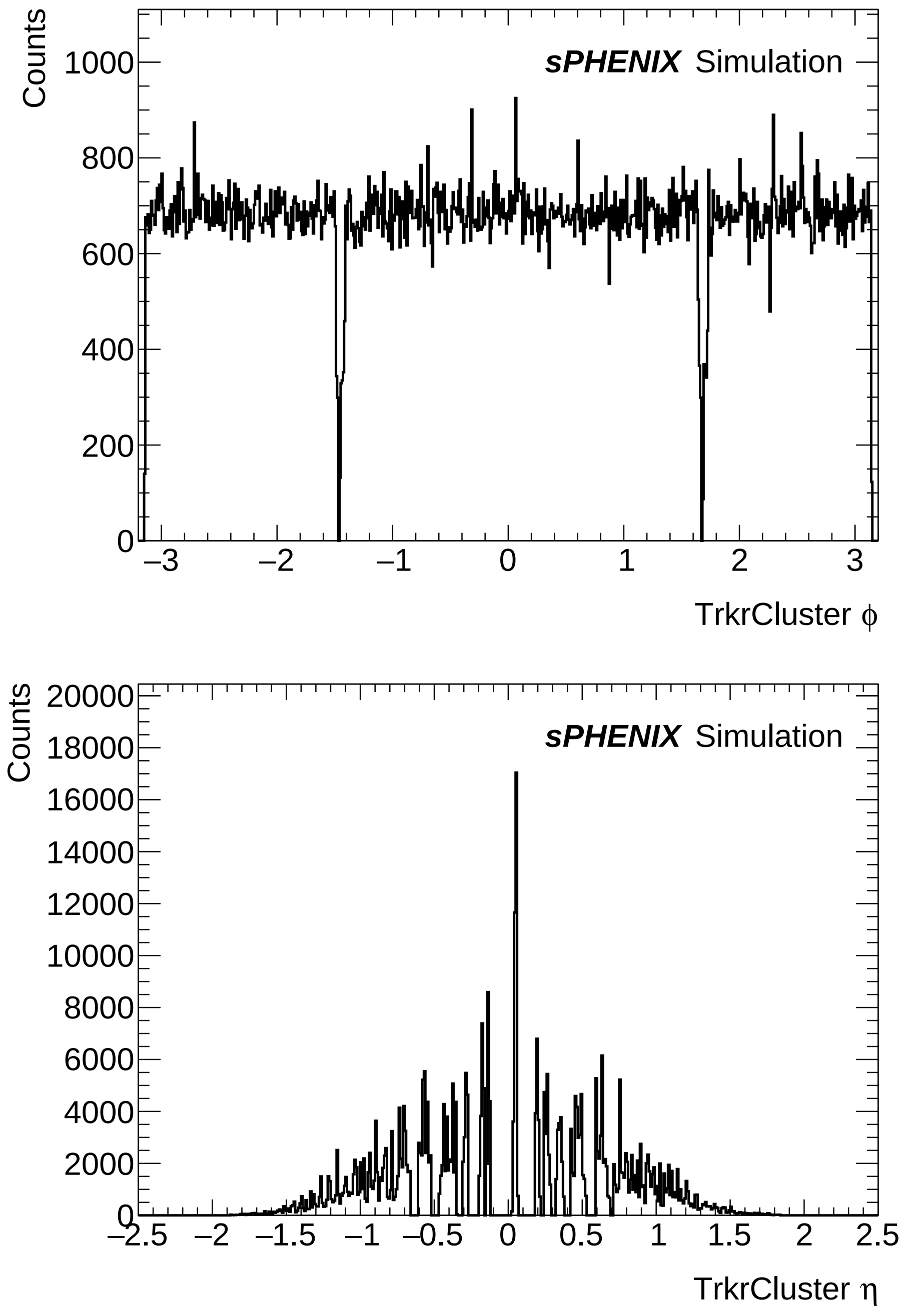

Figure 81

1000 The final implementation can be found at the sPHENIX GitHub coresoftware repository.
1001 Packages that are modified for the final deployment of the updated geometry include:

1002 • simulation/g4simulation/g4intt: https://github.com/sPHENIX-Collaboration/c
1003 oresoftware/tree/master/simulation/g4simulation/g4intt

1004 • offline/packages/intt: https://github.com/sPHENIX-Collaboration/coresoftwar
1005 e/tree/master/offline/packages/intt

- offline/packages/trackreco: https://github.com/sPHENIX-Collaboration/coresoftware/tree/master/offline/packages/trackreco

Two pull requests for integrating the modifications into the sPHENIX software framework are

- sPHENIX-Collaboration/macros: https://github.com/sPHENIX-Collaboration/macros/pull/790
- sPHENIX-Collaboration/coresoftware: https://github.com/sPHENIX-Collaboration/coresoftware/pull/2595

sPHENIX Jenkins continuous integration system performs various quality assurance tests. The resulting build and test reports include diagnostic plots for QA, which can be accessed from the link provided.

C Supplementary plots for cluster distributions

This section presents additional cluster distributions in data and simulation. The selection criteria have been slightly relaxed, with no cuts applied to the cluster ϕ-size and ADC.

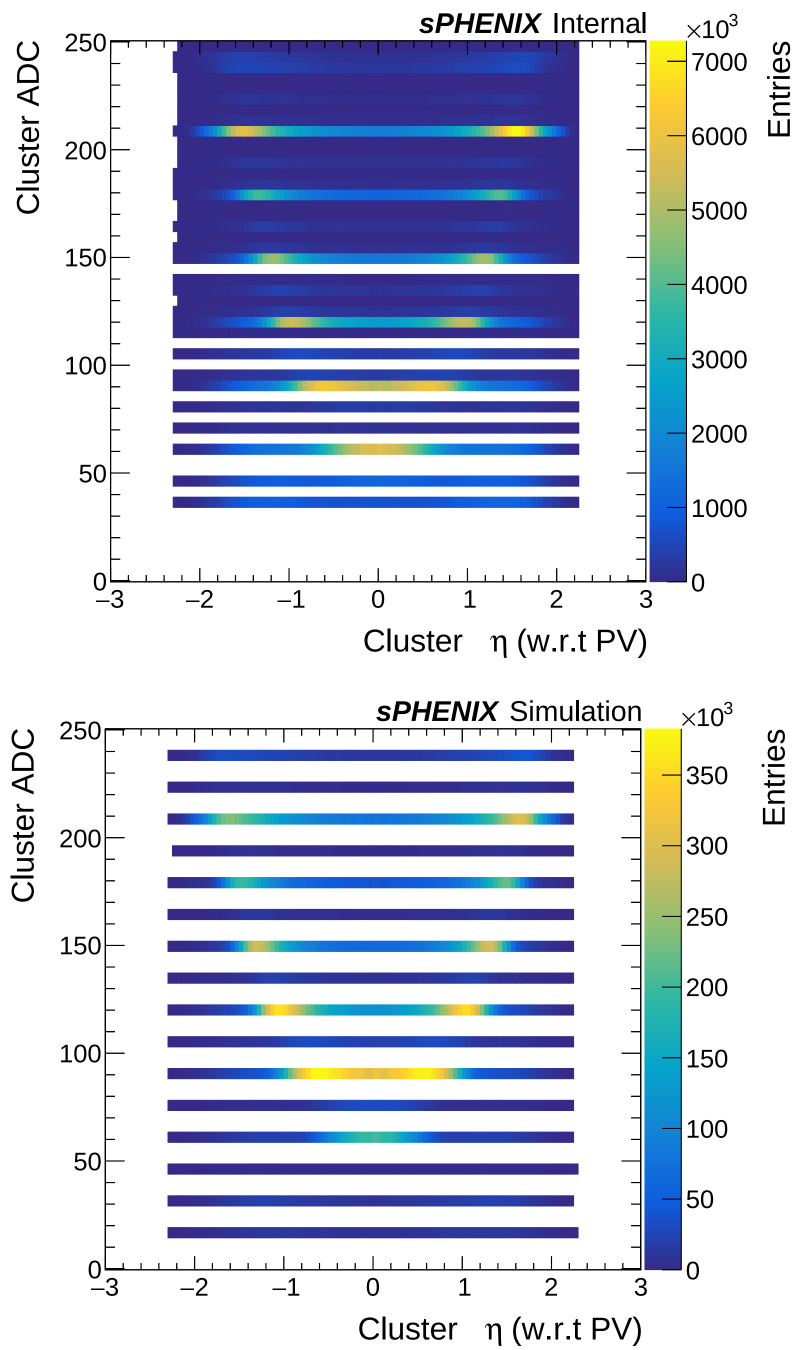

Figure 82: The cluster η versus cluster ADC in data (top) and simulation (bottom).

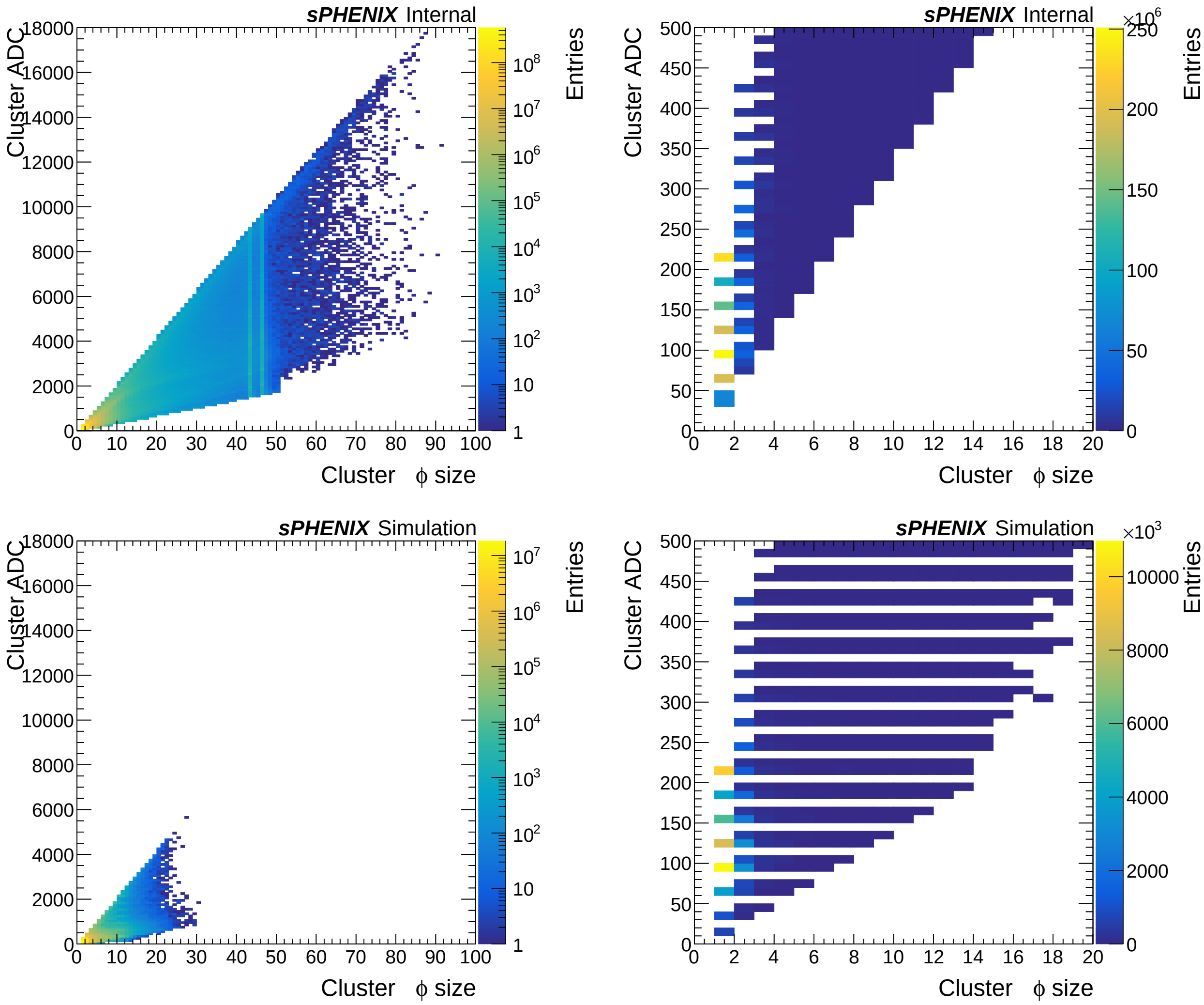

Figure 83: The cluster ϕ-size versus cluster ADC distributions are shown for data (top) and simulation (bottom). The plots on the left display a wider axis range, while those on the right provide a zoomed-in view.

D Discrepancy in cluster ϕ-size and ADC distributions between data and simulation

A simplified model is implemented in the Fun4All module, PHG4InttHitReco, to approximate charge diffusion in silicon. For each charged particle passing through the active region, a column with a fixed radius, referred to as the diffusion radius, is defined to represent the range of charge diffusion. A check is then performed to determine whether this column overlapped with a strip and to calculate the overlapping area. This overlap is used to assign the energy deposit to the strip, assuming a uniform energy profile across the column's cross-section. After the charge diffusion step, clustering is performed by grouping adjacent strips with non-zero energy deposits. The cluster ϕ-size is determined as the number of strips with non-zero energy deposits within a cluster, while the cluster ADC is calculated as the sum of the ADC values of those strips.

A control sample of clusters is defined and constructed to enable a fair comparison between data and simulation and to ensure that the selected clusters primarily originate from collisions rather than beam background. First, hits are clustered using the standard Z-clustering algorithm. From the resulting collection of clusters, those with a pseudorapidity $|\eta| < 0.1$ and a cluster Z-size of 1 are selected. These criteria ensure that the selected clusters are most likely produced by particles incident perpendicularly to the INTT strips.

Figure 84 compares the cluster ϕ-size and ADC distributions of the control sample in data against simulations using different diffusion parameters. The distributions of data without Z-clustering are normalized to 1, while the distributions with Z-clustering are scaled based on the ratio of their integral to the non-Z-clustered data. In simulations with a large diffusion radius, the cluster ϕ-size and ADC values can extend to the maximum observed in the data. However, the shapes of the simulated distributions deviate from the data in the intermediate region. In addition, the data-to-simulation ratios for both cluster ϕ-size and ADC deviate from 1, indicating that none of the tested diffusion radii in the simulation fully reproduce the observed behavior in data.

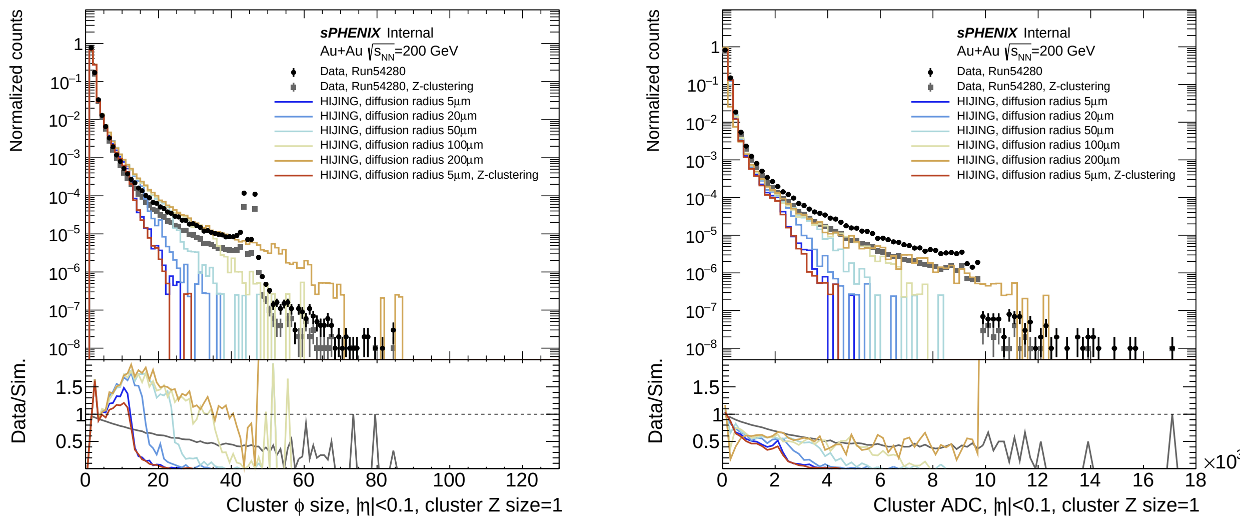

Figure 84: The cluster ϕ-size (left) and ADC (right) distributions of the selected control sample in data and simulations with different diffusion parameters.

The beamspot, event vertex, and tracklet reconstructions in the CMS approach are performed on simulation samples with different diffusion radii. Figure 85 presents the cluster η and the reconstructed tracklet distributions in data and simulations with varying diffusion parameters. Notably, the shapes of the distributions for simulations with large diffusion radii differ significantly from those with smaller diffusion parameters. This difference can be explained by the fact that, for a large diffusion radius, a particle in the simulation spreads its energy deposits across multiple strips. As a result, the constant cluster ADC cut disproportionately impacts the low-η region, leading to a distorted distribution.

The substantial difference in the tracklet η distributions for simulations with a large diffusion radius introduces significant variation in the correction factor compared to simulations with smaller diffusion parameters. This variation results in a large systematic effect when the diffusion parameter is varied. Consequently, the baseline analysis uses simulations with the default diffusion parameter of 5μm.

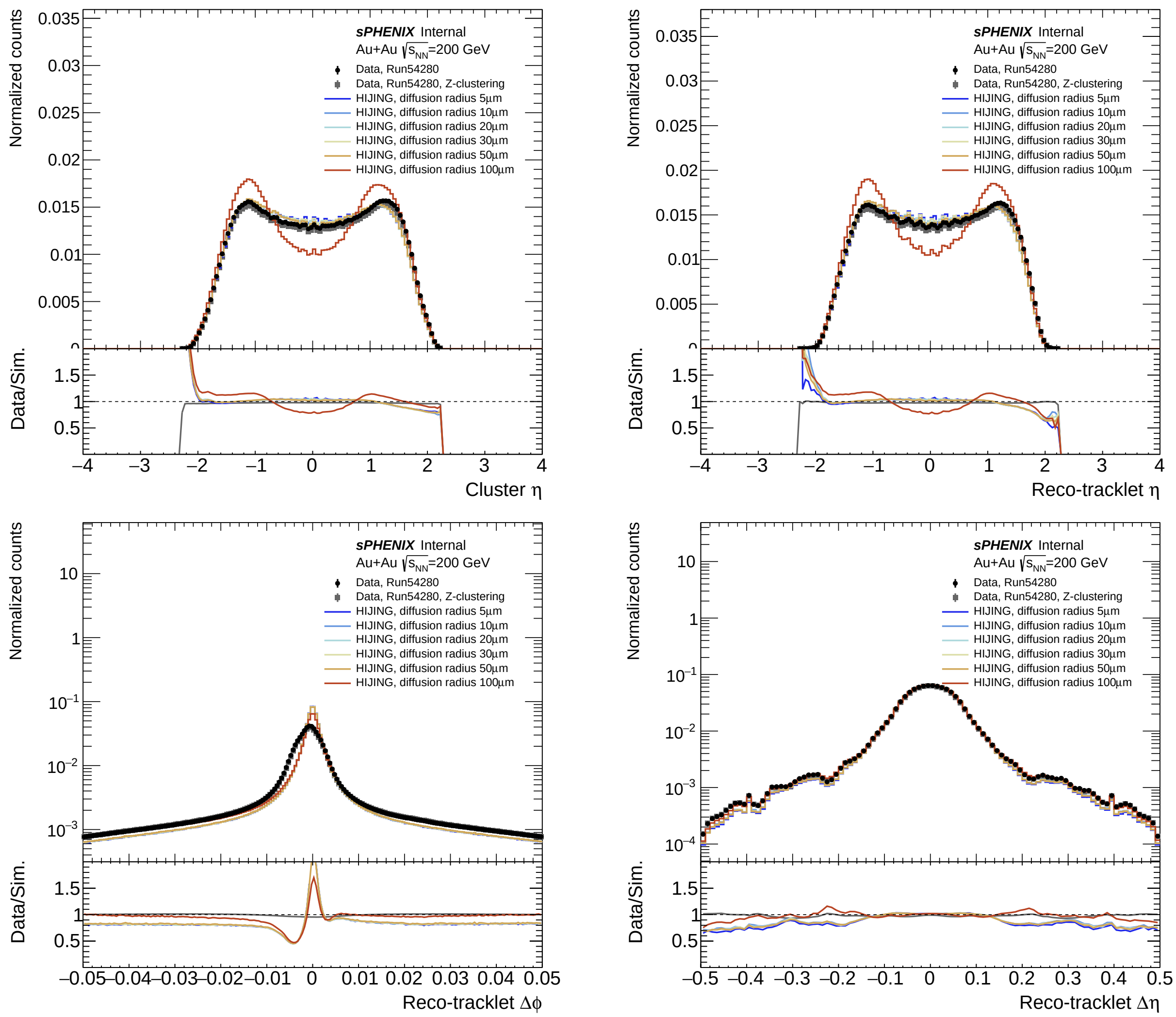

Figure 85: The cluster η (top left) reconstructed tracklet η (top right), $\Delta\phi$ (bottom left), and $\Delta\eta$ (bottom right) distributions in data and simulations with different diffusion parameters.

E Supplementary plots for vertex reconstruction in the PHOBOS approach

The $\Delta\phi$ and DCA cuts used int proto-tracklets selection for vertex Z reconstruction are 0.6 degrees and 0.1 cm, respectively. This is supported by the previous cut scan study with the simulation sample of run 20869, as shown in Figure 86.

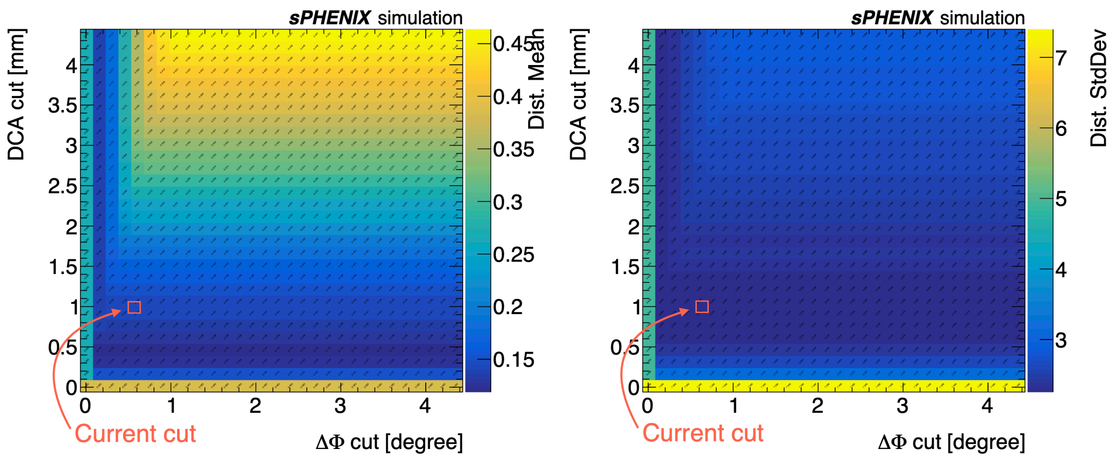

Figure 86: The mean (left) and standard deviation (right) of the ΔZ distribution as a function of $\Delta\phi$ and DCA cuts, where ΔZ is the difference between INTT vtxZ and truth vertex Z.

The vertex Z reconstruction performance is studied with simulation sample of run 54280, as shown in Figure 87, and Figure 88 for the high multiplicity events. The wiggling structure observed in the correlation between ΔZ, the difference between INTT vtxZ and truth vertex Z, and truth vertex Z is expected to be due to the intrinsic INTT sensor geometry. And the vertex Z reconstruction resolution of 0.15 mm is measured for the high-multiplicity events, which is one order of magnitude smaller than the INTT strip length, 1.6 or 2.0 cm. The INTT vertex Z reconstruction efficiency is shown in Figure 89, where the efficiency is defined as the fraction of the number of events with $\Delta Z < 1$ cm. The efficiency of vertex Z reconstruction is consistently at unity up to centrality 70%.

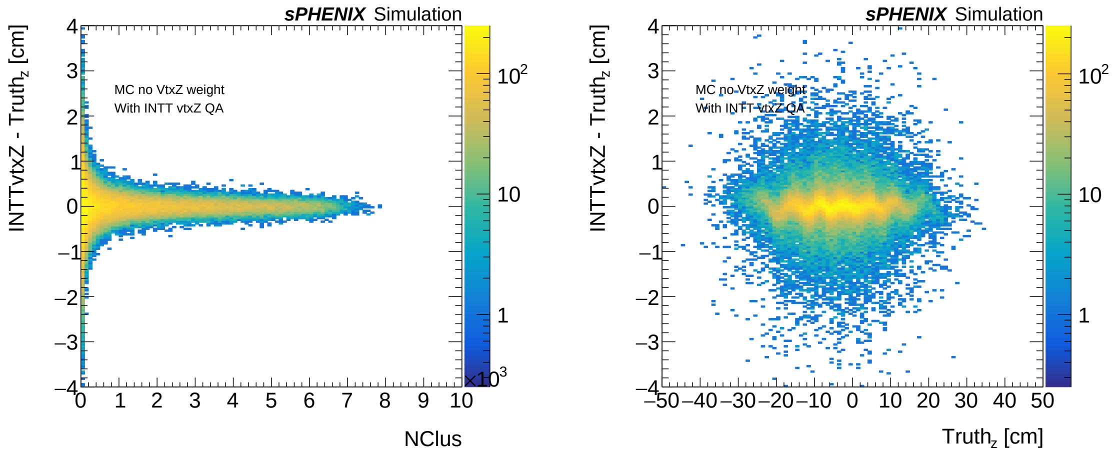

Figure 87: Left: The ΔZ as a function of number of INTT clusters. Right: The ΔZ as a function of truth vertex Z.

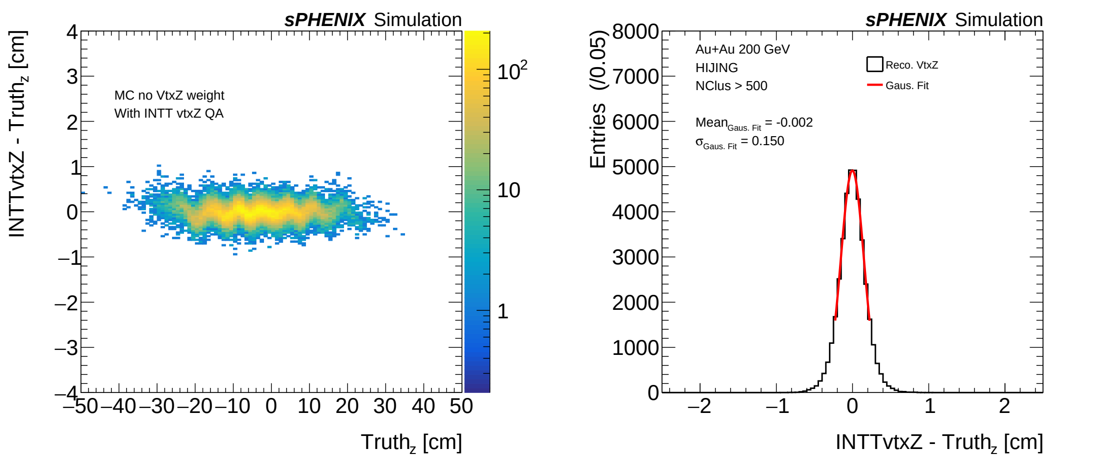

Figure 88: Left: The ΔZ as a function of truth vertex Z for the events with numbers of INTT clusters > 500. Right: The vertex Z reconstruction resolution for the high-multiplicity events.

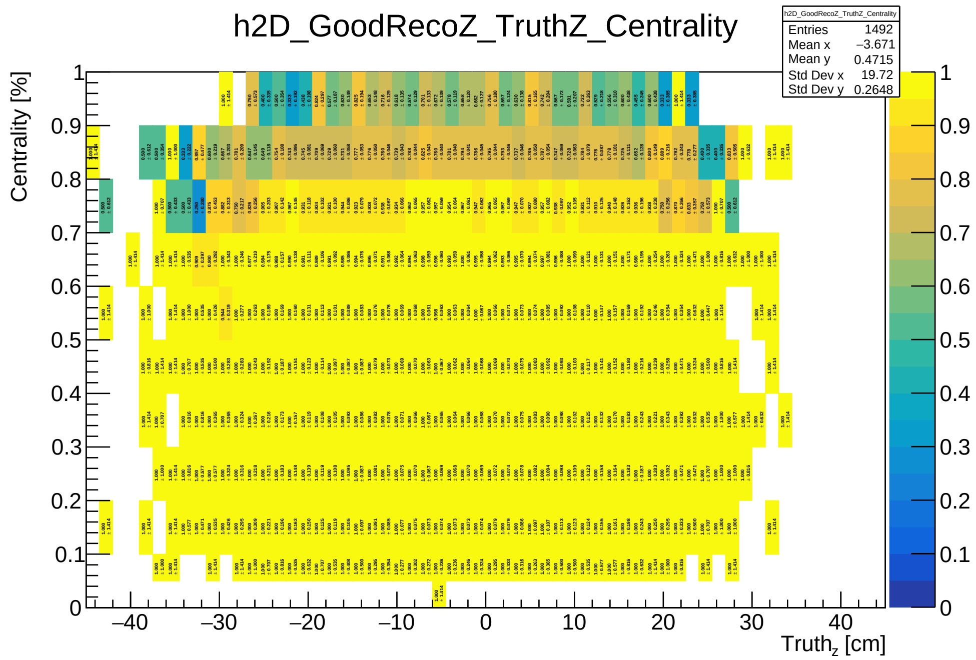

Figure 89: The vertex Z reconstruction efficiency as a function of centrality bin and truth vertex Z.

In data, the correlation of vertex Z reconstructed by INTT and MBD is checked, as shown in Figure 90. A positive correlation is identified indicating the reliability of the algorithm developed. The cause of the two satellite groups along the major correlation is under investigation. It is expected to be due to the MBD calibration. The two satellite groups are discarded in the PHOBOS-style analysis, as mentioned in Section 5.4.

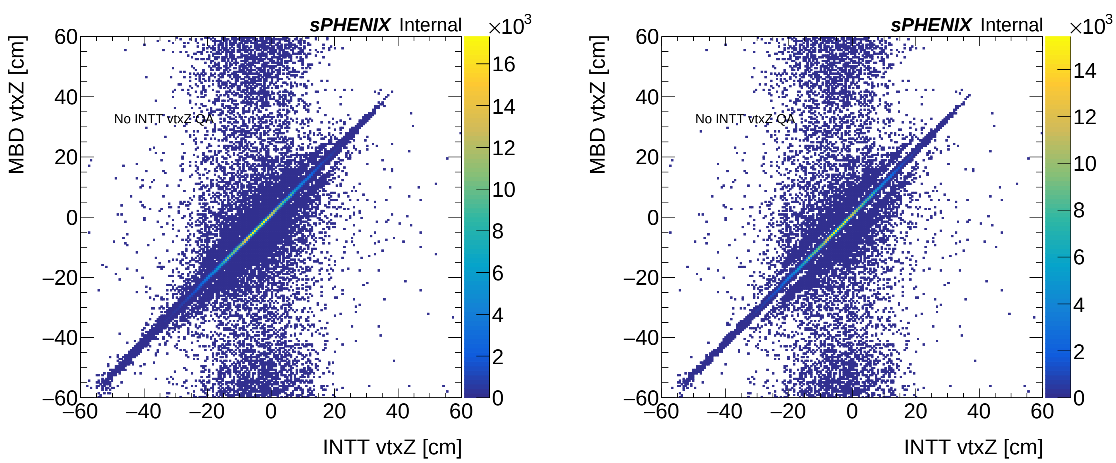

Figure 90: The correlation of vertex Z reconstructed by INTT and MBD for centrality interval $0 - 70\%$ (left) and the events with numbers of INTT clusters > 500 (right).

In data, the reconstructed vertex Z distribution for each centrality interval is compared to that for the centrality interval 0-70% for the reliability study, as shown Figure 91. The good agreement is observed up to the centrality interval of 70–80%.

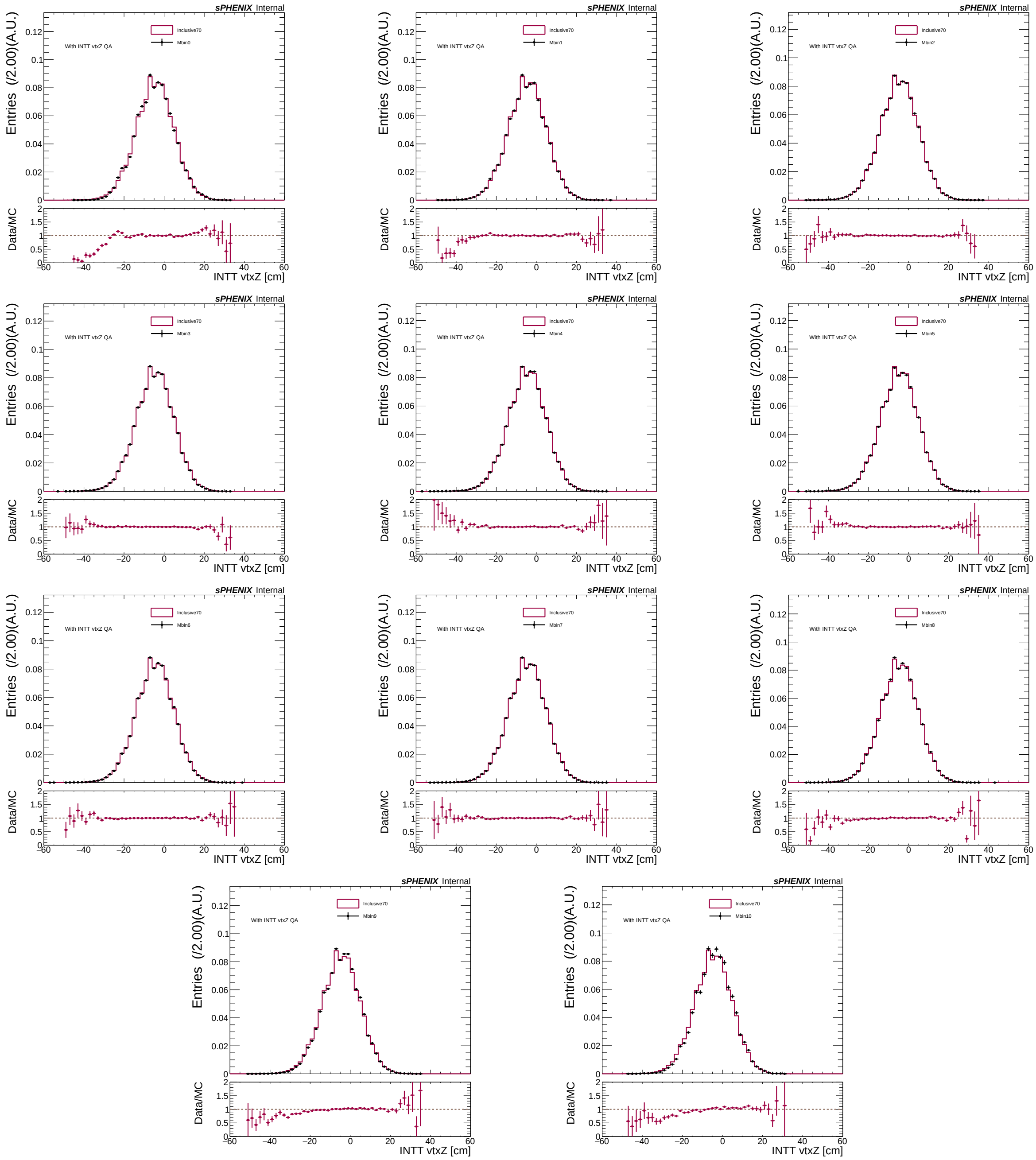

Figure 91: In data, the reconstructed vertex Z distribution for each centrality interval comparing to that of for the centrality interval 0-70%.

E.1 Per-event vertex X/Y position reconstruction

(This section presents a feasibility study of reconstructing the beam spot width performed in Run2023.)

With the average-vertex XY and the per-event vertex Z in place, the per-event vertex XY position reconstruction can be feasible. The limit of INTT is therefore extended forward. Note that reconstructing the event-by-event vertex XY is mainly for obtaining the beam spot size and vertex-position stability. The idea is similar to the 2D tracklet fill method as described in Section 5.4.2. On the contrary, the events with high multiplicities are expected to have higher precision as more information can be included in the reconstruction. The steps are described in the following:

1. Define the dimensions and center of a finely-binned 2D histogram. The central point is determined by the average vertex XY position. In the standard configuration, this corresponds to a 5 mm $\times$ 5 mm square with bin sizes of 50 μm $\times$ 50 μm.

2. In an event, start with a cluster in the inner layer and loop over the clusters in the outer layer. The combinations with cluster $\Delta\phi < 5$ degrees and the strip Z positions able to link to the reconstructed per-event vertex Z position are kept. Move to the next inner-layer cluster, and repeat the procedure.

3. Populate the trajectories of the combinations into the 2D histogram. The example is shown in Figure 92.

4. Remove the background of the histogram.

5. The per-event vertex XY are obtained by taking the averages on both axes of the histogram, as shown in Figure 92.

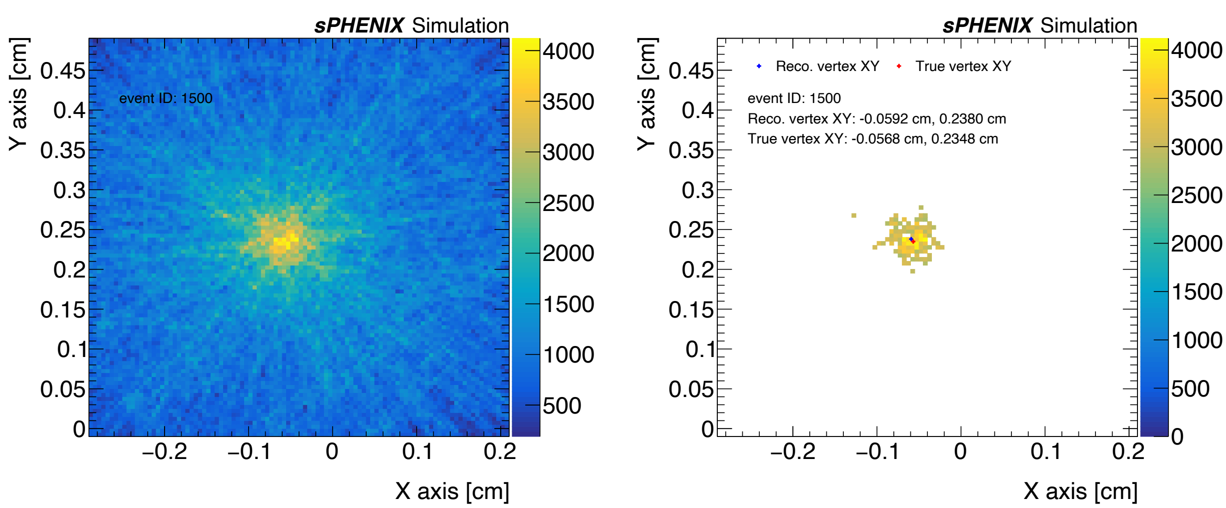

Figure 92: 2D histogram filled by the trajectories of combinations (left) and post background removal (right). The red and blue full cross marks are true and reconstructed vertex XY, respectively.

The reconstructed per-event vertex XY is compared with the true vertex XY in the simulation. Figure 93 and 94 show the correlations and deviations between true and reconstructed vertices for both axes. The correlations described by linear fits are consistent with unity, indicating good reliability of the current reconstruction method. In general, the resolution is 30 μm for the high-multiplicity events.

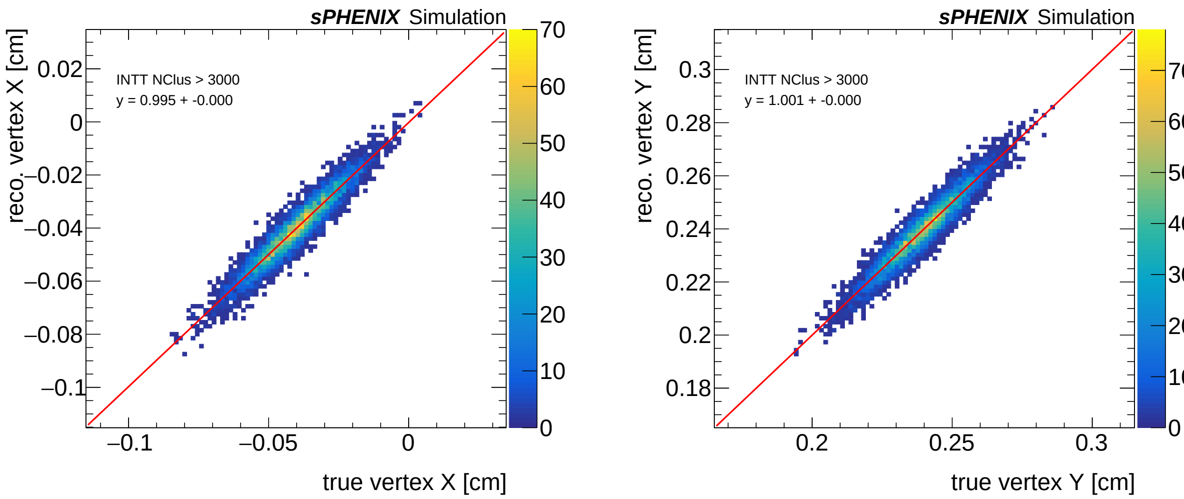

Figure 93: Correlation between the true vertex and reconstructed vertex for X (left) and Y (right) axes. The events with number of clusters $>$ 3000 are shown.

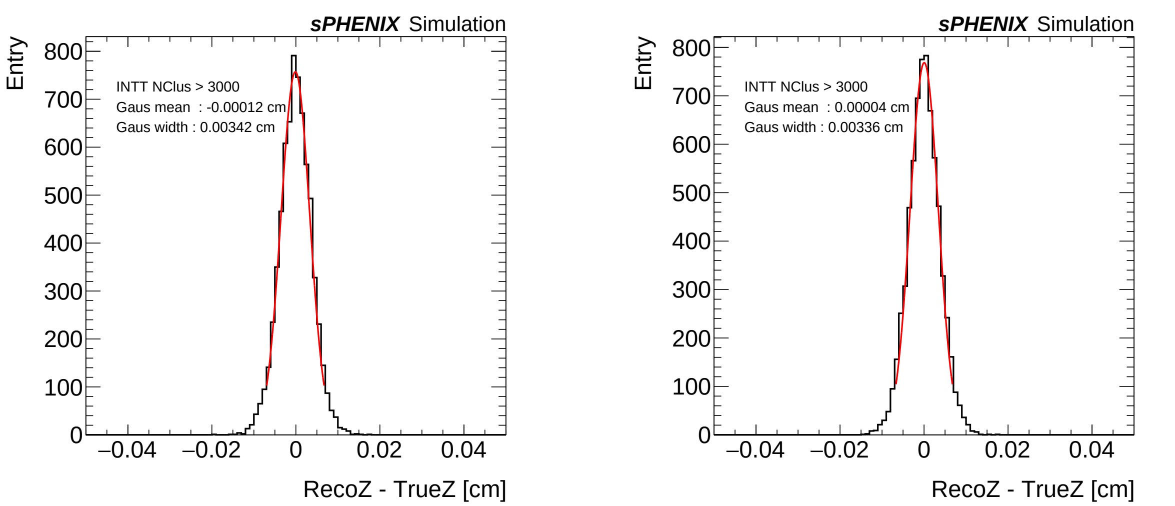

Figure 94: Difference between the true vertex and reconstructed vertex for X (left) and Y (right) axes. The events with number of clusters $>$ 3000 are shown.

To obtain the beam spot size in data, the average vertices are obtained as the first step, which are (-0.191 mm, 2.621 mm) and (-0.277 mm, 2.576 mm), respectively. The discrepancy of the vertices between the two approaches can be explained by the detector misalignment, as described in Chapter 7.1.1. The average of the two vertices, (-0.234 mm, 2.599 mm), is used in the per-event vertex XY position reconstruction. The beam spot sizes for both axes are shown in Figure 95. The beam spot size is $\sim$ 1 mm for both axes. In addition, the beam position stability is studied, as shown in Figure 96. The observed consistency in the vertex position over the run suggests a stable behavior. Consequently, the average vertex position in the XY plane demonstrates the adequacy for being utilized in the tracklet reconstruction.

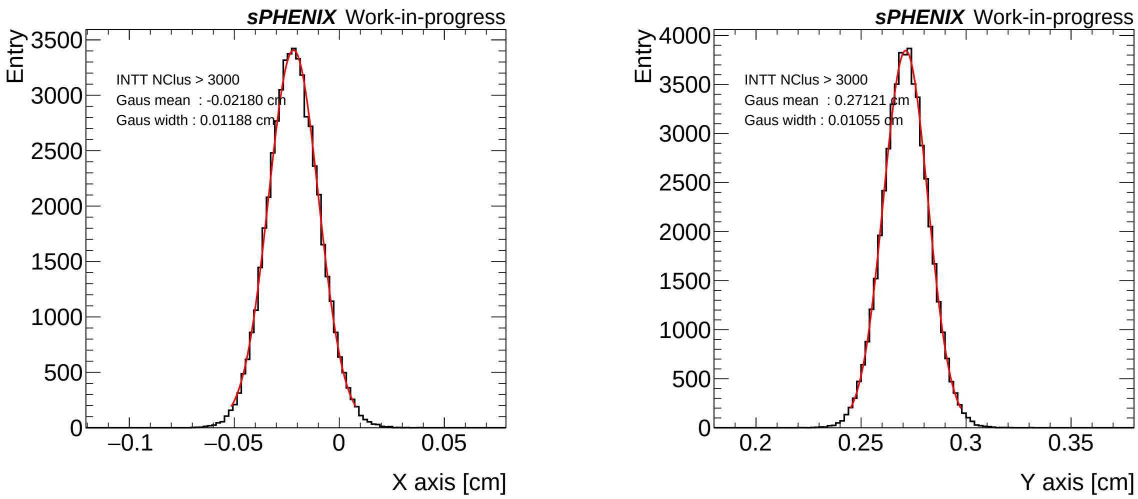

Figure 95: Distributions of the beam spot size in X (left) and Y (right) axes with run 20869.

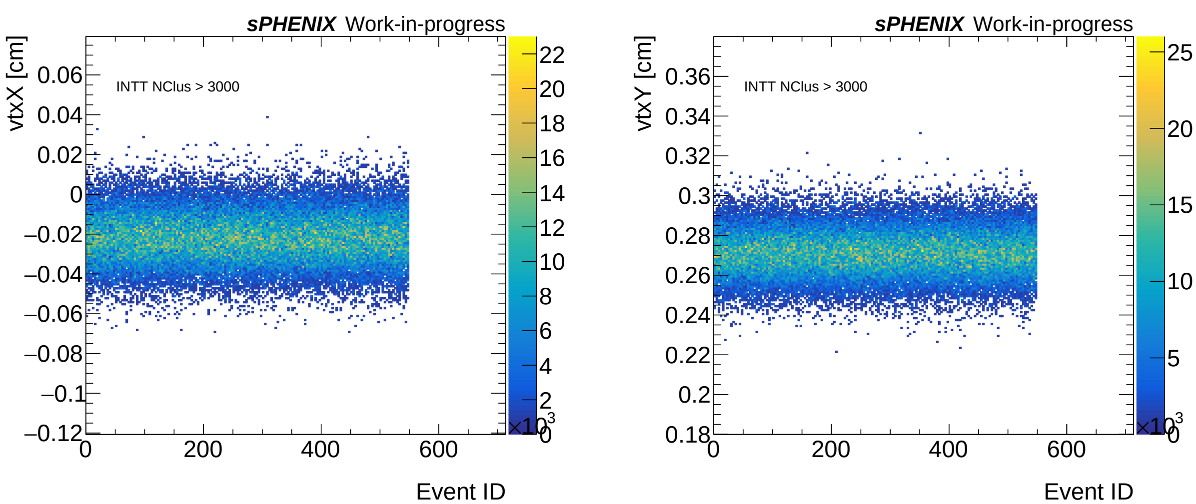

Figure 96: Vertex Position as a function of event index for X (left) and Y (right) axes with run 20869.

F Supplementary plots for vertex reconstruction in the CMS approach

The mean and sigma values of the Gaussian fit to the difference in Z position between the truth vertex and the reconstructed vertex, $\Delta(\mathrm{vtx}_z^{\mathrm{Reco}}, \mathrm{vtx}_z^{\mathrm{Truth}})$, are shown as functions of $\Delta\phi_{\mathrm{cut}}$ and $\mathrm{DCA}_{\mathrm{cut}}$ in Figure 97. The resolution is quantified using the effective width, defined as the minimal range containing 68.5% of the distribution. The distribution of $\Delta(\mathrm{vtx}_z^{\mathrm{Reco}}, \mathrm{vtx}_z^{\mathrm{Truth}})$ and its dependence on the number of clusters in the inner layer, with the optimized parameters $\Delta\phi_{\mathrm{cut}} = 0.3$ degrees and $\mathrm{DCA}_{\mathrm{cut}} = 0.15$ cm, are shown in Figure 98.

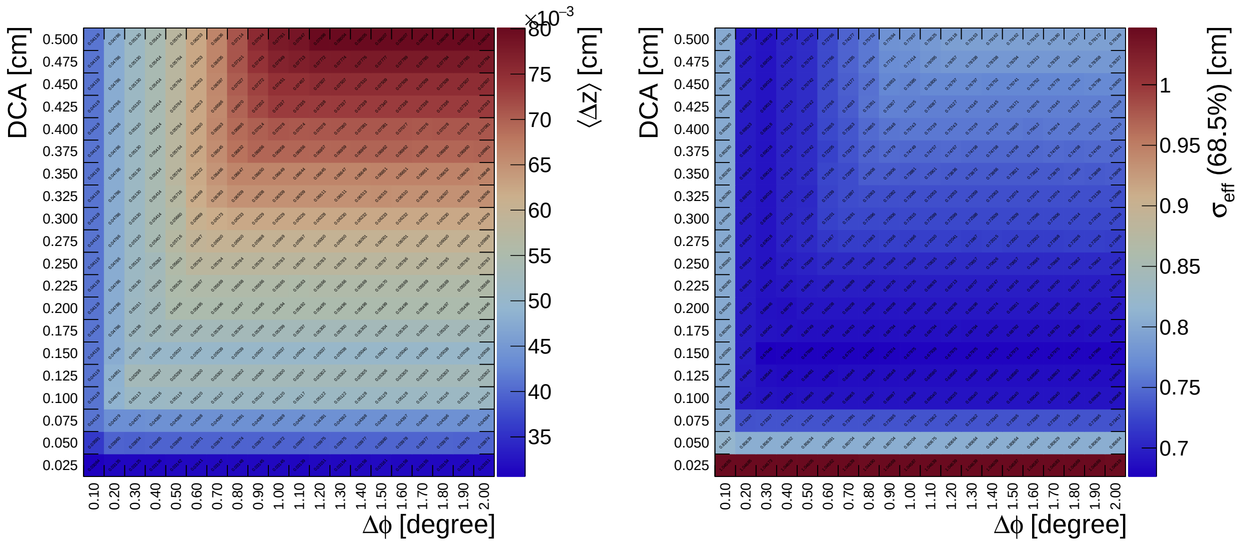

Figure 97: The mean (left) and sigma (right) of the Gaussian fit to $\Delta(\mathrm{vtx}_z^{\mathrm{Reco}}, \mathrm{vtx}_z^{\mathrm{Truth}})$ as a function of $\Delta\phi_{\mathrm{cut}}$ and $\mathrm{DCA}_{\mathrm{cut}}$.

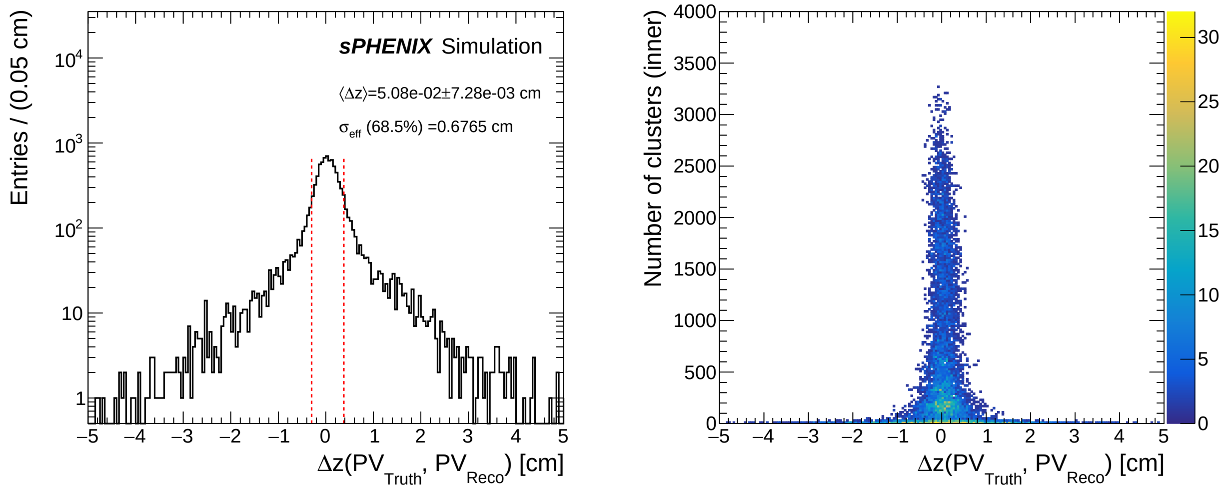

Figure 98: The distribution of $\Delta(\mathrm{vtx}_z^{\mathrm{Reco}}, \mathrm{vtx}_z^{\mathrm{Truth}})$ (left) and $\Delta(\mathrm{vtx}_z^{\mathrm{Reco}}, \mathrm{vtx}_z^{\mathrm{Truth}})$ v.s number of clusters in the inner layer (right) with the optimized $\Delta\phi_{\mathrm{cut}} = 0.3$ degree and $\mathrm{DCA}_{\mathrm{cut}} = 0.15\,\mathrm{cm}$.

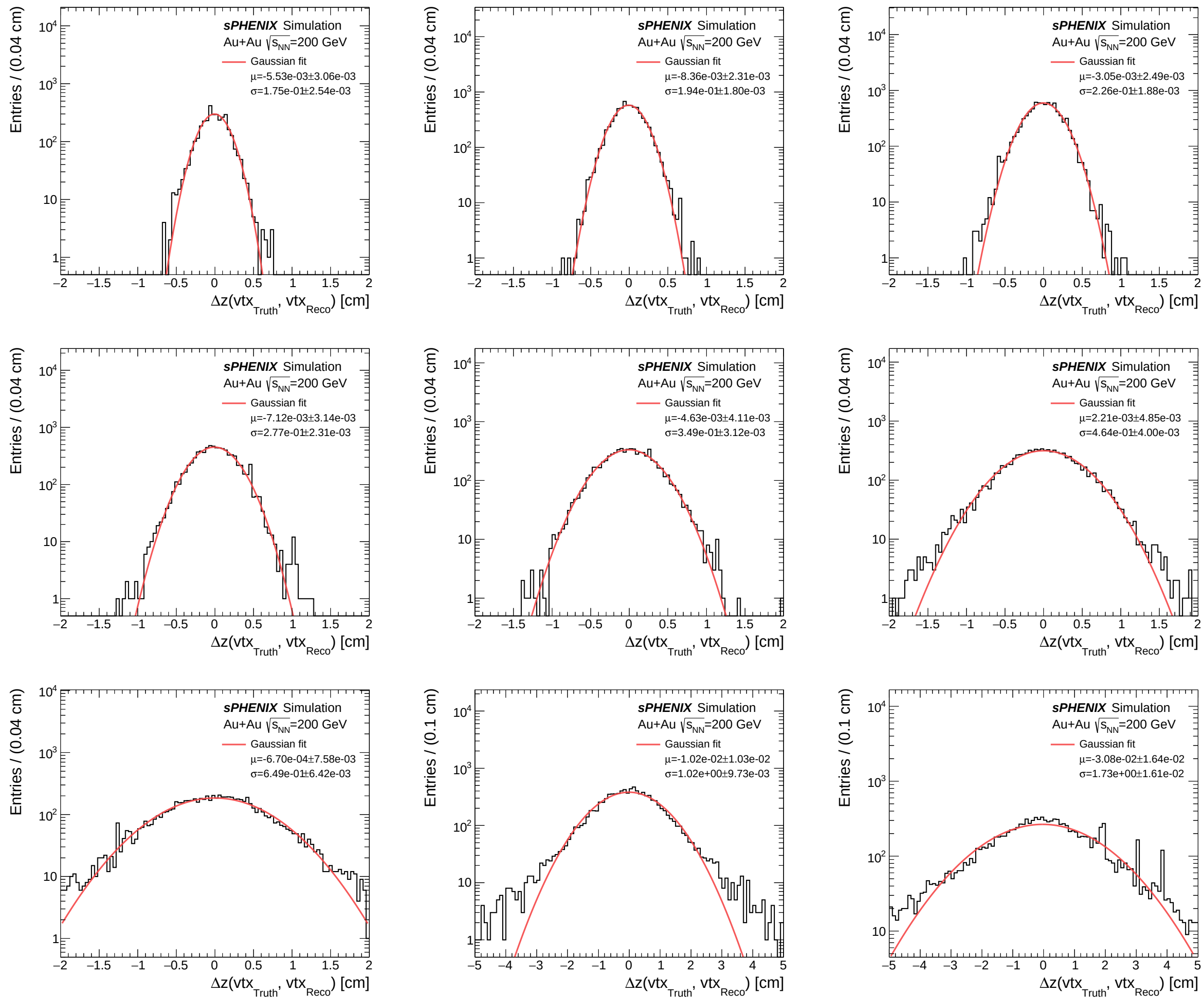

Figure 99: $\Delta(v_z^{\mathrm{Reco}}, v_z^{\mathrm{Truth}})$ and the Gaussian fit. Top row: From the left to the right are the centrality class 0-10%, 10-20%, and 20-30%. Second row from the top: From the left to the right are the centrality class 30-40%, 40-50%, and 50-60%. Third row from the top: From the left to the right are the centrality class 60-70%, 70-80%, and 80-90%.

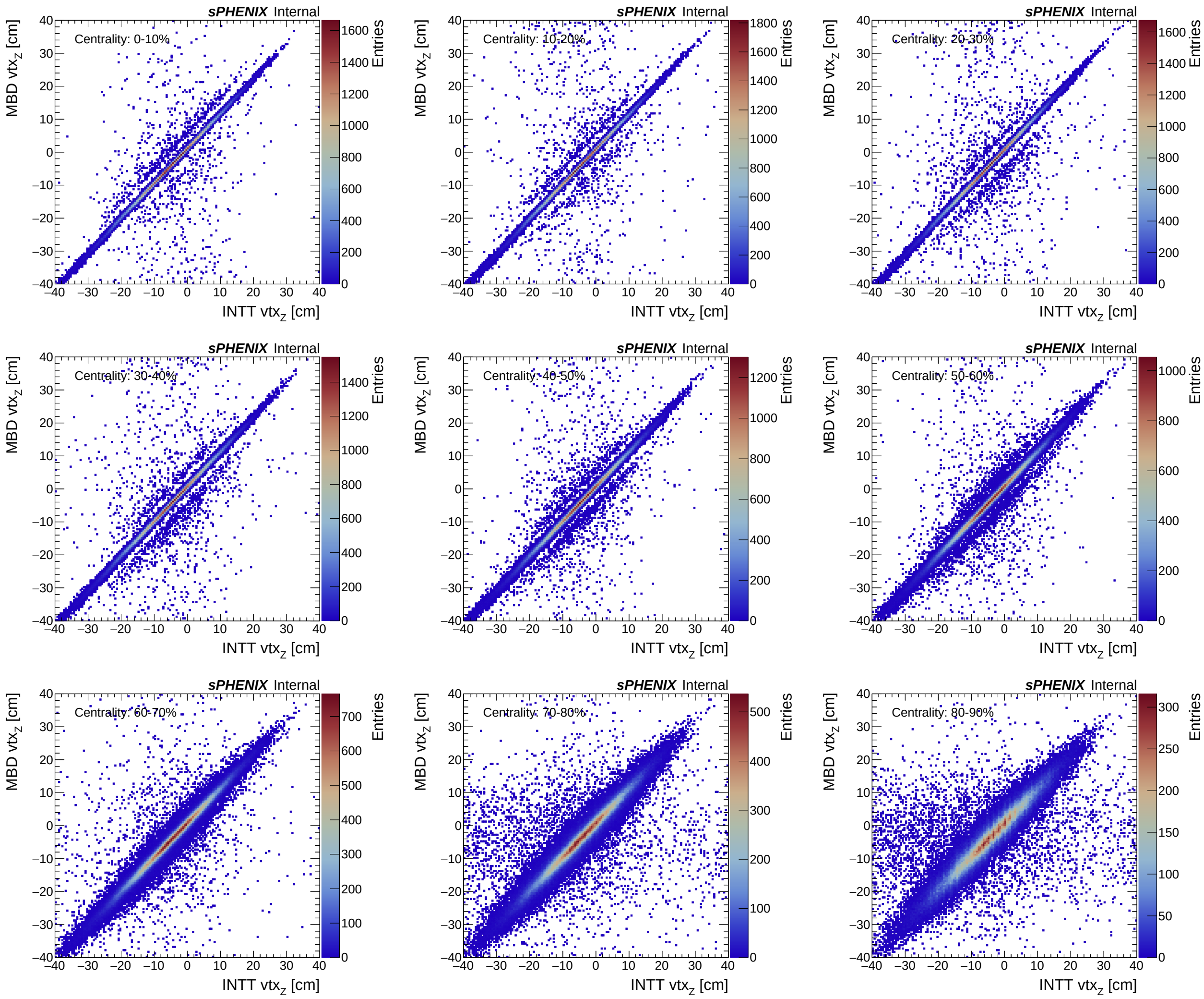

Figure 100: Comparisons between the INTT tracklet vertex Z reconstruction and the MBD vertex determination in different centrality intervals. Top row: From the left to the right are the centrality 0-10%, 10-20%, and 20-30%. Second row from the top: From the left to the right are the centrality class 30-40%, 40-50%, and 50-60%. Third row from the top: From the left to the right are the centrality class 60-70%, 70-80%, and 80-90%.

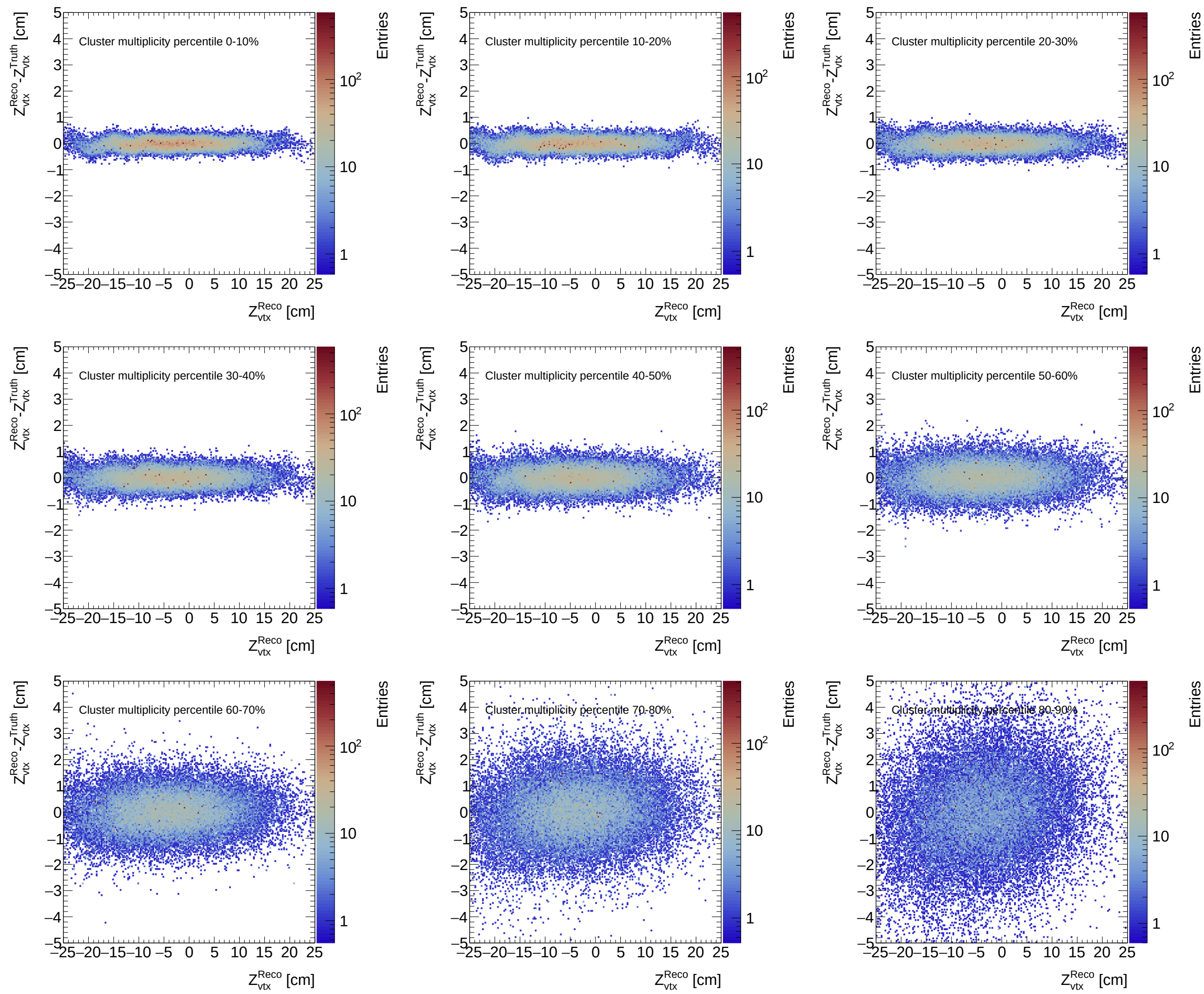

Figure 101: Comparisons of the reconstructed and truth vertex Z position in simulation in different centrality intervals. Top row: From the left to the right are the centrality 0-10%, 10-20%, and 20-30%. Second row from the top: From the left to the right are the centrality class 30-40%, 40-50%, and 50-60%. Third row from the top: From the left to the right are the centrality class 60-70%, 70-80%, and 80-90%.

G Supplementary plots for the correction factors

Corrections factors in specific centrality intervals are shown in this section.

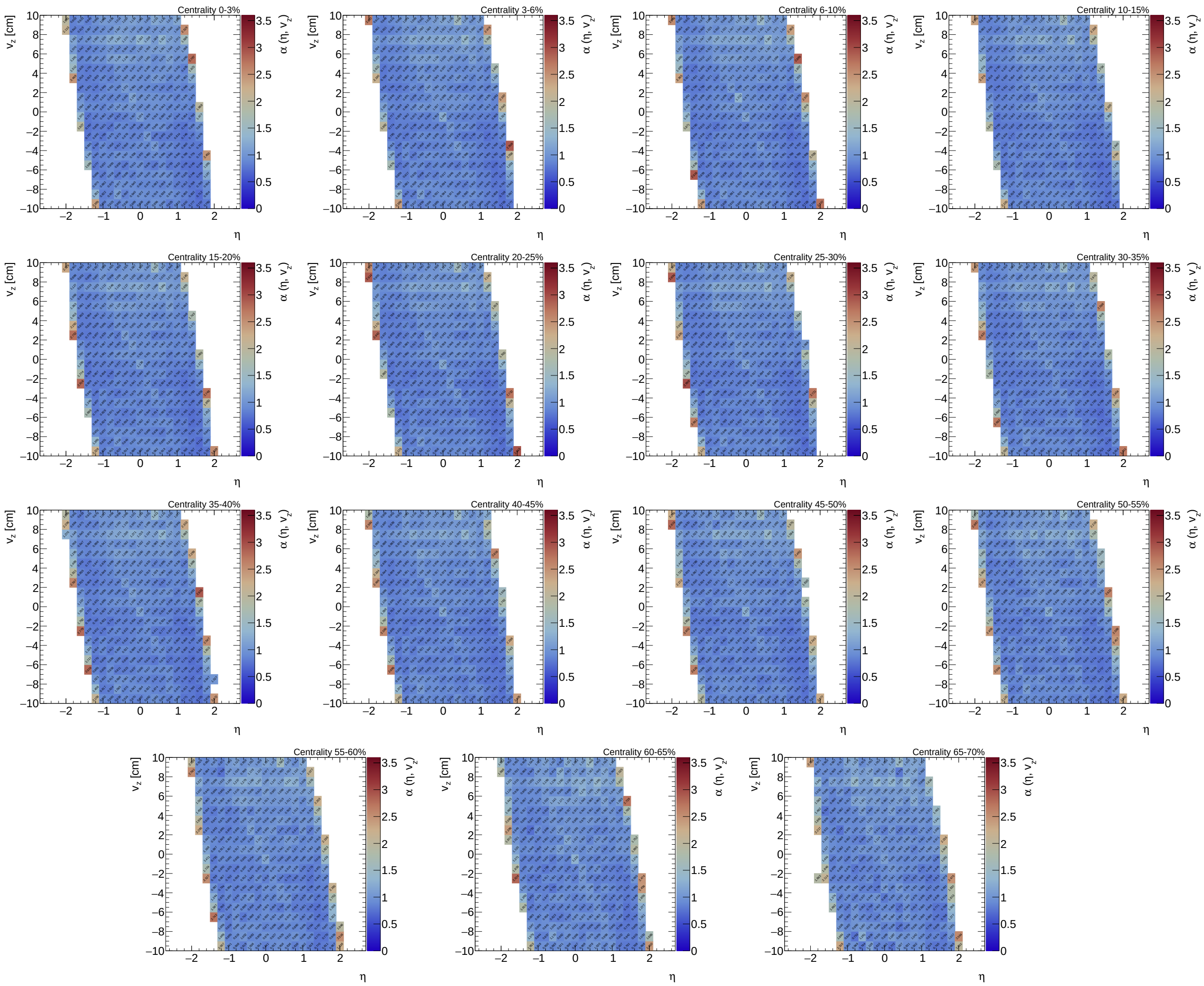

Figure 102: The α factor for each centrality interval.

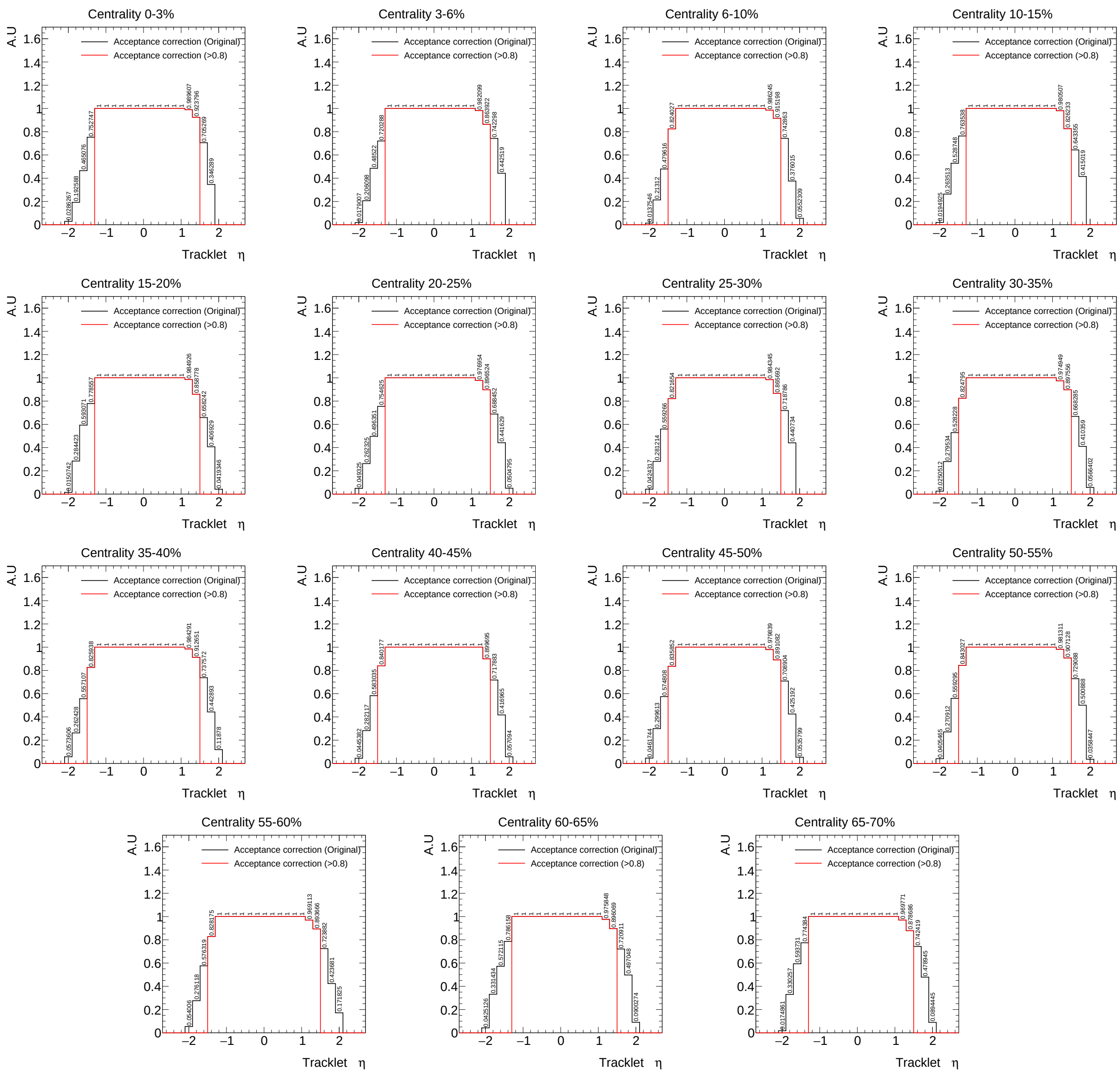

Figure 103: The acceptance correction for each centrality interval.

H Strangeness fraction in simulation

The Fun4All simulation framework, particularly the HepMCNodeReader module, is modified and expanded to allow the enhancement of strange particle fractions. Key modifications include methods for defining enhancement fractions, lists of particle IDs and production probabilities based on the existing measured quantity, and assigning unique identifiers to newly added particles. Static functions for the fitted distributions allow the sampling of kinematic variables, while the fraction of additional strange particles could be dynamically specified through Fun4All macro G4_Input.C. The full implementation can be found at `https://github.com/sPHENIX-Collaboration/coresoftware/blob/master/simulation/g4simulation/g4main/HepMCNodeReader.cc` and the corresponding pull request `https://github.com/sPHENIX-Collaboration/coresoftware/pull/3349`.

The functions used to sample the particle kinematics, p_T and η, are derived by fitting the generator truth distributions of K_s^0 meson from the Pythia8 simulation. The p_T distribution is modeled using an Exponentially-Modified Gaussian (EMG) function, defined as:

$$f(x;\mu,\sigma,\lambda) = \frac{\lambda}{2} e^{\frac{\lambda}{2}(2\mu+\lambda\sigma^2-2x)} \operatorname{erfc}\left(\frac{\mu+\lambda\sigma^2-x}{\sqrt{2}\sigma}\right),$$

where μ and σ are the mean and standard deviation of the Gaussian component, λ is the rate parameter of the exponential component, and $\operatorname{erfc}(z)$ is the complementary error function. The η distribution is modeled as the sum of two Gaussian functions, with equal fractions, sharing the same standard deviation, but with distinct mean values. The generator truth distributions for p_T and η, along with their respective fits, are shown in Figure 104.

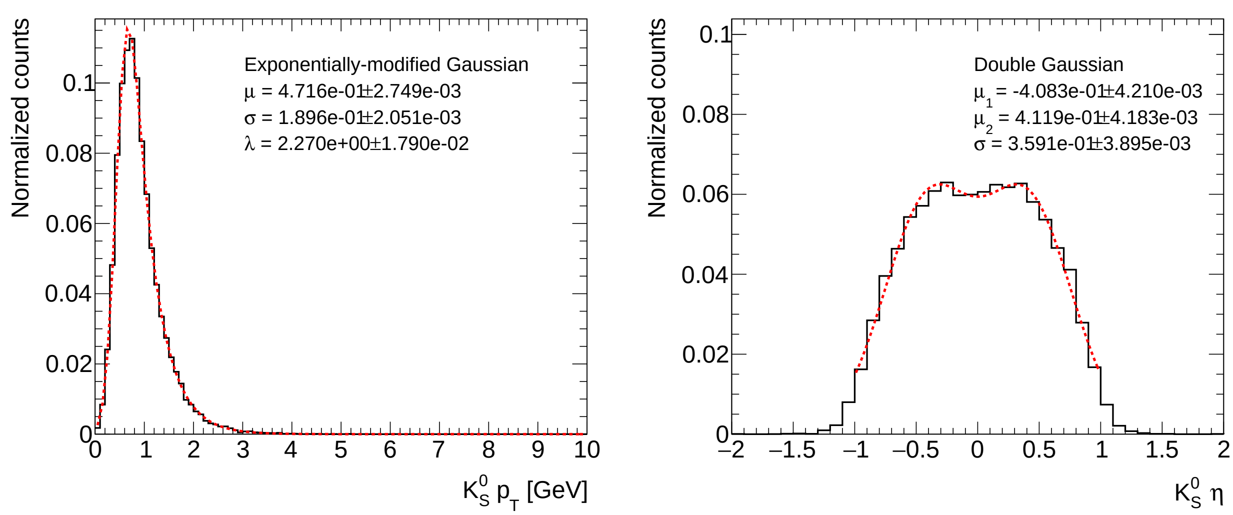

Figure 104: The generator truth distributions of p_T and η and their corresponding fit

A standalone test was performed to sample p_T and η using the EMG and double Gaussian functions, with parameters set according to the fit results, and ϕ uniformly sampled from $-\pi$ to π. A comparison between the truth and sampled distributions of the total momentum p and its z-component p_z is shown in Figure 105, while the two-dimensional distributions of

p_{T} and η from the truth and sampled data are presented in Figure 106. A good agreement between the truth and sampled kinematics ensures that the additional particles introduced in the simulation are consistent with the underlying kinematic properties.

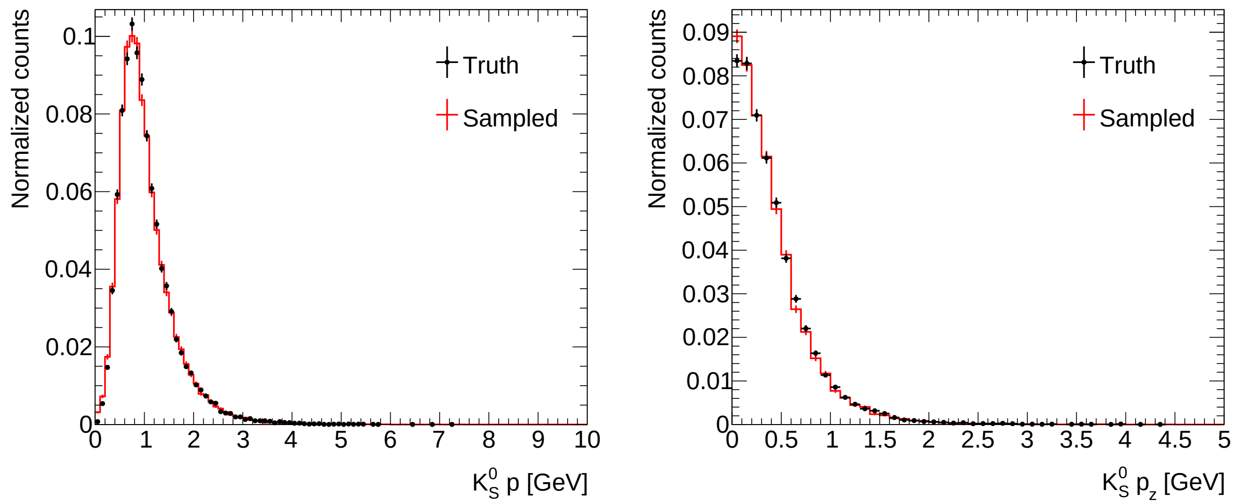

Figure 105: The truth and sampled distributions of the total momentum p (left) and its z-component p_z (right).

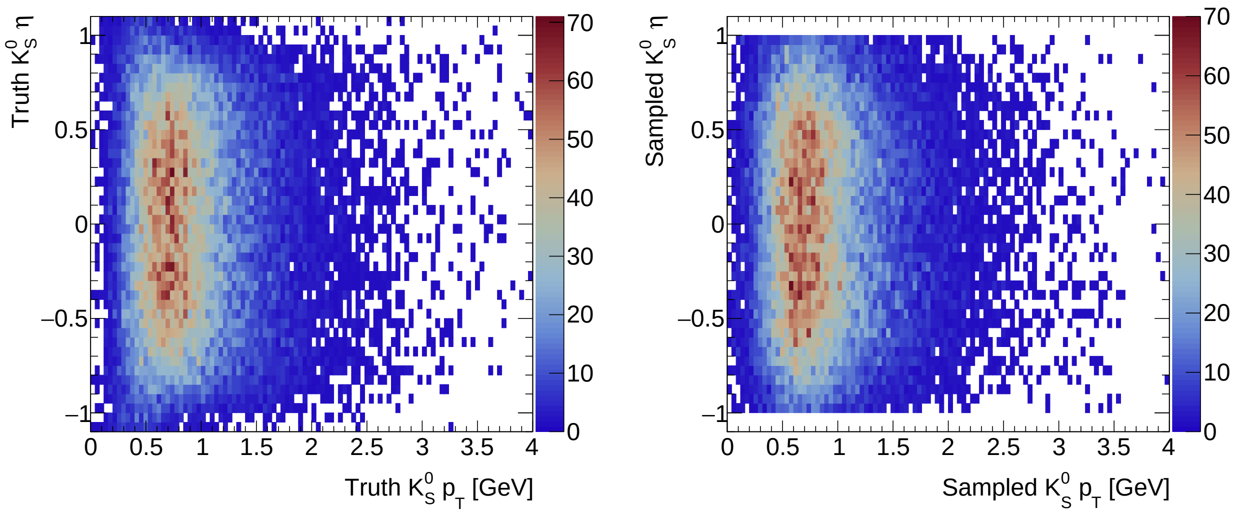

Figure 106: The two-dimensional distributions of p_{T} and η from the truth (left) and sampled (right) particles.

Validation of the implementation was performed using two sets of HIJING minimum bias simulations with enhancement fractions of 40% and 100%, respectively, each containing 500 events. For both validation samples, the additional particles were restricted to K_s^0 mesons and Λ baryons. The top plot in Figure 107 shows the number of K_s^0 mesons and Λ baryons at the HepMC-particle and PHG4Particle stages, confirming that the additional particles were correctly added to the PHG4Particle collection without altering the HepMC record. Marginal differences in the p_T and η distributions of PHG4Particle, shown in the bottom plots of Figure 107, indicate that the introduction of additional particles did not significantly distort the overall event kinematics.

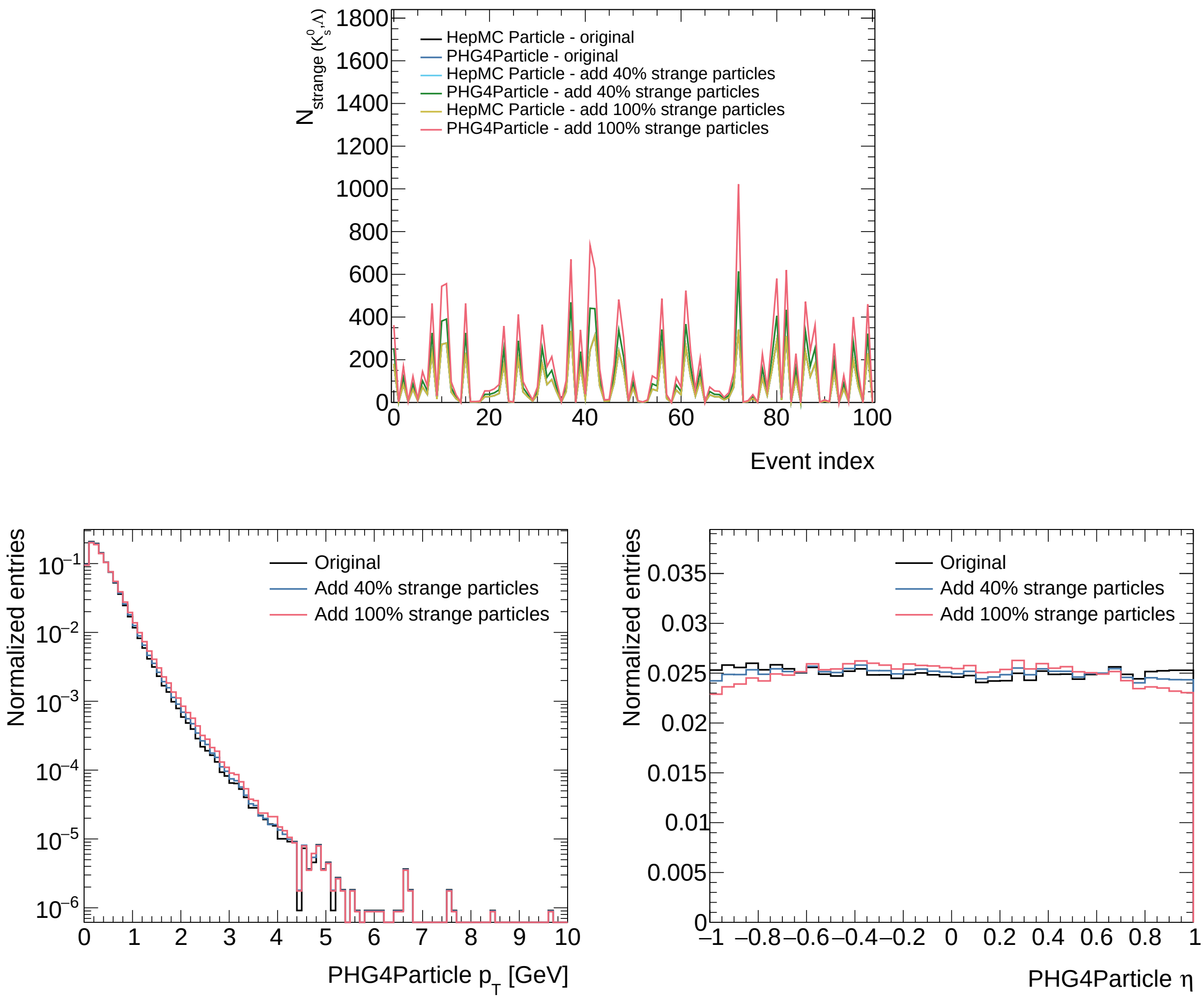

Figure 107: The number of K_s^0 mesons and Λ baryons at the HepMC-particle and PHG4Particle stages (top), the p_T (bottom left) and η (bottom right) distributions of PHG4Particles with additional strange particles.

I Supplementary plots for the systematic uncertainty

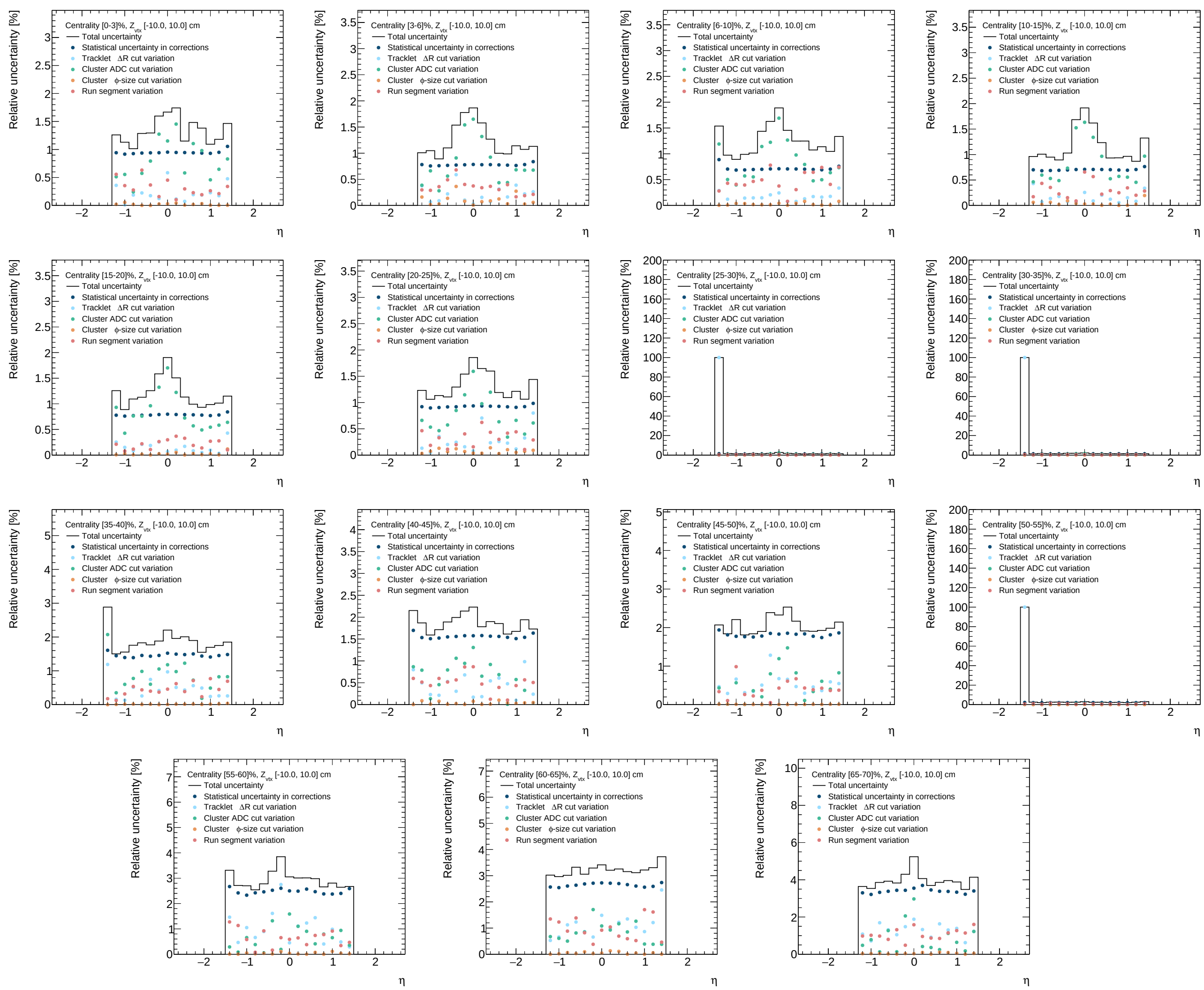

Figure 108: Systematic uncertainties in different centrality intervals.